Self-assembly of liquid crystalline and colloidal nanostructures

by

Ghadah Hadi Saud Sheetah

M.S. Materials Science and Engineering, Colorado University at Boulder,

USA, 2018

M.S. Physics, King Faisal University, KSA, 2011

A thesis submitted to the

Faculty of the Graduate School of the

University of Colorado in partial fulfillment

of the requirements for the degree of

Doctor of Philosophy

College of Engineering and Applied Science, Materials Science and Engineering program

2018

This thesis entitled:
Self-assembly of liquid crystalline and colloidal nanostructures
written by Ghadah Hadi Saud Sheetah
has been approved for the College of Engineering and Applied Science, Materials Science and Engineering program

Prof. Ivan I. Smalyukh

Prof. Patricia Rankin

Prof. David M. Walba

Date

The final copy of this thesis has been examined by the signatories, and we find that both the content and the form meet acceptable presentation standards of scholarly work in the above mentioned discipline.

Sheetah, Ghadah Hadi Saud (Ph.D., Materials Science and Engineering)

Self-assembly of liquid crystalline and colloidal nanostructures

Thesis directed by Prof. Ivan I. Smalyukh

Nanostructure liquid crystal composites are perfect for designing novel materials with predefined properties that can be of substantial interest in many fields including materials science, electronics, optics, and energy storage. Liquid Crystals (LCs) are a good candidate to work as a host medium for nanoparticles with different properties given their low cost and facile responsive characteristic to external stimuli such as voltages as low as one volt. Concentrated dispersions of anisotropic gold, silver, and metal alloy nanoparticles in nematic hosts have been achieved and successfully controlled using low-voltage fields. However, to enable versatile designs of material behavior of these composites, simultaneous dispersion of anisotropic particles with different shapes, alignment properties, and compositions is often needed. For example, integrated plasmonic gold nanoparticles in the up-convergent nanoparticles (UCNPs) or quantum dots (QDs) semiconductor matrices serves as nano antennae that can harvest the light energy to the nanostructured matrix giving rise to potential applications. In this work, spectral characteristics of dispersions of multiple types of anisotropic nanoparticles in a common nematic host LC provide an unprecedented variety of electrically- and optically-tunable material behavior. Different composites of inclusions of plasmonic gold nanorods, quantum dots, dyes will be explored and implementing such composites in an inexpensive, energy-efficient, large-area, fast-switching smart windows applications, along with exploring different self-assembled systems by entropically driven forces will be discussed. Overall, utilizing LCs as a guest medium to these nanoparticles allows for unique features as well as promising properties through the design of novel self-assembly based hybrid nanostructures. This can give rise to potential and practical applications for the fabrication of optical or electro-optical devices such as climate dependent optimal solar gain smart windows, switchable plasmonic polarizers, and may expand to further satisfy renewable energy needs.

Dedication

To my father

Acknowledgements

I begin with my gratitude to Allah for giving me the strength, and for putting wonderful people in my journey, I am grateful to everyone who showed support and encouragement. Thanks to my advisor, Professor Smalyukh, for his guidance, assistance, and suggestions in my quest for knowledge. His dedication to research is second to none, and I aspire towards it. Thanks to my parents for their unconditional love and support throughout my life. Thanks to all of my siblings, Ghaithah, Mohammed, Bushra, Ali, Saleh, Bashair, Yahya, and Faisal. Thank you all for being there for me. I would like to express my gratitude to my Grandmother whom I lost this past year. Many thanks to the wonderful people I met in Boulder and my friends for their heartfelt support. Many thanks to Ginny, Joyce, Susanne, Arine, Hillary, Bethanie, Li, Khowlah, Dua'a, Aysha, Baraah, Nikkie, Hope, Joris, Briana, Shannon, Sarah, Jessie, Kasey, Melanie, Raina, Audra, Amy, Nik, Nicole, Claudia, Tessa, Destiny and all who helped ease my rough days and put a smile on my face. A big thank you to the soft matter group members. Special thanks to Dr. Liu for the knowledge and lab experience he passed on to me. Thanks to my lab-mates and colleges Ye, Benny, Sungoh, Hayley, Rachel, Yuanyuan, and all. I wish you all the best with your future endeavors. Many thanks to a handful of professors whom work ethics are admirable and made me appreciate the academic environment. Special thanks to Professor Rankin, Professor Bryant, Professor Reznik, and Professor Yin. I must give thanks to my committee members for being patient with me when I reschedule my exams and my thesis defense. I genuinely thank everyone from the physics department, and I look forward to building bridges and keeping in touch.

Contents

Chapter

Tables

Figures

Chapter 1

Introduction

1.1 Liquid Crystals

Liquid crystals (LCs), or flowing crystals, [4] define a new state of matter with properties in between those of ordered solid state and the disordered state of flow-like liquids. This intermediate state, also known as the fourth state of matter, acquires its properties from its constituents and their order. For molecular LCs, molecules have an anisotropic shape that is either rod-like or disk-like with dimensions in the nanometer range. Weak intermolecular enthalpic forces between the molecules, such as hydrogen bonds or Van der Waals forces, give rise to an ordered LC phase, namely an orientational order. While, enthalpic forces primarily drive this LC phase, an ordered LC phase may also arise due to entropic driven forces, such as depletion attraction forces or excluded volume based forces, which contribute to the self-assembly of the anisotropic LC molecules and give rise to the orientational order of the LC phase.

Despite the fact that in this LC phase, the anisotropic molecules are randomly positioned, nonetheless, the molecules align with their long axis along a certain orientation. This orientation is denoted by a director $\mathbf{N}$, which presents the average orientation of local LC molecules, where $\mathbf{N}$ is noted as a two-headed arrow along the orientation or alignment directionality, since the physical properties of the molecules are the same in $+\mathbf{N}$ or $-\mathbf{N}$. Fig 1.1(b) demonstrates a LC phase, also noted as nematic phase, in comparison with the crystalline solid phase and isotropic liquid phase, respectively, Fig. 1.1(a),(c).

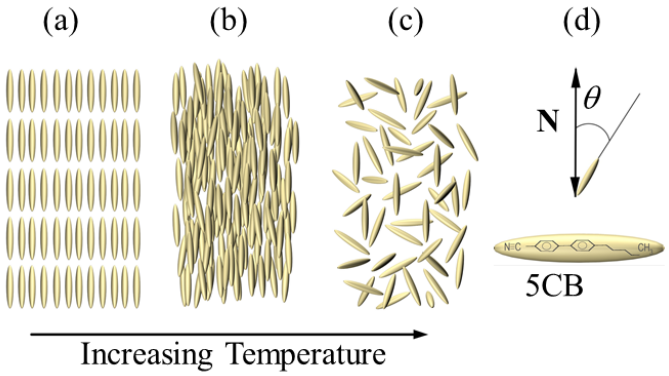

Fig. 1.1: A schematic diagram of LC phase in thermotropic LCs that are commonly known to be temperature sensitive. With increasing temperature, the crystalline solid phase changes to the LC phase, or nematic phase, then to isotropic liquid phase: (a) ordered solid phase, (b) nematic LC, and (c) isotropic liquid phase. (d) Orientation distribution can be deduced by the molecules long axis deviation from the local average orientation of LC molecules denoted by the director **N**. The deviation of the LC molecules from **N** by an angle θ (top), and a molecular structure of a common thermotropic LC known as pentyl cyanobiphenyl, or 5CB (bottom).

The orientation of the LC molecules are analyzed with a traceless tensor order parameter that is used to describe the orientational order of the nematic LC. However, with certain LCs, such as uniaxial LCs, it is sufficient to express this orientational order more simply with a scalar order parameter S:

$$S = (3\left\langle \cos^2\theta \right\rangle - 1)/2, \tag{1.1}$$

where θ is the deviation of the long molecular axis from the LC local director **N** as shown in Fig. 1.1(d), which is the preferred orientation in a given LC volume. S can range from 1 to $-1/2$, where 1 indicates complete crystalline order, 0 is an isotropic state, and $-1/2$ reflects the molecular orientations where the molecules long axes are in the plane perpendicular to the local director. At the extreme ends of S values, $S = 1$ or 0, the LC loses its liquid crystalline phase, and the constituents form either a crystal phase or a liquid phase, respectively. For the nematic LC phase, on the other hand, S ranges between 0.3 and 0.9. Note that S can measure not only the order of the LCs themselves, but also the orientational order of any inclusions of anisotropic nanoparticles in the LC medium, at which case S will reflect how well these particles are aligned with respect to **N**, as demonstrated in chapter two.

LCs are ubiquitous in nature and have many different types that can be classified into categories that depend on certain parameters, such as thermotropic LCs that depend on temperature, polymeric LCs that depend on their constituents, lyotropic LCs that depend on the concentration, and so on. All of these categories exhibit physical properties, such as birefringence, dielectric anisotropy, and optical and electronic properties that can be exploited for many different applications. Since thermotropic LCs are utilized in many applications, such as LC displays, switchable smart windows, or very sophisticated optoelectronic devices, they will be the focus of this work, and part of this chapter is devoted to exploring their characteristics. This is followed by theoretical models that explain LCs in general and their associated properties.

While the anisotropy of molecular constituents plays a major role in the formation of the LC phase, thermotropic LCs mainly form through weak intermolecular interactions that are influenced by temperature. Consequently, thermotropic LCs can be controlled by temperature to reach the liquid crystalline phase. However, higher temperatures lead to increasing the Brownian motion, resulting in a decrease in the orientational order of the LC phase until it falls off into the isotropic phase, as shown in Fig. 1.1(b-c). The temperature range of the LC phase is $T_m < T < T_c$, where T_m is the melting point after which a transition occurs from the solid state to the LC phase. T_c, on the other hand, is the clearing temperature at which the LC phase turns into an isotropic liquid and loses its long-range ordering and its properties. Different temperature ranges will appear depending on the thermotropic LC itself. In general, a thermotropic LC can be a *monotropic* if the LC state is thermodynamically stable. This means the LC phase can be achieved by either cooling or heating below the clearing point or above the melting point of the corresponding thermotropic LC, respectively. On the other hand, if the LC phase is metastable, which is referred to as an *enantiotropic* state, then the LC phase occurs only via one end of the transitions, cooling the isotropic phase to the liquid phase at the clearing temperature, for example. Typically thermotropic LC molecules consist of a rigid head group, which is commonly composed of several benzene derivatives and a hydrocarbon chain.

Thermotropic LCs exhibit different mesophases. For example, they can be nematic, semectic A, semectic B, cholesteric, etc. The cholesteric LC phase is basically a nematic phase of molecules that are intrinsically chiral, or a nematic LC that is doped with either left- or right-handed chiral dopants. This chirality leads to a twist across the bulk of the LC, where a full twist across the bulk of the LC by 360° defines a single cholesteric pitch **p**, see Fig. 1.2(b). Cholesteric LCs are extensively used in displays, where they can be actively tuned or pre-designed to have a specific pitch value, typically in the micrometer range. However, once the pitch approximates the light wavelength, the light polarization state can be modulated leading to different potential optical applications, as demonstrated in chapter three.

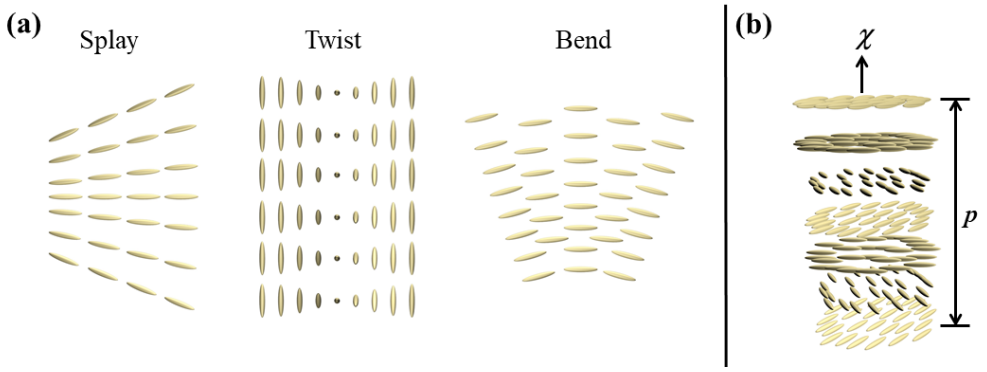

Fig. 1.2: (a) The classic elastic distortions: splay, twist, and bend in LC, respectively. (b) An illustration of a full twist of LC layers of 360° forming a pitch (p) along the chiral axis.

1.2 Dielectric Anisotropy, Birefringence, and Polarized Light

One of the main properties of a LC is its dielectric anisotropy. Generally, LC molecules contain a small charge distribution that gives rise to small dipoles. Consequently, the dipoles give rise to induced dipole-dipole interactions in the bulk of the LC. However, the dipoles can easily be polarized with an external electric field. This polarizability differs along the long axes of the molecule compared to their short axes. This polarizability also depends on the constituents of the LC, and as a result of this difference in polarizability, LCs exhibit dielectric anisotropy $\Delta\varepsilon$, where $\Delta\varepsilon = \varepsilon_{\parallel} - \varepsilon_{\perp}$. $\varepsilon_{\parallel}$ and $\varepsilon_{\perp}$ are the dielectric constants measured parallel and perpendicular to the

electric filed **E** applied on the LC medium, respectively. To minimize the electrostatic energy in the presence of the electric field, the molecules will have to reorient to be either along the electric field direction ($\Delta\varepsilon > 0$) or perpendicular to it ($\Delta\varepsilon < 0$). This is an important feature in designing LC panels with certain reactions to external stimuli and is extensively utilized already in LC displays (LCD).

Another interesting property of LCs is their optical birefringence. Here, the light experiences double refraction as it propagates through the LC medium where the light interacts with two different refractive indices of the LC, n_o and n_e. This birefringence given by Δn, where $\Delta n = n_e - n_o$, is established through the different refractive indices, where n_e is an extra-ordinary refractive index, while n_o is the ordinary refractive index. Consequently, the optically anisotropic medium decomposes any polarization state of the incoming light into two different orthogonally polarized components of ordinary and extraordinary rays, which travel at different speeds resulting in a phase difference or retardation.

This retardation can be measured using a Polarized Optical Microscopy (POM) demonstrated in Fig. 1.3(a). The the indecent light is polarized before it passes through a LC slab or cell, where the LC is homogeneously aligned along a certain orientation, $\mathbf{N_0}$, here denoting the far field director. When the polarized light is not parallel to $\mathbf{N_0}$, the light becomes elliptically polarized after it passes through the LC slab. This results in transmitting selective components that are filtered out through the analyzer, as illustrated in Fig. 1.3(b). Because the light experiences constructive and destructive interferences, the light experiences a phase shift, which mainly depends on the birefringence ($|\Delta n|$) and the thickness (t) of the LC slab. This is extensively described by the Michel-Levy table that associates the wavelength of the light and transmitted colors with given values of $|\delta n|$ and t. This is useful for tuning the polarization state of the light passing through the LC medium. [25] The retardation can be quantitatively measured by the following relation:

$$\delta = (2\pi/\lambda) \times \Delta n \times t \tag{1.2}$$

δ is the quantitative retardation of the light passing through the birefringent medium. From this

equation, the greater the birefringence or the thickness, the more retardation light experiences. If light propagates through 5CB (4-Cyano-4'-pentylbiphenyl), which is a common thermotropic LC, for example, then the light encounters the short axis (fast axis), or the long axis (slow axis or optic axis), or in between the two axes when the light propagates at a non-zero angle θ with respect to the optical axis. Fig1.3(b) illustrates how light propagates in a LC medium between cross-polarizers. In this case, an effective refractive index is considered

$$n_{\text{eff}}^2 = \frac{n_e^2 n_o^2}{n_e^2 \cos^2\theta + n_o^2 \sin^2\theta} \tag{1.3}$$

and the effective birefringence becomes $\Delta n_{\text{eff}} = n_{\text{eff}} - n_o$. Given their uniaxial nature, LCs are commonly known for having only one optical axis. These properties make LCs very attractive and useful for many applications and make them the perfect candidate as a guest-host platform to design new composites with unique properties, as will be demonstrated with examples in the preliminary results.

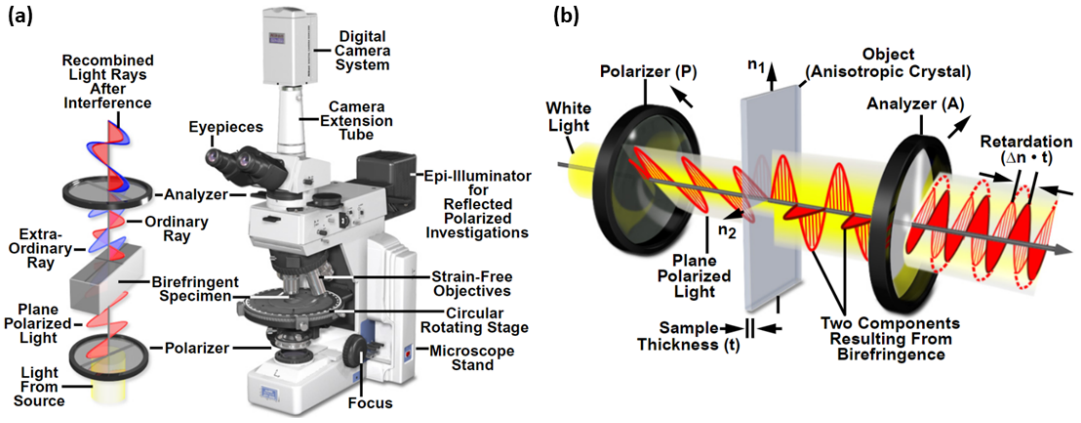

Fig. 1.3: (a) An illustrations of the Polarized Optical Microscopy (POM) with a polarizer **P** oriented orthogonally to the Analyzer **A**; as the LC sample rotates the transmission of the light changes from dark state (**N** parallel to **A** or **P**) to a bright state (**N** at 45 degrees from either **A** or **P**). The given LC sample here is a homogeneous planar LC cell, it can be of different alignment settings, and POM is useful in distinguishing LC orientations. Note that n_1 and n_2 correspond to n_{e} and n_{o}, respectively. (b) Detailed illustrations of the light propagation through the birefringent LC cell under crossed-polarized illumination (both images obtained from https://www.microscopyu.com/techniques/polarized-light).

1.3 Elastic and Surface Anchoring Energy of Liquid Crystals

In the nematic phase, the director field **N** is uniform as long as there are no defects or distortions present. A penalty to introducing any deformation in the LC medium will increase the free energy per unit volume of the uniformly aligned nematic LC, commonly referred to as free energy density. The free energy density of the LC medium, $\mathcal{F}$, can be written as

$$\mathcal{F} = \mathcal{F}_0 + \mathcal{F}_\mathrm{d} + \cdots, \tag{1.4}$$

where $\mathcal{F}_0$ is the free energy associated with the uniform undeformed director **N** of the nematic LC. This free energy density can be considered as the ground state at which the LC free energy density is minimal. $\mathcal{F}_\mathrm{d}$, on the other hand, is the free energy density of the elastically deformed nematic LC. More deformation can be generated at surface boundaries or by applying external fields onto the LC medium, for example. Consequently, an additional energy cost is introduced, and more terms will contribute to the overall total energy density. Traditionally, the energy density of elastically deformed LC can be presented by the Frank-Oseen free elastic energy density: [26]

$$\mathcal{F}_\mathrm{d} = \frac{1}{2}[K_{11}(\nabla \cdot \mathbf{N})^2 + K_{22}(\mathbf{N} \cdot (\nabla \times \mathbf{N}))^2 + K_{33}(\mathbf{N} \times (\nabla \times \mathbf{N}))^2], \tag{1.5}$$

where **N** is the LC director, and K_{11}, K_{22}, and K_{33} are the three main elastic constants, known as Frank elastic constants associated with splay, twist, and bend, respectively. Each of them corresponds to specific distortion in the nematic phase, see Fig. 1.2(a), in addition to mixed elastic constants known as the splay-bend and saddle-splay constants, K_{13} and K_{24}, respectively. Frank's constants have been measured for different nematic LCs with values around **pN**, see table 1.1, for example. [27] With the one constant approximation, these three constants can be presented by one constant K, reducing the Frank-Oseen equation to a shorter equation that characterizes and quantifies the different distortions the LC "feels":

$$\mathcal{F}_\mathrm{d} = \frac{1}{2}K[(\nabla \cdot \mathbf{N})^2 + (\nabla \times \mathbf{N})^2]. \tag{1.6}$$

	K_{11} (pN)	K_{22} (pN)	K_{33} (pN)	n_e	n_o
5CB	7.0	4.6	10.4	1.74	1.54
E7	6.4	3.0	10.0	1.69	1.5
AMLC0010	17.2	7.5	17.9	1.55	1.45

Table 1.1: The main three Frank elastic constants for thermotropic LCs used in this manuscript; 5CB, E7, and AMLC0010 (MLC6609). Also, the ordinary and extraordinary values of refractive indices of each LC.

As mentioned earlier, **N** is generally uniform in the absence of external fields; however, when an external stimuli is applied, the orientation of the LC director is deformed. [11] This happens when applying either an electric or magnetic field. For example, with the application of an electric field across a nematic LC medium, there will be an additional electric free energy density added to the Frank free energy. This electric free energy density is given by

$$\mathcal{F}_{\text{elec}} = -\frac{\Delta\varepsilon}{2}(\mathbf{N}\cdot\mathbf{E})^2, \tag{1.7}$$

where **E** is the electric field. This equation indicates that the director **N** changes its orientation either along or perpendicular to **E** depending on whether the $\Delta\varepsilon$ value of the LC medium is positive or negative, respectively. Different examples are presented in future chapters.

Additionally, **N** reorients close to interfaces between solid walls and LC. Treating the surfaces of the cell walls forces specific orientation of **N** close to these surfaces compared to the bulk LC medium. Likewise, **N** reorients at the surfaces of particles that are doped in the LC medium, and its alignment depends on the surface treatment or functionalization of these particles. This reorientation of **N** depends on the surface area and the strength of the surface anchoring. In general, and in the proximity of any surface, LC molecules follow an easy axis that molecules follow locally. There are different surface anchoring effects that force the director to align accordingly. For example, if the orientation of the easy axis is perpendicular to the solid surface, then the surface anchoring is said to be homeotropic, as illustrated in Fig. 1.4(b). If the easy axis is in plane of the surface, then it is said to be planar anchoring, as shown in Fig. 1.4(c). The anchoring may be either homogeneous or degenerate anchoring. For the degenerate anchoring case, multiple easy axes are

associated with the different regions. Homogeneous homeotropic and planar surface anchoring are studied for different LC cells in this thesis. The anchoring is said to be strong or weak, depending on whether the nematic LC director is rigidly fixed along the easy axes or not. And the anchoring free energy density is given by the Rapini-Popular relation:

$$\mathcal{F} = \frac{1}{2}[W_p \sin^2(\theta - \theta_0) + W_a \sin^2(\varphi - \varphi_0)], \tag{1.8}$$

where θ_0 and φ_0 are the polar and azimuthal angles describing the easy axis orientation, and θ and φ describe the deviation of the nematic LC director from the easy axis, while W is the anchoring strength coefficient measured in (J/m^2). The study of surface anchoring is of great interest in many LC device applications, though it is not fully understood. [28]

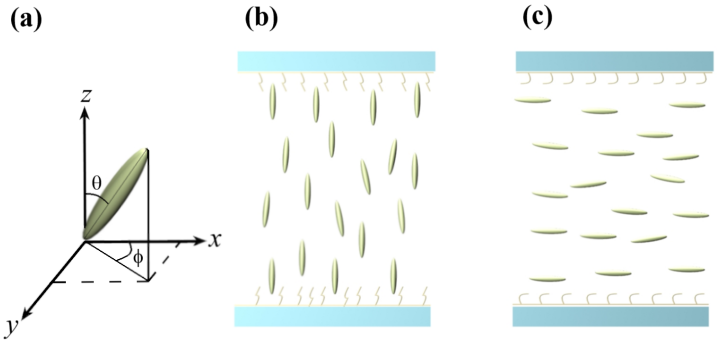

Fig. 1.4: (a) A schematic representation of the anchoring angles; polar angle θ and azimuthal angle ϕ (b) and (c) show the anchoring of nematic LC on the surfaces within a cell after treating these surfaces with appropriate polymers to induce the alignment needed close to the surfaces; (b) Homeotropic anchoring, and (c) planar anchoring. The nematic LC director extends its orientation to the bulk of the cell as a result of the long-range ordering to minimize the elastic energy of the LC system.

1.4 Plasmonic nanoparticles

Nanoparticles usually range in dimensions from $1 - 100$ nm in size. In general, nanoparticles show an intermediate behavior between that of bulk solids and that of atoms or molecules. The study of nano-sized particles became possible with the assistance of different nano-technological tools such as Scanning Electron Microscopy (SEM) and Tunneling Electron Microscopy (TEM). Among the different nanoparticles used, plasmonic nano particles are of interest (and focused

on here) given how their morphology affects their properties, which can be tuned by means of bottom-up wet chemistry methods. This makes plasmonic nanoparticles unique in allowing the ability to engineer their optical, electronic, and other properties for use for in a wide range of applications. Furthermore, incorporating these particles as colloidal dispersions in nematic LCs creates even more room for engineering directed towards specific applications. Since plasmonic nanoparticles are extensively used in this work, the following sections are dedicated to describing the main properties associated with plasmonic nanoparticles, specifically gold nanorods followed by a discussion of techniques to synthesize them and an explanation of how to tune their morphologies.

1.4.1 Surface Plasmon Resonance

Noble metal nanoparticles such as gold nanoparticles have interesting optical properties that arise from a localized surface plasmon resonance (SPR) that depends heavily on having a high electron density within the metallic nanoparticle. [30] When light hits a small metal nanoparticle that is much smaller than the wavelength of light a strong interaction happens between the free electrons on the metals surface and the light. The oscillating electric filed of the incoming electromagnetic wave delocalizes the electrons in the conduction band of the metal nanoparticle. Opposing this motion, the Coulombic forces work on restoring these electrons to their original positions within the nanoparticle, see Fig. 1.5. This leads to an oscillating motion of electrons, which is in resonance with a narrow band of wavelengths of the illuminating light, leading to the SPR. This SPR causes absorption scattering, and it can be measured through absorbance measurement via a spectrometer, for example.

The localized SPR is mainly affected by the nanoparticle composition, as well as the particle size and shape. Additionally, the light interaction with the refractive index of the medium surrounding the metal nanoparticle plays a role in changing the SPR peak position, which can either experience a redshift or a blue shift with higher or smaller refractive indices, respectively. This is particularly important for many sensing applications.

Mie theory provides a description for small spherical particles interacting with light and

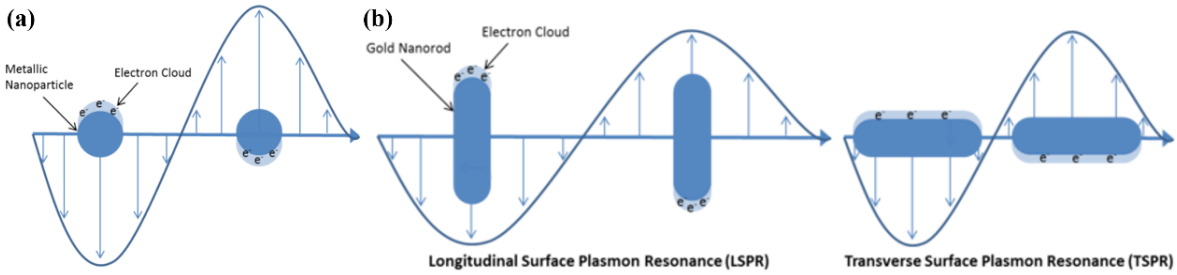

Fig. 1.5: (a) Schematic of SPR in a small metallic spherical nanoparticle irradiated by light. (b) The electron oscillations associated with a rod like metallic nanoparticles exhibiting transverse and longitudinal SPR with light irradiation (image obtained form NANOHYBRID website: https://nanohybrids.net/pages/plasmonics).

provides an exact explanation to the scattering and absorption associated with these particles, [31,32] and consequently determines the optical spectra. If the particles are much smaller than the wavelength of light it simplifies the solutions to Maxwells equations and allows for considering only the dipolar contribution, which gives the scattering (σ_{sca}) and absorption (σ_{abs}) cross sections for the metallic nanosphere:

$$\sigma_{\text{sca}} = \frac{k^4}{6\pi\varepsilon_0^2}|\alpha(\lambda)|^2, and \tag{1.9}$$

$$\sigma_{\text{abs}} = \frac{k}{\varepsilon_0}\text{Im}(\alpha(\lambda)), \tag{1.10}$$

where k is the wave vector, ε_0 is the permittivity of free space, and $\alpha(\lambda)$ is the polarizability of the metal nanosphere that is proportional to the cubic power of the particle radius r, given by

$$\alpha(\lambda) = 4\pi\varepsilon_0 r^3 \frac{\varepsilon_r(\lambda) - 1}{\varepsilon_r(\lambda) + 1}. \tag{1.11}$$

ε_r is the relative permittivity. The SPR measured extinction is dominated mainly by a strong absorption and little scattering as the nanospheres size go smaller. The larger the nanosphere, the more scattering contributes to the overall extinction at the given SPR peak.

Metal nanorods on the other hand, have two SPR peaks, which depends on the electric field orientation with respect to the nanorod axes. This means that these nanorods are polarization dependent. The absorption is maximized if the direction of the electric field is parallel with respect

to the long axis of the metal nanorod, and it is minimized when it is perpendicular to the axis, denoted as longitudinal SPR (LSPR). However, when the electric field hits along the short axis of the metal nanorod, it will delocalize the electrons resulting in a transverse SPR (TSPR), which is much weaker given the difference in rods dimensions. This TSPR results in both absorption and scattering with the TSPR peak located at a different part of the optical spectrum compared to the LSPR, as demonstrated in Fig. 1.6(a). Another interesting feature of the plasmonic metal nanoparticles is the SPR coupling between two, or more, interacting metal nanoparticles. This coupling decays with the inter-particle separation that is equal to or larger than the particle size. Briefly, when the nanorods are close to one another and assembled in a head-tail configuration, for example, as if they elongate the particle, they would result in a coupling and the LSPR will experience a red-shift. However, having the particles approach one another in a side by side assembly, and given the proximity in their size, it would result in coupling and the TSPR experiencing a blue-shift relative to the original peak. [33] Methods like discrete dipole approximation (DDA), [34] can be used to calculate the coupling, for example, and compare it with experimental results. This method relies on discretizing the nanoparticle into large enough numbers of dipoles and then calculating the interaction of each dipole with the light and its interactions with other dipoles around it. For example, DDA may assist in simulating the spectra of the coupled nanoparticle pairs.

1.4.2 Synthesis of GNRs

Gold nanoparticles come in many different shapes with different synthesis methods, i.e. spheres, rods, stars, etc. However, this work focuses on utilizing gold nanorods (GNRs) and explores different coatings so that the reactive gold nanorods can be more efficient and controlled through different surface treatment to incorporate them in nematic LCs and make them better candidates for applications such as enhancing optical and electro-optical properties of these new composites. Surface chemistry plays an important role in the functionalization of GNRs. GNRs are synthesized via numerous chemical methods. The most common method, however, is the seed mediated method that consists of two steps, established by Elsayed and Murphy groups. [35, 36] It

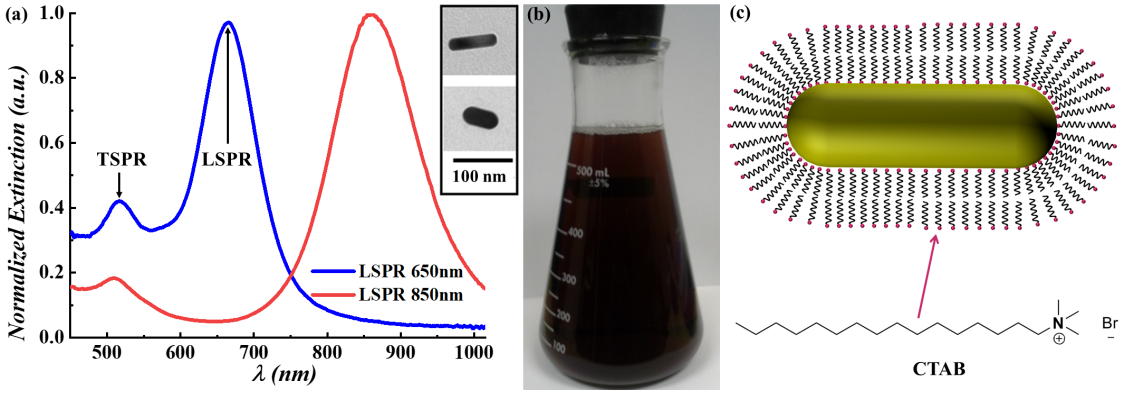

Fig. 1.6: (a) A representation of the optical spectra of GNRs with arrows indicating the TSPR and the LSPR in short GNRs spectra dispersed in water (blue), and another long GNRs (red). The inset shows a TEM image with the corresponding GNRs dimensions. (b) The final solution of GNRs synthesized following a seed mediated method, the GNRs appear brown reflecting long GNRs with LSPR close to the near IR (900 nm; the TSPR is responsible for the coloration. (c) A schematic showing CTAB arrangement around the GNR, with the hydrophobic tail pointing inwards avoiding contact with the solute (water), and the hydrophilic head group in contact with the solute.

involves a seed growth step followed by a growth step in solution. Tuning chemicals concentration and using the assistance of a cationic surfactant hexadecyltrimethylammonium bromide (CTAB), as well as adjusting the pH plays a rule in controlling the dimensions and the aspect ratio (AR) of theses GNRs. [37, 38] First, the seed solution was prepared by reducing 5ml of Hydrogen tetrachloroaurate ($HAuCl_4 3H_2O$, 0.5 mM) with 0.6 ml ice-cold sodium borohydride ($NaBH_4$, 10 mM), in the presence of 5 ml of CTAB (0.2 M). The seed is kept under vigorous stirring for two minutes (1k rpm). It is then left at room temperature for at least half an hour before use to make sure that the borohydride ions are fully decomposed.

The GNRs growth process starts by reducing the Hydrogen tetrachloroaurate through chemical reduction methods by using weak reducing agent (ascorbic acid, AA), which does not reduce the gold to its full metallic state, but rather to Au^+. This is indicated by the growth solution turning from yellowish-brown into a clear solution after adding the AA. The next step is adding the silver nitrides and hydrochloric acid (HCL), followed by the addition of the seed. The solution is then

left over night. Fig. 1.6(b) shows the final solution of GNRs with LSPR 900 nm. The amounts used here can be tuned depending on the desired size of the GNRs, or the desired LSPR, as will be established in later chapters. The seed acts as a catalyst to further reduce the gold to Au^0 and gradually assemble more gold onto the seed and eventually change its shape from quasi-spherical to rod-like with the assistance of silver nitrate and CTAB. The asymmetry is first produced by regulating the presence of silver cations in the solution. [36] The silver ions contribution to the AR depends on the chemical environment. For example, with higher concentration of silver ions, higher AR is achieved in an acidic medium, but the reverse is observed without any acid addition as it shortens the GNRs. [39] However, tuning the pH is crucial for not only the AR of the GNRs but also its morphology, and it reduces the CTAB adsorption on certain surfaces on the growing gold seed. [40] The asymmetry is further assisted with bi-layer CTAB forming around the GNRs, as demonstrated in Fig. 1.6(c). As CTAB act as a template guiding the growth of the GNRs, since it binds more strongly to (110) facets of the gold crystal of the seed, while more gold atoms deposit on the (100) and (111) facets, since these surfaces have less surface energy, and they are more stable for the gold deposition. The GNRs are usually stored after centrifuging the particles to separate from the byproducts and filter out undesired shapes, such as gold nanospheres, by changing the centrifuge speed. Then the precipitates of GNRs are then stored in a concentrated solution that is reduced in volume approximately 50 times the original water based solution during the synthesis and can be stored at room temperature until needed.

Surface functionalization of GNRs is another interesting process that assists GNRs to become more active components in experiments with a goal of utilizing properties of GNRs and adapt these plasmonic particles to their new environments, and it is widely followed in many research areas. LCs for example, are organic materials, and it would require exchanging the unstable bilayer CTAB into a more stable layer of coating around the GNRs in order to disperse in the LC without aggregations. For example, PEGylation, or the coupling of the GNRs with polyethylene glycol (PEG) of GNRs is processed via the Sulphur of the thiol groups (SH groups), since the gold surfaces, Au(111) for

example, have high affinity to thiol groups as well as disulfide with a semi-covalent interaction with the gold of approximately 45kcal/mol bond strength. [41] Likewise, there is many other stable layers that can be formed around the GNR in the hope of achieving certain adaptation or alignments. For example, Silica porous layer followed a fictionalized polymer, dimethyloctadecyl[3-(trimethoxysilyl) propyl] ammonium chloride (DMOAP), to help induce different alignment of the GNRs in the LC. More details on PEGylation or Silica formation on GNRs will be provided in chapters two and three.

1.4.3 Characterization of the GNRs

It is very useful to characterize GNRs by checking their optical spectra. Some information of the plasmonic GNRs can be deduced from their extinction spectrum. The extinction spectrum is typically measured using a set of USB2000-FLG (Ocean Optics), which is mounted on a microscope as well as an Integrating Sampling System (ISS-2, Ocean Optics) as a light source. For example, the full width at half maximum (FWHM) of the LSPR help identifies whether or not the GNRs are mono- or poly-dispersed. If the FWHM is around 100 nm wide for short GNRs, then it is indicative of monodispersed GNRs solution. This is slightly larger for longer GNRs ($\sim$ 150-200 nm). The position of the TSPR directly relates to the diameter, as well as the yield of rods to spheres. Transmission electron microscopy (TEM) is another characterizing tool requires high electron density in the specimen measured. Therefore, it is not good for organic materials, however it is excellent to characterize GNRs for imaging their shape and dimensions. Images in this work were obtained with two different TEM, the FEI Tecnai T12 Spirit and the CM100 microscope (FEI Philips). The TEM mainly uses electromagnetic lenses to focus the electron beam into a very sharp point or spread it out as needed, which travels through the TEM grid under study, and the image can be seen in an eye piece or on the screen and can be further adjusted to get the best magnification and highest resolution. To image GNRs, centrifugation of the synthesized GNRs solution is necessary to remove undesired byproducts, such as CTAB or excess Silica after coating these particles, which may influence the quality of the TEM image. It is best to centrifuge the

GNRs solution twice. Short GNRs are typically centrifuged at faster speed (9000 rpm) compared to long GNRs (7000 rpm) for 15-20 minutes, given the heaviness of the later. After that, the GNRs were re-dispersed in deionized (DI) water after which a droplet of the solution was deposited on the TEM copper grid and left to dry before imaging. The collected images from the TEM were then processed using a software to measure the dimensions of nanoparticles, mainly ImageJ. 30-50 particles are roughly a good estimate to give the distribution of a given GNRs sample. Measuring the optical density (OD) of the new GNRs suspension is useful in knowing the concentration of the GNRs present, and then deciding whether more packed GNRs are needed in the image or more spaced out and hence dilute the sample more.

1.5 Brief overview of literature

GNRs have been extensively investigated for use in a wide range of practical applications, and a key element for this usage is incorporating GNRs into different matrices such as polymers, gels, glasses, etc. The sensitivity of the SPR to the medium around the GNRs makes it ideal for sensing applications for example [45]. One of the main advantages of GNRs is enabling the anisotropic optical properties through their polarization dependence by aligning them in an ordered medium such as LCs [1]. The formation of polarizers due to a collective presence of plasmonic GNRs was extensively investigated, and it is mainly exploited in the field of optoelectronics. However, the polarization dependence of GNRs is only present in a certain spectral window depending on the LSPR peak of the GNRs.

Zhang *et al*, for example, demonstrate that GNRs doped polymer, Poly(Vinyl Alcohol) (PVA), can exhibit polarization dependence when the polymer is stretched forcing the GNRs to align along the stretching direction. [44] While the polymer doped GNRs can successfully produce a film that is polarized and flexible, these have the drawback of being non-switchable and maintaining a fixed state. LCs, on the other hand, allow for switching between a polarization dependent state and a clear state. This can allow the control of light transmittance. Q. Liu et al, [1] for example, developed a prototype of electrically and optically tunable cell of LC doped with

GNRs of about square inch area, which in principle can be extended to one square meter area as will be discussed in chapter 6. Further investigations of changing surface treatment of the GNRs doped in the LC lead to interesting optical properties. [2] The LC medium also offers a variety of options, ranges from cholesteric LCs, and LCs with negative or positive dielectric anisotropy, etc. And incorporating GNRs in these different LCs would assist with modulating the light through the complex unique properties of both the LCs and GNRs, and may offer a wide range of potential applications. Namely thermotropic liquid crystals that can be switched with weak external stimuli, and by combining different nanoparticles in thermotropic liquid crystals, a new colloidal liquid crystals emerge of nanocomposites that are sustainable and with collective properties, which can be useful for a variety of applications.

1.6 Thesis Objective

Liquid crystals are extensively studied in research and widely commercialized it have become essential in our everyday life. Liquid crystals function as a platform particularly for nanoparticles, resulting in a new field that studies anisotropic soft matter materials with unique properties. Particularly, thermotropic liquid crystals that can be switch between different states with a weak external stimuli.

The motivation of my work is to identify new materials with refined properties by creating complex systems of different nanoparticles and incorporating them in thermotropic liquid crystals. Combining the properties of the liquid crystals with weak responsiveness and the ability to be switched at very low values of applied external forces, and the properties of nanoparticles leads to identifying different implementation of ways to reproduce renewable energy with materials that are newer, cheaper, sustainable, and environmentally friendly. Additionally, my work allows for investigating and better understanding the fundamental science behind new phenomena, such as the mechanical coupling between gold nanorods and quantum dots as demonstrated later on.

This research is distinguished from earlier work because the different nanoparticles used are formed from materials that are composed by following a bottom-up approach and then incorpo-

rated into the liquid crystal to design new tunable nanostructured composites mainly through self-assembly. In particular, I study anisotropic plasmonic nanoparticles, often referred to as gold nanorods, throughout this thesis, which modulate the energy flow at any given band of the light spectrum through synthetic tuning. In addition, gold nanorods may enhance the electric field close to their edges, a property that enables them to function as nano-antennas and can further exploited to enhance the luminescence of different nanoparticles, such as quantum dots, up-conversion nanoparticles, etc.

In this thesis, I will focus on investigating different composites of co-dispersion of nanoparticles in liquid crystals. This work can be divided in three main areas of studies. The first area investigates co-dispersing gold nanorods with different surface fictionalization and different sizes simultaneously doped in the same liquid crystal medium. This study creates bleach-less broad band polarization dependent systems, and can further be refined to incorporate dyes with the gold nanorods, where the dye modulate the light in the visible region, while the gold nanorods can be tuned to absorb light in the near infrared region of the light spectrum. This part of the study allows researchers to alter the light in different bands of the spectrum simultaneously, or alternatively, depending on the fictionalization of the particles, resulting in a huge impact in modulating energy consumptions if it were implemented in the industry as will be discussed in the last chapter. Another area of study involves studying single particle interaction between a plasmonic gold nanorod with another nanoparticle, such as quantum dot or up-conversion nanoparticle, all in the same liquid crystal medium, which allows the investigation of optical characterization, for example. And the last area of study addresses super nanostructures of gold nanorods that can be formed through depletion driven self-assembly.

The layout of this thesis is arrayed chronologically based on the above studies. The first chapter presents the fundamentals of liquid crystals and followed by an illustration of plasmonic gold nanoparticles, their properties, and synthesis methods. An overview of previous work is presented next, leading to the motivation behind the proposed studies in the thesis overview. The following chapter outlines experimental details demonstrating a system that allows for controlling the optical

properties of plasmonic mesostructured composites though the alignment of polarized surface plasmon resonance modes of nanoparticles with different shapes and compositions co-dispersed within an ordered thermotropic LC host allowing the engineering of the physical behavior of self-assembled optical metamaterials. Chapter three consists of a subsequent project on designing mesostructured composites by co-doping dichroic dyes and anisotropic plasmonic nanoparticles in both nematic and cholesteric LCs, where these composites exhibit facile and unique switching allowing the control over light transmission in the near-IR and visible spectral ranges, which can be implemented in many possible applications such as smart and privacy windows. Chapter four establishes a new study that controls the quantum mechanical effects of a core/shell quantum dots utilizing a coupling effect between the quantum dot and two neighboring plasmonic particles utilizing a liquid crystal defect line with the assistance of laser tweezers to push the plasmonic particles towards the quantum dot, illustrating the plasmonic coupling phenomena and how the plasmonic particles work as antennas improving the luminescence yield of these quantum emitters. Chapter five is dedicated to the study of self-assembled nanostructures of GNRs through entropic driven forces. The last chapter explores future opportunities for different projects that stem from perspective of this work. Overall, this work sets the stage for new, cheaper, and more efficient adaptive technologies, including those that convert energy, presenting a fertile ground for new basic scientific work, as well as providing new directions and methods to explore possibilities for new alternatives in renewable and sustainable energy.

1.7 References

[1] Q. Liu, Y. Yuan, I. I. Smalyukh, "Electrically and optically tunable plasmotic guest-host liquid crystals with long-range ordered nanoparticles," *Nano Lett.*, 2014 **14** 4071.

[2] Y. Zhang, Q. Liu, H. Mundoor, Y. Yuan, I. I. Smalyukh, "Metal nanoparticle dispersion, alignment and assembly in nematic liquid crystals for applications in switchable plasmonic color filters and E-polarizers," *ACS Nano*, 2015 **9** 3097.

[3] H. Mundoor, B. Senyuk, I. I. Smalyukh, "Triclinic Nematic Colloidal Crystals from Competing Elastic and Electrostatic Interactions," *Science*, 2016 **352** 69.

[4] O. Lehmann, "Die Struktur krystallinischer Flssigkeiten," *Zeitschrift für Physikalische Chemie*, 1889 **4** 462.

[5] Q. Liu, Y. Cui, D. Gardner, X. Li, S. He, and I. I. Smalyukh. "Self-alignment of plasmonic gold nanorods in reconfigurable anisotropic fluids for tunable bulk metamaterial applications," *Nano Lett.*, 2010 **10** 1347.

[6] Y. Yuan, I. I. Smalyukh, "Topological nanocolloids with facile electric switching of plasmonic properties," *Opt. Lett.*, 2015 **40** 5630.

[7] G. H. Sheetah, Q. Liu, I. I. Smalyukh, "Self-assembly of Predesigned Optical Materials in Nematic Codispersions of Plasmonic Nanorods," *Optics Letters*, 2016 **41** 4899.

[8] G. H. Sheetah, Q. Liu, B. Senyuk, B. Fleury, I. I. Smalyukh, "Electric switching of visible and infrared transmission using liquid crystals co-doped with plasmonic gold nanorods and dichroic dyes," *OPTICS EXPRESS*, 2018 **26** 22264.

[9] H. Mundoor, G. H. Sheetah, S. Park, P. J. Ackerman, I. I. Smalyukh, J. van de Lagemaat "Tuning and switching a plasmonic quantum dot sandwich in a nematic line defect," *ACS NANO*, 2018 **12** 2580.

[10] A. Bhattacharyya, "Fluorescence labelling of biologically important molecules," *Ind. J. Biochem. Biophys.*, 1986 **23** 171.

[11] D. Demus, J. Good, G. W. Gray, H.W. Spiess, V. Vill, "Handbook of liquid crystal sets," *WILEYVCH Verlag GmbH*, 1998.

[12] K. G. Thomas, S. Barazzouk, B. I. Binil Itty Ipe, S.T.S. Joseph, P. V. Kamat, "Uniaxial Plasmon Coupling through Longitudinal Self-Assembly of Gold Nanorods," *J. Phys. Chem. B*, 2004 **108** 13066.

[13] P. K. Jain, S. Eustis, M. A. El-Sayed, "Plasmon Coupling in Nanorod Assemblies: Optical Absorption, Discrete Dipole Approximation Simulation, and Exciton-Coupling Model," *J. Phys. Chem. B* 2006 **110** 18243.

[14] F. Wang, Y. Han, C.S. Lim, Y. Lu, J. Wang, J. Xu, H. Chen, C. Zhang, M. Hong, X. F. Liu, "Simultaneous phase and size control of upconversion nanocrystals through lanthanide doping," *Nature*, 2010 **463** 1061.

[15] X. Ye, C. Zheng, J. Chen, Y. Gao, C.B. Murray, "Using binary surfactant mixtures to simultaneously improve the dimensional tunability and monodispersity in the seeded growth of gold nanorods," *Nano Lett.*, 2013 **13** 765.

[16] B. Nikoobakht, M. A. El-Sayed, "Preparation and growth mechanism of gold nanorods (NRs) using seed-mediated growth method," *Chem. Mater*, 2003 **15** 1957.

[17] L. Wang, "Controlled Synthesis and Luminescence of Lanthanide Doped NaYF4 Nanocrystals," *Chem. Mater.*, 2007 **19** 727.

[18] W. C. Wu, J. B. Tracy, "Large-Scale Silica Overcoating of Gold Nanorods with Tunable Shell Thicknesses," *Chem. Mater*, 2015 **27** 2888.

[19] S. Link, Z. L. Wang, M. A. El-Sayed, "Alloy Formation of GoldSilver Nanoparticles and the Dependence of the Plasmon Absorption on Their Composition," *J. Phys. Chem. B*, 1999 **103** 3529.

[20] H. K. Bisoy, S. Kumar, "Liquid-crystal nanoscience: an emerging avenue of soft self-assembly," *Chem. Soc. Rev.*, 2011 **40** 306.

[21] B. Senyuk, D. Glugla, I. I. Smalyukh, "Rotational and translational diffusion of anisotropic gold nanoparticles in liquid crystals controlled by varying surface anchoring," *Phys. Rev. E*, 2013 **88** 062507.

[22] B. Bahadur, "Handbook of Liquid Crystals," *Wiley-VCH*, Weinheim, 2A, 1998.

[23] P. M. Chaikin, T. C. Lubensky, "Principles of condensed matter physics," *Cambridge Univ. Press*, 2000.

[24] L. M. Blinov, V. G. Chigrinov, "Electrooptic effects in liquid crystal materials," *Springer-Verlag, New York*, 1996.

[25] M. Bass, C. DeCusatis, J. M. Enoch, V. Lakshminarayanan, G. Li, C. MacDonald, V. N. Mahajan, E. Van Stryland, "Handbook of optics", *McGraw-Hill, New York*, 1995.

[26] F. C. Frank, "On the Theory of Liquid Crystals," *Discussions of the Faraday. Society,* 1958 **25** 19.

[27] J. Li, C. H. Wen, S. Gauza, R. Lu, S. T. Wu, "Refractive indices of liquid crystals for display applications," *J. Disp. Technol.*, 2005 **1** 51.

[28] S. Ishihara, "How far has the molecular alignment of liquid crystals been elucidated?," *IEEE/OSA Journal of Display Technology,*, 2005 **1** 30.

[29] V. S. U. Fazio, L. Komitov, C. Radüge, S. Lagerwal, H. Motshmann, "Influence of the flow on the anchoring of nematic liquid crystals on langmuir-blodgett monolayers studied by optical second-harmonic generation," *Eur. Phys. J. E*, 2001 **5** 309.

[30] A. M. Funston, C. Novo, T. J. Davis, P. Mulvaney, "Plasmon coupling of gold nanorods at short distances and in different geometries.", *Nano Lett.*, 2009 **9** 1651.

[31] L.S. Slaughter, W.-S. Chang, P. Swanglap, A. Tcherniak, B. P. Khanal, E. R. Zubarev, S. J. Link, "Single-Particle Spectroscopy of Gold Nanorods beyond the Quasi-Static Limit: Varying the Width at Constant Aspect Ratio." *Phys. Chem. C*, 2010 **114** 4934.

[32] A. S. Stender, G. Wang, W. Sun, N. Fang, "Influence of Gold Nanorod Geometry on Optical Response," *ACS Nano*, 2010, **4**, 7667.

[33] P.K. Jain and M. A. El-Sayed, "Surface Plasmon Coupling and Its Universal Size Scaling in Metal Nanostructures of Complex Geometry: Elongated Particle Pairs and Nanosphere Trimers," *J. Phys. Chem. C*, 2008 **112** 4954.

[34] B. T. Draine, P. J. Flatau, "Discrete-Dipole Approximation for Scattering Calculations," *J. Opt. Soc. Am. A*, 1994 **11** 1491.

[35] B. Nikoobakht, M. A. El-Sayed, "Preparation and growth mechanism of gold nanorods (NRs) using seed-mediated growth method," *Chem. Mater*, 2003 **15** 1957.

[36] N. R. Jana , L. Gearheart , C. J. Murphy, "Seed-Mediated Growth Approach for ShapeControlled Synthesis of Spheroidal and Rodlike Gold Nanoparticles Using a Surfactant Template," *Adv. Mater.*, 2001 **13** 1389.

[37] X. Ye, C. Zheng, J. Chen, Y. Gao, C. B. Murray, "Using binary surfactant mixtures to simultaneously improve the dimensional tunability and monodispersity in the seeded growth of gold nanorods," *Nano Lett.*, 2013 **13** 765.

[38] T. K. Sau, C. J. Murphy, "Seeded High Yield Synthesis of Short Au Nanorods in Aqueous Solution," *Langmuir*, 2004, **20**, 6414.

[39] J. O. Park, S.-H. Cho, D.-Y Jeong, Y.-M Kong, S. Y. Lee, "Effects of chloride and silver ions on gold nanorod formation," *Jpn. J. Appl. Phys.*, 2015 **54** 019202.

[40] J. Cheng, L. Ge, B. Xiong, Y. He, "Investigation of pH Effect on Gold Nanorod Synthesis," *Journal of the Chinese Chemical Society*, 2011 **58** 822.

[41] H. Groenbeck, A. Curioni, W. Andreoni, "Thiols and disulfides on the Au(111) surface: the headgroup-gold interaction," *J Am Chem Soc*, 2000 **122** 3839.

[42] L. Vigderman, E.R. Zubarev, "High-Yield Synthesis of Gold Nanorods with Longitudinal SPR Peak Greater than 1200 nm Using Hydroquinone as a Reducing Agent," *Chem. Mater.*, 2013 **25** 1450.

[43] P. K. Jain, W. Huang, M.A. El-Sayed, "On the Universal Scaling Behavior of the Distance Decay of Plasmon Coupling in Metal Nanoparticle Pairs: A Plasmon Ruler Equation Prashant" *Nano Lett.*, 2007 **7** 2080.

[44] H. Zhang, J. Zhang, X. Tong, D. Ma, Y. Zhao, "Light PolarizationControlled ShapeMemory Polymer/Gold Nanorod Composite," *Macromolecular rapid communications*, 2013 **34** 1575.

[45] A.J. Haes, D.A. Stuart, S. Nie, R.P. Van Duyne, "Using solution-phase nanoparticles, surface-confined nanoparticle arrays and single nanoparticles as biological sensing platforms", *J. Fluoresc.*, 2004 **14** 355.

Chapter 2

Self-assembly of predesigned optical materials in nematic codispersions of plasmonic nanorods

Adapted from:Optics Letters. 2016, **41**(21) 4899-4902.

Chapter Overview

Optical metamaterials and other nanostructured metal-dielectric composites hold a great potential for designing and practically realizing novel types of light-matter interactions. Here we develop an approach to fabricate composites with tunable pre-engineered properties via self-assembly of anisotropic nanoparticles codispersed in a nematic liquid crystal host. Orientations of plasmonic nanorods of varying aspect ratios are controlled to align parallel or perpendicular to the nematic director and retain this relative orientation during a facile electric switching. The ensuing dynamic re-configurability of the surface plasmon resonances of a composite enables previously inaccessible means of controlling light and may enable tunable plasmonic filters and polarizers.

2.1 Introduction

Nematic LC colloids, formed by particles dispersed in a LC host fluid, provide a soft matter platform for designing novel composite materials with interesting optical properties [3]. This approach of designing mesostructured functional materials with novel physical behavior often com-

bines unique optical properties of solid nanoparticles with long-range ordering and facile response of the soft matter to weak external stimuli. The design and practical realization of diverse types of orientationally ordered nematic LC dispersions of nanoparticles is enabled by rich and highly complex LC-nanoparticle interactions on hierarchical scales ranging from nanometers to device scales. The LC-mediated ordering of particles can emerge from elastic or surface-anchoring-based interactions, or a combination of both. Recent studies have demonstrated spontaneous self-alignment of nanoinclusions such as rods, platelets, and topologically nontrivial colloidal objects [3]. However, despite the tremendous recent progress [6], the facile wet-chemistry-based synthesis approaches yield a limited variety of shapes and compositions of nanoparticles, which, in turn, limits the prospects for the design of properties of nanoparticles dispersed within the ordered switchable composites.

In this work, we describe an approach of codispersing different anisotropic nanoparticles in LCs to design and realize composite materials with pre-engineered surface plasmon resonances (SPRs) and electrically tunable optical properties that could not be fabricated otherwise. To illustrate the power of this approach, we use rod-like gold nanoparticles of aspect ratios and different treatment of surfaces codispersed within the same nematic LC host. The nanorods of different types are controlled to align along the same direction of the nematic LC director **N** or in the mutually orthogonal directions, with one type of nanorods orienting parallel to **N** and the other type of rods orienting orthogonally to **N**. When low-voltage fields switch **N**, nanorods are slave to changes of the **N**-orientation [2–4], rotating with their long or short nanorod axes mechanically coupled to **N** and thus enabling unprecedented tunability of SPR spectra and polarization-dependent optical properties of the ensuing composites. We characterize the threshold-like behavior of the electric switching of the composites, as well as the response times and other characteristics. We conclude with a discussion of potential practical uses of LC-nanoparticle codispersion composites in practical applications [7], such as tunable broadband polarizing elements and optical filters.

2.2 Methods and discussion

Aqueous dispersions of gold nanorods (GNRs) with mean diameters and lengths of 22×50 nm (short GNRs, SGNRs) and 21×80 nm (long GNRs, LGNRs) were synthesized using seed-mediated methods [8, 9]. Before surface functionalization of GNRs aimed at defining boundary conditions (anchoring) for the LC molecules, the excess surfactant hexadecyltrimethylammonium bromide (CTAB, Sigma-Aldrich) initially used during synthesis of GNRs was removed. To define the tangential alignment of LC molecules and **N** on the surface of GNRs, we functionalized both SGNRs and LGNRs by thiol-terminated methoxy-poly(ethylene glycol) (mPEG-SH, JemKem Technology) (Fig. 2.1(a)) following the literature [4]. To achieve the homeotropic anchoring of LC molecules and N on the GNR surface, SGNRs were first capped with 10 nm-thick mesoporous silica and then surface-functionalized by N,N-dimethylN-octadecyl-3-aminopropyltrimethoxysilyl chloride (DMOAP, 60% in methanol, from Acros Organics) (Fig. 2.1(c)) [3, 10]. Briefly, 50 μl of a 0.1 M aqueous NaOH solution were added (under vigorous stirring) to a 5 ml of aqueous dispersion of GNRs with optical density (OD) of 4.7 and 1.1 mM CTAB. Then 700 μl of 0.25 vol. % tetraethyl orthosilicate (Sigma-Aldrich) in ethanol were added with gentle stirring for 0.5 h and kept undisturbed for 14 h. After washing with centrifuging twice, 4 ml of GNRs solution with OD of 2.3 was diluted to 8 ml and then 400 μl of DMOAP was injected under stirring. The solution was kept stirred for 20 min and washed by repeated centrifugation and transferred into methanol. Capped GNRs were redispersed in methanol and mixed with a nematic 4-cyano-4′-pentylbiphenyl (5CB, from Chengzhi Yonghua Display Materials Co. Ltd.), followed by full evaporation of the solvent at 90 °C. The mixture was sonicated for 5 min at 40 °C and cooled down to the nematic phase while vigorously stirring, yielding excellent dispersion in the LC phase at a high concentration. The codispersion of SGNRs and LGNRs with designed cappings were obtained by mixing them as dispersions with comparable ODs. LC cells were constructed from 0.17 or 1.0 mm-thick glass substrates coated with transparent indium tin oxide electrodes and polyvinyl alcohol (PVA) alignment layers. Their inner surfaces with PVA layers were unidirectionally rubbed to impose the

planar surface boundary conditions for the far-field director $\mathbf{N_0}$ parallel to the rubbing direction. The LC-nanoparticle composite was sandwiched between two such plates, with the cell gap defined by silica beads or Mylar spacers of corresponding diameters/thickness. Capillary action was used for the cell filling with the composite colloidal dispersion. UV-curable glue NOA-65 (Norland Products, Inc.) was used to bind the substrates together and to seal the cell edges.

We used Olympus BX-51 polarizing optical microscope equipped with 10×, 20×, and 50× air objectives with numerical aperture NA= 0.30.9 and a charge coupled device camera Spot 14.2 Color Mosaic (Diagnostic Instruments, Inc.). Extinction spectra were studied using a spectrometer USB2000-FLG (Ocean Optics) mounted on the microscope and an Integrating Sampling System (ISS-2, Ocean Optics) as a light source. The polarized SPR spectra were measured by having light pass through the LC cell and then through a broadband ($400-1200$ nm) rotatable polarizer. Dark field imaging utilized an oil-immersion dark-field condenser (NA= 1.2), so that only highly scattered light was detected. Electric switching of codispersions was characterized using a data acquisition system SCC-68 (National Instruments Co.) controlled by homemade software written in Labview (National Instruments Co.) and a Si amplified photodetector PDA100A (Thorlabs Inc.). Our selective studies of switching of different GNRs in LC was done in the vicinity of their longitudinal SPR wavelengths and utilized band-pass optical interference filters procured from Semrock Inc. Transmission electron microscopy (TEM) images were obtained using a CM100 microscope (FEI Philips). Since the wet chemical synthesis and other means of facile fabrication of metal nanostructures provide only limited control of the ensuing SPR properties [6,7], colloidal self-assembly of simple-shape nanoparticles (like spheres, rods, and platelets) into more complex plasmonic nanostructures has been broadly considered as means to mitigate these limitations [7–13]. The enrichment of the SPR effects could be achieved through coupling of SPR modes of individual nanoparticles upon their assembly into clusters, crystals, and other colloidal superstructures [7]. However, these approaches are typically limited to colloidal self-assemblies with nanoparticles at distances comparable to their dimensions. In dilute nanoparticle dispersions, such control is limited. Although multiple types of

plasmonic nanoparticles, such as GNRs with different aspect ratios (Fig. 2.1), can be codispersed in isotropic fluid hosts (Fig. 2.1(e)), the extinction spectra of such dilute codispersions are usually just superpositions of those due to the individual constituent nanoparticle dispersions with a very limited ability of controlling them. In this work we use an example of codispersions of LGNRs and SGNRs in a nematic host to demonstrate that spontaneous pre-designed self-alignment of either long (Fig. 2.1(b)) axes or short and long axes (Fig. 2.1(d)) of SGNRs and LGNRs with the LC director $\mathbf{N}$ allows us to pre-engineer the ensuing composite mediums optical properties through exploiting the polarization-dependent SPR resonances of aligned nanoparticles.

SGNRs and LGNRs functionalized by mPEG self-align with their long axes roughly parallel to $\mathbf{N}$ (Fig. 2.1(b)). This spontaneous alignment is reminiscent to that of individual dispersions of SGNRs and LGNRs in LCs [2] and is driven by minimization of the surface anchoring free energy due to the finite-strength tangential boundary conditions on nanoparticle surfaces. Polarizing optical microscopy (Figs. 2.2(a,b)) shows that GNRs do not perturb the uniform alignment of the LC host while dispersed at rather high concentrations up to 1.6 wt.%. Dark field imaging (Fig. 2.2(c)) of the SGNR and LGNR codispersion in the aligned LC reveals Brownian motion of the nanoparticles on individual basis, without forming aggregates, which was assessed on the basis of their diffusion [5]. Polarized extinction spectra have three peaks, one corresponding to the transverse SPR modes at 530 nm of both SGNRs and LGNRs and two peaks corresponding to the spectrally separated longitudinal SPR modes of the two types of nanorods. When the effects of relatively high polarization dependent effective refractive index of the LC host are accounted for, the spectral locations of all SPR peaks (Fig. 2.2(d)) appear consistent with those of the same GNRs in an isotropic host (Fig. 2.1(e)).

In a planar cell, the extinction spectra exhibit strong dependencies on polarization of light $\mathbf{P}$ and applied AC voltage U (at 1kHz), with the maximum extinction values at $\mathbf{P}\|\mathbf{N_0}$ corresponding to the two longitudinal SPR modes of the constituent GNRs. At $\mathbf{P}\|\mathbf{N_0}$, an extinction peak is located at the transverse SPR mode wavelength (Fig. 2.2(d)). The voltage dependence of light transmission through the cell exhibits a threshold-like behavior (Fig. 2.2(e)), showing no or little

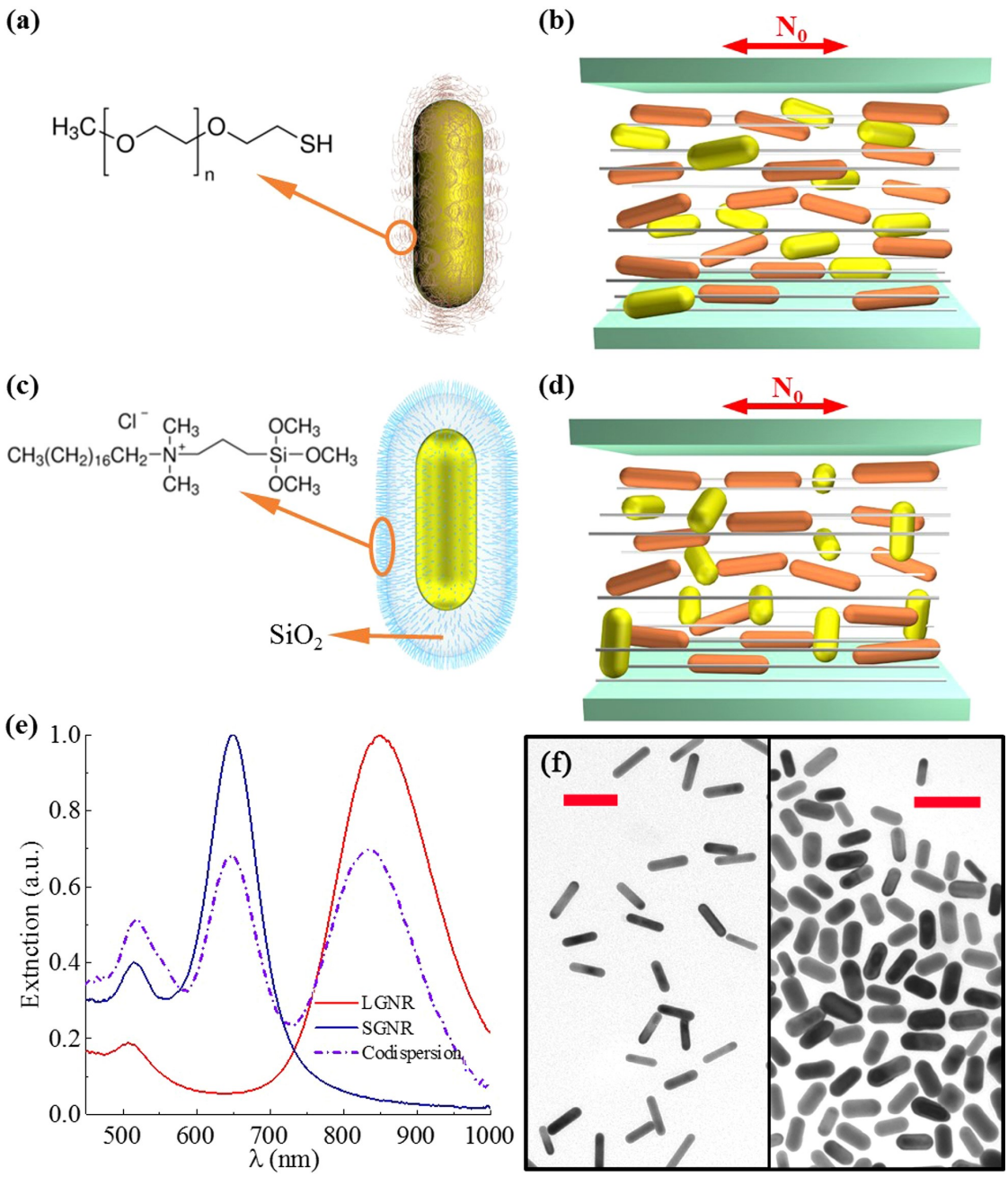

Fig. 2.1: Design of plasmonic nanocomposite materials and oriented self-assembly of codispersed GNRs. (a) Schematic of a GNR with the mPEG capping polymer layer on its surface. (b) Schematic of the codispersed GNRs with different aspect ratios but treated to define the same tangential anchoring for **N** on their surfaces. (c) Schematic of a GNR with the silica coating and DMOAP capping layer on its surface. (d) Schematic of the codispersed GNRs with different aspect ratios that are treated to define different, tangential or homeotropic, surface anchoring for **N**. (e) Extinction spectra of both SGNRs and LGNRs when separately and jointly dispersed in an isotropic solvent (ethanol) at a dilute total concentration of 0.6 wt.%. (f) TEM images of the long (left) and short (right) GNRs; the red scale bars are 100 nm.

change up to a threshold voltage $U_{\rm th}$ and then changing dramatically with the increase of U. This behavior is consistent with the U-dependent extinction spectra (Fig. 2.2(d)) and the synchronous field-induced realignment of $\mathbf{N}$ and GNRs schematically shown in the insets of Fig. 2.2(e). Since the longitudinal SPR modes are polarized along the long axes of the nanorods, extinction spectra allow us to determine the scalar order parameters, defined as

$$S_{\rm GNR} = (3\left\langle \cos^2\theta_{\rm GNR}\right\rangle - 1)/2, \tag{2.1}$$

characterizing the orientational order of both SGNRs and LGNRs. Using the peak extinction values $A_{\parallel}$ and $A_{\perp}$ of longitudinal SPR for $\mathbf{P}\|\mathbf{N_0}$ and $\mathbf{P}\perp\mathbf{N_0}$ and a relation

$$S_{\rm GNR} = (A - A_{\perp})/(A + 2A_{\perp}), \tag{2.2}$$

we find that the order of GNRs is characterized by $S_{\rm LGNR} = 0.58$ and $S_{\rm SGNR} = 0.50$, respectively.

The kinetics of electric switching of SGNRs and LGNRs is probed by using bandpass filters matching their longitudinal SPR peaks. Rising and decay times are found from relative changes of the transmitted light intensity between 10% and 90% with respect to their maximum and minimum values. The switching times of GNRs in the nanorod-LC codispersion are comparable to those of the pristine LCs, with the rising (voltage-on) times dependent on U, albeit the reorientation of LGNRs is slightly faster than that of SGNRs (Fig. 2.2(f-h)). This could be due to the relative strengths of mechanical coupling between $\mathbf{N}$ and the orientations of GNRs, which is stronger for LGNRs, consistent with $S_{\rm LGNR} > S_{\rm LGNR}$. The decay times (response to voltage off) are also comparable to what one expects for cells of a pristine LC with the same thickness $d = 30$ m [2]. The measured response time values (Fig. 2.2(g,h)) qualitatively agree with theoretical prediction for pristine LCs

$$\tau_{\rm rising} = \tau_{\rm decay}/[(U/U_{\rm th})^2 - 1], \tag{2.3}$$

where

$$\tau_{\rm decay} = \gamma_1 d^2/(K_{33}\pi^2) \tag{2.4}$$

is the decay time, γ_1 is the rotational viscosity, and $_{33}$ is the bend elastic constant. The insets of Fig. 2.2(f) show that the polarization dependence of the composites can be controlled in the same way over large areas of cells (demonstrated for inch-size cells, but can be scaled to meters, as long as the LC host can be aligned).

Fig. 2.3 shows a very different behavior of a codispersion of DMOAP-functionalized silica-coated SGNRs (inset of Fig. 2.3(a)) and mPEG-functionalized LGNRs in the same 5CB LC host. The homeotropic and tangential boundary conditions on SGNR and LGNR particle surfaces prompt their self-alignment perpendicular and parallel to $\mathbf{N_0}$, respectively (Fig. 2.1(d)), again driven by the minimization of the surface anchoring energy [2,3]. As the polarization of probing light is switched between $\mathbf{P}\|\mathbf{N_0}$ and $\mathbf{P}\perp\mathbf{N_0}$, the longitudinal SPR peaks due to the two GNRs alternate while varying between maximum and minimum values of extinction at the corresponding wavelengths. The finite S_{GNR}values characterizing the LC-induced order of both GNRs manifest themselves in that the longitudinal peaks of the two rods never disappear with rotating $\mathbf{P}$. Using the same approach as for the tangentially anchored rod codispersion, we determine the scalar order parameters to be $S_{\mathrm{LGNR}} = 0.65$ and $S_{\mathrm{SGNR}} = -0.31$, respectively. The polarized SPR spectra can be also controlled by applying voltage while switching $\mathbf{N}$ and having the orientation of $\mathbf{P}\|\mathbf{N_0}$ fixed (Fig. 2.3(b)) Both the alignment and switching can be controlled on centimeter square areas of the LC cells (insets of Fig. 2.3(c)). This can be extended to a much larger LC cell dimensions, such as that of large-screen TVs.

The threshold-like switching of the cells (Fig. 2.3(d)) manifests itself very differently when probed separately at the wavelengths of longitudinal SPR modes of the two GNRs. The transmitted intensity at the SGNRs longitudinal SPR mode wavelength stays intact with increasing U up to Uth, but then decreases continuously above it (Fig. 2.3(d)). The transmitted intensity at the LGNRs longitudinal SPR peak wavelength stays intact with increasing U up to U_{th}, but then increases continuously at $U > U_{\mathrm{th}}$ (Fig. 2.3(d)). This behavior is consistent with the switching of $\mathbf{N}$ from its initial in-plane orientation to the vertical orientation and the ensuing realignment

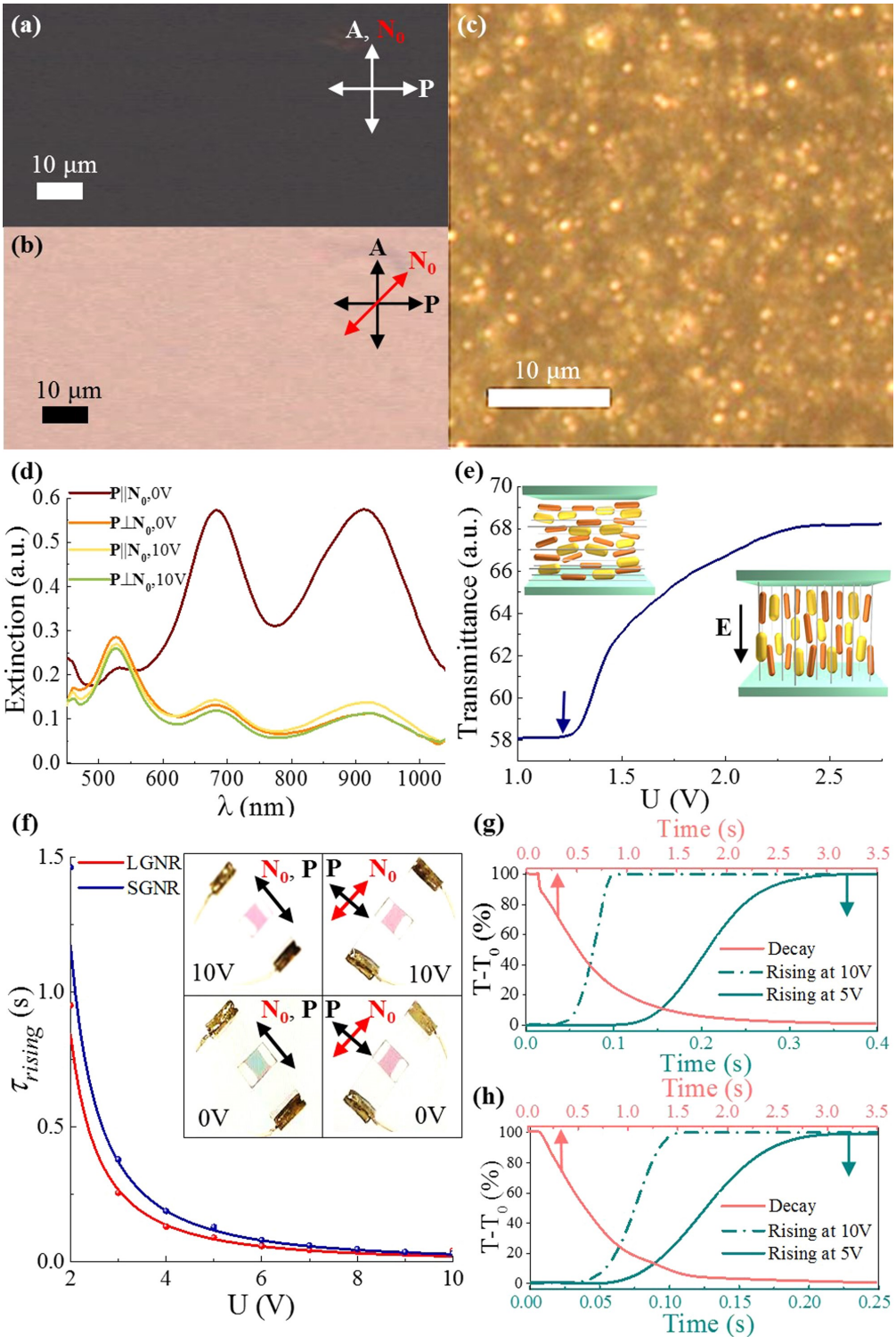
(a)
A, N0
P
10 μm
(b)
A
N0
P
10 μm
(c)
10 μm
(d)
P||N0,0V
P⊥N0,0V
P||N0,10V
P⊥N0,10V
Extinction (a.u.)
λ (nm)
(e)
Transmittance (a.u.)
U (V)
E
(f)
LGNR
SGNR
τrising (s)
U (V)
N0, P
P N0
10V
0V
(g)
Time (s)
T-T0 (%)
Decay
Rising at 10V
Rising at 5V
(h)
Time (s)
T-T0 (%)
Decay
Rising at 10V
Rising at 5V
Time (s)

Fig. 2.2

Fig. 2.2: Codispersion, coalignment and switching of like-anchored GNRs in a nematic LC. (a,b) Polarizing optical micrographs of a planar cell with $\mathbf{N_0}$ (a) parallel to analyzer ($\mathbf{A}$), and (b) at 45° to crossed polarizer ($\mathbf{P}$) and $\mathbf{A}$. (c) Dark field micrograph of a cell with $\mathbf{N_0}$ along its horizontal edge. (d) Polarized extinction spectra of the cell for linear polarizations $\mathbf{P}\|\mathbf{N_0}$ and $\mathbf{P}\perp\mathbf{N_0}$ at no applied fields and at applied voltage $U = 10$V. (e) Voltage dependence of transmittance of white light polarized along the rubbing direction measured using a microscope, with the threshold voltage marked by an arrow. (f) Voltage-dependent rising time for both types of GNRs. The insets show photographs of the inch-size cells at different orientations of $\mathbf{N_0}$ relative to $\mathbf{P}$. (g,h) Rising and decay times for (g) SGNR and (h) LGNR dispersions measured based on relative changes of transmittance $(T - T_0)$ for the same codispersion sample by using optical band-pass filters corresponding to their longitudinal SPRs. The cell thickness is 30 μm.

LGNRs and SGNRs that maintain their orientations relative to U-controlled $\mathbf{N}$ (insets of Fig. 2.3(d)). Interestingly, $U_{\rm th}$ is slightly lower than that measured for the codispersion with both LGNRs and SGNRs aligned along $\mathbf{N}$ (Fig. 2.2(e)). The time response characteristics (Fig. 2.3(e,f) are qualitatively consistent with those of pristine LCs and the plasmonic guest-host LCs, albeit the response times for SGNRs are slower than for LGNRs.

2.3 Results and Conclusions

The above examples based on SGNRs and LGNRs demonstrate that anisotropic plasmonic nanoparticles can be aligned in LC host fluids so that the polarized plasmonic modes of these nanoparticles have different orientations with respect to each other and the LC director. By varying the aspect ratios, composition (e.g. some particles could be made of silver while others of gold) and geometric shape of individual types of codispersed particles in the composite, one can tune both the locations of SPR peaks and their polarization dependent properties as needed for the design of optical materials.

To conclude, we have demonstrated an approach of pre-designed control of optical properties of plasmonic mesostructured nanoparticle based composites, which involves alignment of polarized SPR modes of nanoparticles with different shapes and compositions codispersed within an ordered LC host. Our findings open new possibilities for engineering physical behavior of self-assembled

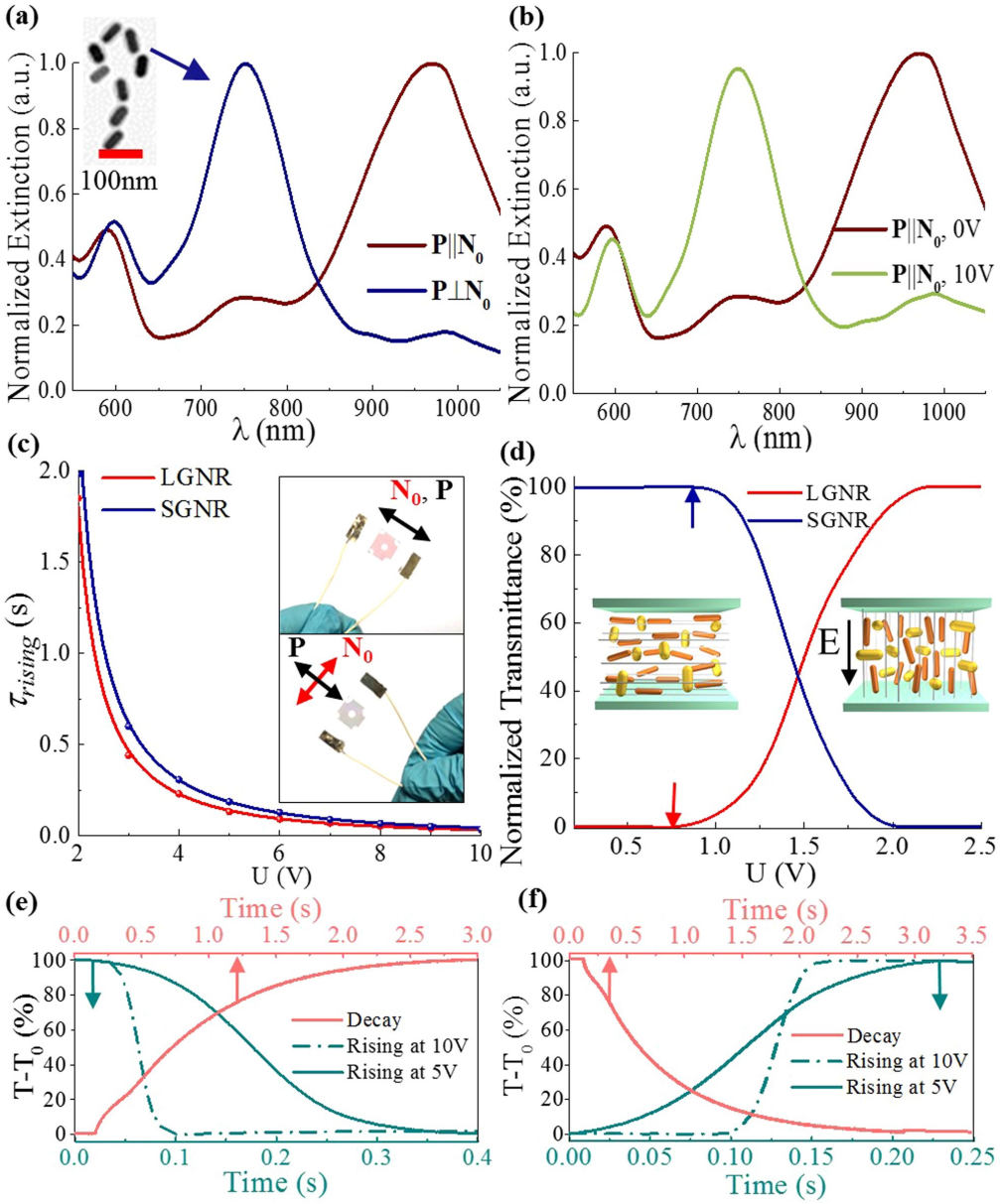

Fig. 2.3: Codispersion, coalignment and switching of differently anchored GNRs in a nematic LC. (a) Normalized extinction of a codispersion of LGNRs treated for tangential and SGNRs treated for perpendicular anchoring for $\mathbf{P}\|\mathbf{N_0}$. The inset is a TEM image of the silica-coated SGNRs. (b) Switching of the extinction spectra at $\mathbf{P}\|\mathbf{N_0}$ by applying $U = 10$ V. (c) Voltage-dependent rising times for both types of GNRs codispersed in the same LC sample, along with photographs of the cell (30 μm-thick, square-inch area filled with the codispersion) in the inset showing the change of color upon changing polarizer orientation from $\mathbf{P}\|\mathbf{N_0}$ (top) to $\mathbf{P}\perp\mathbf{N_0}$ (bottom). (d) Voltage dependence of light transmission at the longitudinal wavelengths of SGNRs and LGNRs, with the threshold voltages marked by colored arrows. The insets are schematics of the cell before and after applying U much larger than U_{th}, along with schematically shown alignment of particles in the LC with and without applied U. (e, f) Rising and decay times for (e) SGNRs and (f) LGNRs measured based on relative changes of transmittance $T - T_0$ for the same LC codispersion by using optical band-pass filters corresponding to their longitudinal SPRs.

optical metamaterials, as well as technological uses in plasmonic nanolasers, guest-host LC displays and smart windows, [2] electrically switchable broadband polarizing elements and tunable optical filters.

2.4 References

[1] Q. Liu, Y. Cui, D. Gardner, X. Li, S. He, and I. I. Smalyukh. "Self-alignment of plasmonic gold nanorods in reconfigurable anisotropic fluids for tunable bulk metamaterial applications," *Nano Lett.*, 2010 **10** 1347.

[2] Q. Liu, Y. Yuan, I. I. Smalyukh, "Electrically and optically tunable plasmotic guest-host liquid crystals with long-range ordered nanoparticles," *Nano Lett.*, 2014 **14** 4071.

[3] Y. Zhang, Q. Liu, H. Mundoor, Y. Yuan, I. I. Smalyukh, "Metal nanoparticle dispersion, alignment and assembly in nematic liquid crystals for applications in switchable plasmonic color filters and E-polarizers," *ACS Nano*, 2015 **9** 3097.

[4] Y. Yuan, I. I. Smalyukh, "Topological nanocolloids with facile electric switching of plasmonic properties," *Opt. Lett.*, 2015 **40** 5630.

[5] B. Senyuk, D. Glugla, I. I. Smalyukh, "Rotational and translational diffusion of anisotropic gold nanoparticles in liquid crystals controlled by varying surface anchoring," *Phys. Rev. E*, 2013 **88** 062507.

[6] S. Link, Z. L. Wang, M. A. El-Sayed, "Alloy Formation of GoldSilver Nanoparticles and the Dependence of the Plasmon Absorption on Their Composition," *J. Phys. Chem. B*, 1999 **103** 3529.

[7] H. K. Bisoy, S. Kumar, "Liquid-crystal nanoscience: an emerging avenue of soft self-assembly," *Chem. Soc. Rev.*, 2011 **40** 306.

[8] J. Perez-Juste, L. M. Liz-Marzan, S. Carnie, D. Y. C. Chan, Mulvaney, P. "Electric-Field-Directed Growth of Gold Nanorods in Aqueous Surfactant Solutions," *Adv. Funct. Mater.*, 2004 **14** 571.

[9] X. Ye, L. Jin, H. Caglayan, J. Chen, G. Xing, C. Zheng, V. Doan-Nguyen, Y. Kang, N. Engheta, C. R. Kagan, C. B. Murray, "Improved Size-Tunable Synthesis of Monodisperse Gold Nanorods Through the Use of Aromatic Additives," *ACS Nano*, 2012 **6** 2804.

[10] W. C. Wu, J. B. Tracy, "Large-Scale Silica Overcoating of Gold Nanorods with Tunable Shell Thicknesses," *Chem. Mater*, 2015 **27** 2888.

[11] J. A. Fan, C. Wu, K. Bao, J. Bao, R. Bardhan, N. J. Halas, V. N. Manoharan, P. Nordlander, G. Shvets, F. Capasso, "Self-assembled plasmonic nanoparticle clusters," *Science*, 2010 **328** 1135.

[12] M. R. Jones, R. J. Macfarlane, B. Lee, J. Zhang, K. L. Young, A. J. Senesi, C. A. Mirkin, "DNA-nanoparticle superlattices formed from anisotropic building blocks.", *Nat. Mater*, 2010 **9** 913.

[13] T. Hu, B. P. Isaacof, J. H. Bahng, C. Hao, Y. Zhou, J. Zhu, X. Li, Z. Wang, S. Liu, C. Xu, J. S. Biteen, N. A. Kotov, "Self-Organization of Plasmonic and Excitonic Nanoparticles into Resonant Chiral Supraparticle Assemblies." *Nano Lett.*, 2014 **14** 6799.

Chapter 3

Electric switching of visible and infrared transmission using liquid crystals co-doped with plasmonic gold nanorods and dichroic dyes

Adapted from: Optics Express. 2018, **26** 22264-22272.

Chapter overview

Smart windows and many other applications require synchronous or alternating facile electric switching of transmitted light intensity in visible and near infrared spectral ranges, but most electrochromic devices suffer from slow, nonuniform switching, high power consumption and limited options for designing spectral characteristics. Here we develop a guest-host mesostructured composite with rod-like dye molecules and plasmonic nanorods spontaneously aligned either parallel or orthogonally to the director of the liquid crystal host. This composite material enables fast, low-voltage electric switching of electromagnetic radiation in visible and infrared ranges, which can be customized depending on the needs of applications, like climate-dependent optimal solar gain control in smart windows.

3.1 Introduction

LC devices, such as optical modulators, displays and shutters, often utilize dichroic dye guest molecules to control visible light intensity. [1,2,4,50] Typically, dichroic dyes are rod-like molecules with dimensions comparable to the LC molecules. Thus, they tend to align with the LC director

N (the average orientation of rod-like LC-molecules [5]) and follow **N** as it rotates in response to low-voltage electric fields. Since the absorption of dye molecules depends on their orientation with respect to the light propagation direction and the polarization direction, if this light is linearly polarized, [1] switching the LC director allows for tuning the relative fractions of light absorbed by the dye molecules and transmitted through the LC cell. Plasmonic analogs of these guest-host LCs, introduced recently,[6–9] extend this principle to rod-like plasmonic nanoparticles with typical dimensions in the range of tens of nanometers. Dichroic dyes [1, 2, 4, 50] and plasmonic nanoparticles, such as gold nanorods (GNRs), [6–9] have their advantages and disadvantages when used with LCs and were previously utilized only separately in recent studies or applications. For example, a large variety of inexpensive commercially available dyes and their (often high) solubility concentration limits make them ideal for designing switchable light absorption in the visible spectral range, but not in the infrared. [1] In contrast, plasmonic GNRs with longitudinal surface plasmon resonance (SPR) peaks in the infrared range allow for tuning peak absorption within the near infrared but rarely in the short-wavelength part of the visible spectrum. [6–9] Co-dispersions of plasmonic GNRs were developed recently [9] to demonstrate that short-range or broadband spectral characteristics can be obtained in the switchable plasmonic guest-host composites by mixing nanorods with different aspect ratios and surface treatments within the LC dispersions, though this again was limited in terms of the accessible spectral range.

In this work, we develop a mesostructured LC composite with both molecular dichroic dyes and plasmonic nanoparticles homogeneously distributed within the host medium. We demonstrate that long axes of dye molecules and GNRs can be spontaneously aligned parallel to **N**, as well as that the rod-like nanoparticles can be also oriented orthogonally to **N** by defining perpendicular boundary conditions (BCs) on their surfaces. This allows tuning the transmitted light intensity in both the visible and the near infrared spectral ranges, either in-phase or out-of-phase. Using different sample geometries, nematic and cholesteric LCs with negative or positive dielectric anisotropy, we show that the LC composites switching times can be varied from millisecond to seconds and

transmission of both unpolarized and polarized light can be controlled depending on the needs of applications such as smart windows, optical shutters, modulators, etc.

3.2 Method and design

GNRs were synthesized following a seed mediated method while using surfactants and pH control to tune their aspect ratio. [9,12] To obtain the longitudinal localized SPR peaks at 780 nm, 815 nm and 1010 nm, the synthesized GNRs were designed to have mean lengths and diameters of 77×21 nm, 93×23 nm, and 104×20 nm, respectively, as determined by transmission electron microscopy (TEM) (Fig. 3.1(a-c)). GNRs with the longitudinal SPR peak at 815 nm were surface-functionalized with thiol-terminated methoxy-poly(ethylene glycol) (mPEG-SH 5kDa, JemKem Technology). [10] For some GNRs, porous silica shells were grown around the nanoparticles (Fig. 3.1(a,b)), followed by further surface-functionalization with dimethyloctadecyl[3-(trimethoxysilyl) propyl] ammonium chloride (DMOAP, ACROS Organics) according to procedures described elsewhere. [8–10] The thickness of the silica shell was controlled to maintain the anisotropic shape of the ensuing nanostructures, as needed for orienting these particles in LCs. The extinction spectra of both silica and PEG capped GNRs in isotropic solvents are shown in (Fig. 1(d,e)). To disperse different types of synthesized GNRs in various LCs, we used nematic 4-cyano- 4-pentylbiphenyl (5CB, Chengzhi Yonghua Display Materials Co., Ltd.) as an intermediate nematic solvent. First, 60 μl of GNRs dispersion in methanol $\sim$ 0.91 nmol/l was kept in a 0.5 ml centrifuge tube at 90 $^{\circ}C$ for an hour to fully evaporate the solvent. Then 15 l of 5CB was added and kept under sonication for 5 min at 40 $^{\circ}C$ while in the isotropic phase and then vigorously stirred until it cooled down to the nematic phase. The sample was centrifuged at 2000 rpm for 3 min to remove occasional aggregates caused by the nucleation of nematic domains during the phase transition, [13] yielding a stable dispersion 0.68 nmol/l of GNRs within 5CB. To obtain dispersions with negative dielectric anisotropy $\Delta\varepsilon$, these 5CB dispersions of GNRs were mixed with a nematic mixture AMLC-0010 (from AlphaMicron Inc.) with $\Delta\varepsilon = -3.7$ and containing dichroic dyes with strong absorption within the visible spectrum. The mixing of 5CB and AMLC-0010 by a ratio of 1:10 (vol. %)

yielded a mixture with an estimated $\Delta\varepsilon \approx -2$. The cholesteric pitch p of LC mixtures was maintained within $p = 10-60$ μm using a left-handed chiral dopant ZLI-811 (from Merck) and measured with the Grandjean-Cano wedge cell method. [14] Alternatively, the dispersion of DMOAP capped silica on GNRs (DMOAP-SiO_2-GNRs) in 5CB was mixed with the AMLC-0010 at ratio 1:1 (vol. %) yielding a nematic mixture with $\Delta\varepsilon \approx 4.6$.

We used different configurations of cells with homeotropic (perpendicular) and planar BCs for the LC far-field director $\mathbf{N_0}$. In the former case, polyimide SE1211 (Nissan Chemical Industries, Ltd.) was spin-coated onto the glass plates with transparent indium tin oxide (ITO) electrodes at 3000 rpm for 60 s and baked at 180 °C for 60 min. In the latter case, a thin layer of 1% aqueous polyvinyl alcohol (PVA, Sigma-Aldrich) was spin-coated and kept in an oven at 100 6ircC for 1h and then unidirectionally rubbed. The cells were assembled using 30 μm silica spacers and glued with UV-curable NOA-63 glue (Norland Products, Inc.) and the cell gap thickness was checked using an optical interference method. We used an Olympus BX-51 polarizing optical microscope (POM) equipped with 10×, 20×, and 50× objectives with numerical aperture 0.3-0.9 along with a CCD camera (GS3-U3-28S5C, from Point Grey Research). Extinction and transmittance spectra were probed using a microscope-mounted spectrometer USB2000-FLG (Ocean Optics) with a broadband (400-1200 nm) polarizer inserted into the optical path after the sample using a natural light lamp. Electric switching properties, including the threshold voltage and response time, etc., were measured utilizing a photodiode and data acquisition card SCC-68 (National Instruments Co.) controlled by a homemade software [6] written in Labview and a Si amplified photodetector PDA100A (Thorlabs Inc.). The response times, including both the rising time upon applying the voltage and the decay time after removing the voltage, were measured as in our previous studies and described elsewhere. [6–10] Wavelength-selective studies of switching of dye and GNR orientations utilized optical interference filters such as 700 nm long pass filter (Semrock Inc.) and an infrared filter (Olympus). TEM images were obtained using FEI Tecnai T12 Spirit.

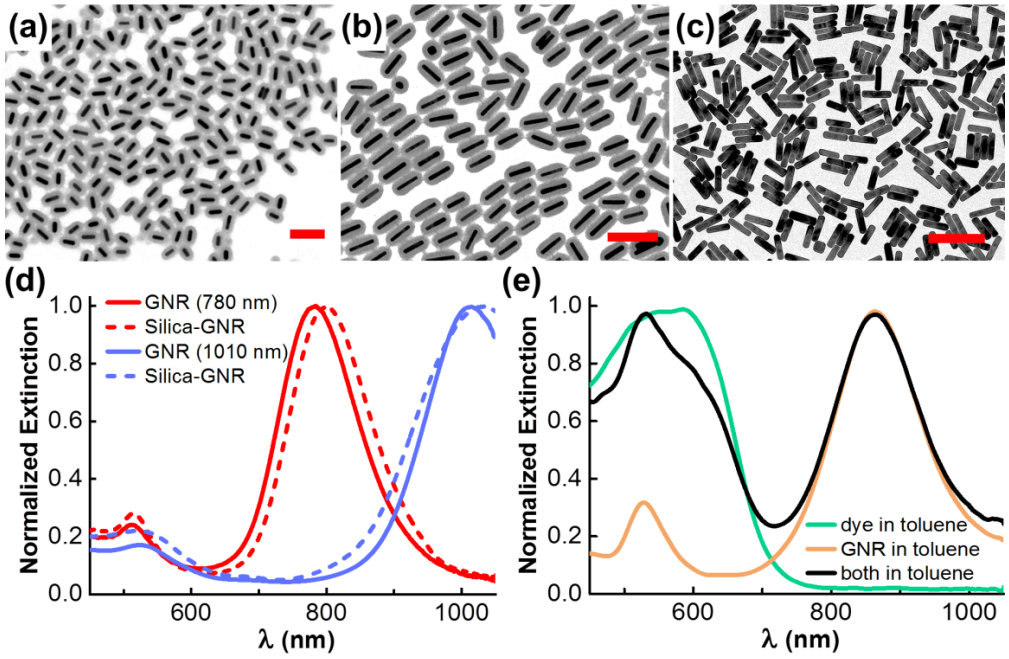

Fig. 3.1: TEM imaging of GNRs and extinction spectra of dye molecules and nanoparticles in isotropic solvents. (a-c) TEM images of GNRs with different longitudinal SPR peaks: (a) 780 nm, (b) 1010 nm and (c) 815 nm GNRs shown in (a) and (b) are coated with a silica shell of average thickness of 21 nm and 25 nm, respectively. Scale bars are 200 nm. (d) Normalized by the maximum intensity extinction spectra of GNRs in water before (red and violet lines) and after silica capping (corresponding lines). (e) Normalized by the maximum intensity extinction spectra of dye molecules and PEG-capped GNRs in toluene taken separately (green and orange lines) and when dispersed jointly (black line). Note that the extinction peaks of dye and the longitudinal SPR of GNRs are red-shifted due to the high refractive index of toluene.

3.3 Experiment and Characterization

GNRs treated with PEG promoted tangential BCs on their surfaces, prompting self-alignment of GNRs within the aligned LC parallel to **N** (Fig. 3.2(a)), while DMOAP-SiO_2-GNRs self-aligned perpendicularly to **N** because of perpendicular BCs (Fig. 3.2(b)). This self-alignment (Fig. 3.2(a, b)) is driven by the minimization of the surface anchoring energy. [6, 7] The corresponding polarization-dependent extinction spectra of PEG-GNR and DMOAP-SiO_2-GNRs in uniformly aligned 5CB samples are shown in Fig. 3.2(c, d). The rod-like dichroic dyes follow the LC molecules and **N** because of the induced dipole-dipole (anisotropic van der Waals) interactions, [1] similar to that between LC molecules themselves. [5,14] Although the mechanisms of alignment

of nanometer-sized rod-like dichroic dye molecules and much larger (20 to 100nm) nanorods are rather different, the orientational self-ordering of both leads to anisotropic, polarization-dependent optical characteristics (Fig. 3.2(c,d)). Orientational self-ordering of different types of GNRs and dye molecules can be quantified by determining the scalar order parameter commonly defined as S_{GNR} see equation (2.1), where the angled brackets denote sample average values and θ is the angle between the long axes of rod-like dye molecules or nanoparticles and $\mathbf{N}$. [14] By using samples with the uniformly aligned $\mathbf{N_0}$ defined by the rubbing direction $\mathbf{N}(r)$ in planar LC cells, the order parameter S (see equation (2.2)) of both the dichroic dye and GNRs can be experimentally determined based on the peak absorbance values $A_{\parallel}$ and $A_{\perp}$ at the linear polarization orientation of the probing light $\mathbf{P}\|\mathbf{N_0}$ and $\mathbf{N}\perp\mathbf{N_0}$, respectively. [1, 14] The PEG-GNRs and DMOAP-SiO_2-GNRs (Fig. 3.2(c,d)) exhibit order parameter values of 0.66 and -0.41, respectively, consistent with their average alignment parallel and perpendicular to $\mathbf{N_0}$. In a similar way (Fig. 3.2(c)), we determine an order parameter of ≈ 0.61 for the dye.

Dye molecules and GNRs align with respect to the local director also in samples with spatially varying $\mathbf{N}$, such as the uniformly π-twisted configuration shown in (Fig. 3.2(e)). In this sample, the dichroic dye molecules and PEG-functionalized GNRs follow the helicoidal $\mathbf{N}$ in the LC with $\Delta\varepsilon < 0$ and $p = 60$ m in a planar cell of thickness $d \approx p/2 \approx 30$ m. Following $\mathbf{N}$, dye molecules and GNRs twist by π around the helical axis perpendicular to cell substrates. This structure of spatial orientations of dye molecules and nanoparticles is inferred from the extinction spectra of the composite LC (Fig. 3.2(f)).

Due to a large pitch, linear polarizations of visible and near-infrared electromagnetic radiation traversing such LC cell closely follow the rotation of $\mathbf{N}$ as the Mauguin parameter [14] $np/(2\lambda) \gg 1$, where an optical anisotropy of used mixtures was within $\Delta n \approx 0.05$-0.2 and is a wavelength of light. This results in a strong dependence of the extinction spectra on the polarization of the probing light $\mathbf{P}$ (Fig. 3.2(f)) with a maximum extinction due to the dye and the longitudinal SPR of PEG-functionalized GNRs at $\mathbf{P}\|\mathbf{N}(r)$. Under the Mauguin regime of light propagation, the strong

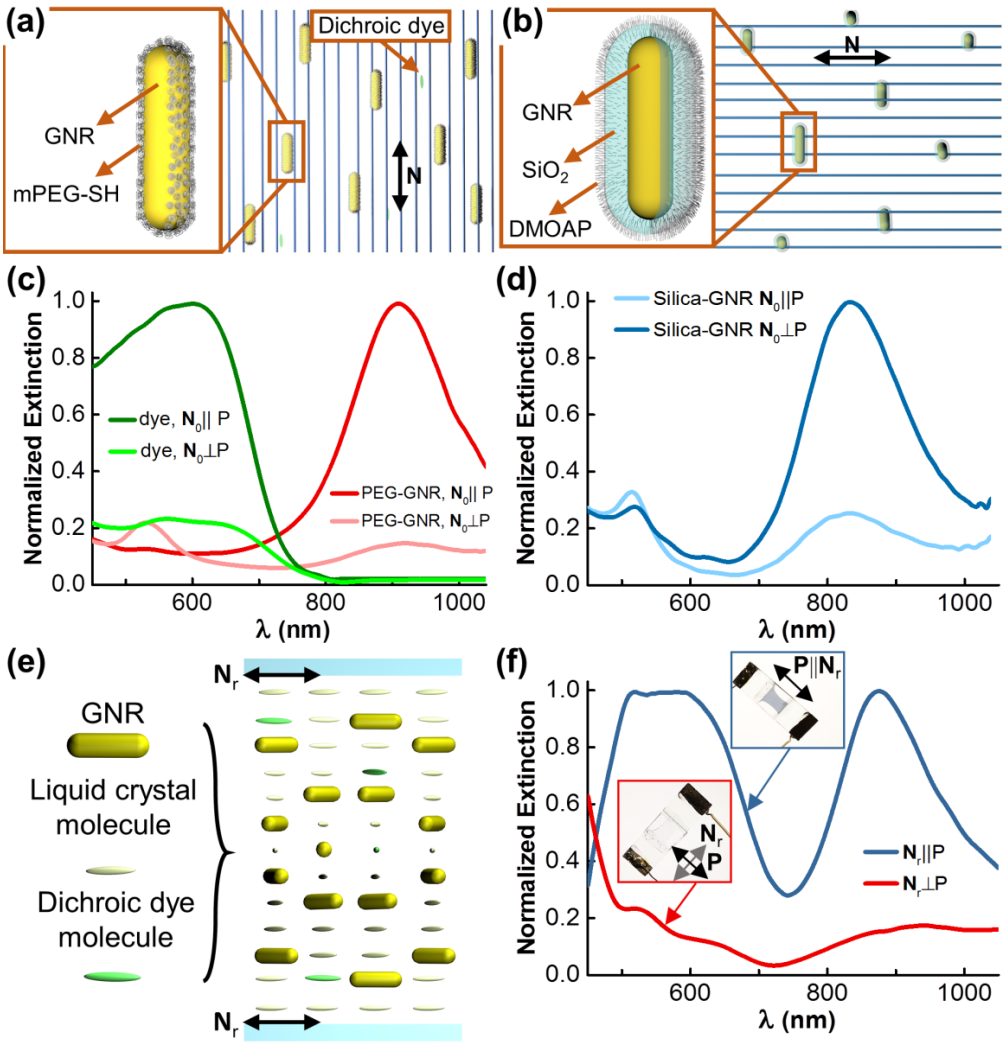

Fig. 3.2: Unidirectionally aligned and twisted structures of LC doped with GNRs and dichroic dye molecules. (a) Schematic of GNRs capped with mPEG-SH following $\mathbf{N}$ (blue lines) in a uniformly aligned LC; the inset shows details of surface functionalization of GNRs. (b) Schematic diagram of DMOAP-SiO_2-GNRs that exhibit self-alignment perpendicular to $\mathbf{N}$; the inset shows details of silica shells around GNRs and DMOAP surface functionalization. (c, d) Normalized by the maximum intensity extinction spectra of LC with (c) PEG-functionalized and (d) DMOAP-SiO_2-GNRs in a planar cell for linear polarizations of probing light $\mathbf{P}\|\mathbf{N_0}$ and $\mathbf{P}\perp\mathbf{N_0}$. (e) Schematic diagram of the cholesteric LC co-doped with dichroic dye and PEG-functionalized GNRs in a planar cell with the alignment of $\mathbf{N}$ at cell substrates defined by the rubbing direction $\mathbf{N}(r)$. (f) Normalized spectra of cholesteric LC with $\Delta\varepsilon < 0$ (1:10 mixture of 5CB and AMLC-0010) co-doped with the dichroic dye and PEG-functionalized GNRs in a planar cell shown in (e); the spectra are obtained for $\mathbf{N}\|\mathbf{N}(r)$ and $\mathbf{N}\perp\mathbf{N}(r)$.

polarization dependence of the spectra shown in (Fig. 3.2(f)) confirms that the dye molecules and the rod-like particles mimic the spatial LC director configurations, as depicted in Fig. 3.2(e).

A cholesteric LC composite with $\Delta\varepsilon < 0$, the same as shown in Fig. 3.2(f), was also introduced into a homeotropic cell with $d \approx p/2 \approx 30$ μm. Despite the cholesteric LCs tendency to twist, strong perpendicular BCs at the substrates of this cell cause unwinding of **N** (a left-side inset in Fig. 3.3(a)). Application of 1 kHz AC voltage to the transparent ITO electrodes at confining substrates forces LC molecules to rotate to be orthogonal to the electric field and tangential to cell substrates. This realignment is due to the dielectric coupling between **N** and electric field and leads to the so-called translationally invariant twisted configuration[15] (a right-side inset in Fig. 3.3(b)) with the threshold voltage[16]

$$U_{\rm th}^2 = \frac{\pi^2}{|\Delta\varepsilon|}\left(K_{33} - \frac{K_{22}^2 d^2 q_0^2}{K_{33}\pi^2}\right), \tag{3.1}$$

where K_{22} and K_{33} are the twist and bend Frank elastic constants, respectively, and $q_0 = 2\pi/p$. The chiral nature of the used cholesteric LC tends to reduce $U_{\rm th}$ of the Freedericksz transition as compared to the nematic counterpart (for which $q_0 = 0$), so that it is in the range of several volts despite the small value of $\Delta\varepsilon$; the experimentally measured value of $U_{\rm th} \approx 5$ V (Fig. 3.3(a)) is consistent with that estimated with above expression for material parameters of used LC. The extinction spectra (Fig. 3(b)) exhibit strong dependence on the applied voltage $U > U_{\rm th}$, revealing that both GNRs and dye molecules (Fig. 3.3(a,c)) in this composite follow changes of the LC orientation with applied U. Interestingly, the PEG-GNR transmission decay faster than the dyes (Fig. 3.3(c)).

To characterize the kinetics of switching of our LC composite (Fig. 3.3(d)), we separately probed response times of the dichroic dye and GNRs using optical filters. Rising and decay times were calculated based on the relative light transmittance changes (Fig. 3.3(e,f)) between 90% and 10%, respectively. The rising rising and decay decay response times of switching **N** are related as

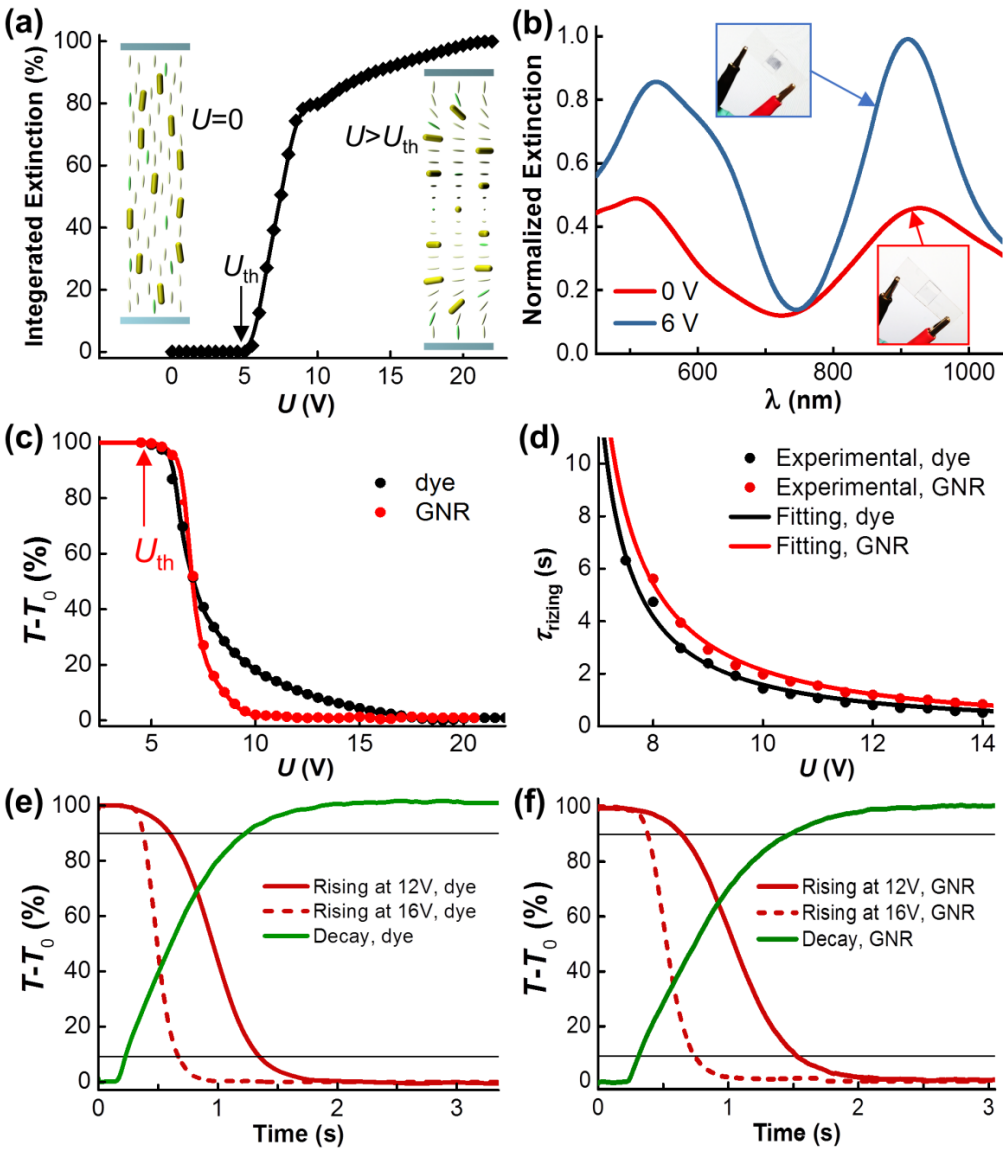

Fig. 3.3: Electric switching of a cholesteric LC co-doped with GNRs and dichroic dyes in a homeotropic cell. (a) Integrated extinction of light traversing through a homeotropic cholesteric LC cell versus U. The threshold voltage $U_{\rm th}$ is marked by an arrow; cell thickness is $d \approx p/2$ with $p \approx 60$ μm. Schematics in the insets show patterns of orientation of dichroic dye and LC molecules and GNRs within the LC at (left) $U < U_{\rm th}$ and (right) $U > U_{\rm th}$. (b) Normalized by the maximum intensity extinction spectra of the homeotropic cell for linear polarizations with and without field, with insets of photographs of inch-size cells. (c) Voltage dependence of the transmittance of natural white light across the homeotropic cell measured separately utilizing optical filters for both PEG-GNR and the dichroic dye. (d) Voltage-dependent rising times for both dye and GNR in the same sample. (e, f) Rising and decay times for dye and PEG-GNR, respectively, measured based on changes of a relative transmittance $(T - T_0)$, where T_0 is the minimum transmittance of the composite, for the same LC system by using corresponding optical filters.

in equation 2.3.

for pristine LCs. [14] Mechanical coupling of GNRs and N through the surface anchoring and direct van der Waals interactions between dye and LC molecules previously led to similar relations in guest-host dichroic [1,2,4,50] and plasmonic [6–10] LCs. This is also the case for our guest-host LCs that contain plasmonic GNRs and dichroic dye molecules at the same time (Fig. 3.3(d)). Reorientation of dichroic dye and **N** is faster than that of PEG-functionalized GNRs, which is expected given that the dye molecules are comparable in dimensions to that of LC molecules while GNRs are much larger and exhibit lagging of rotational response, as also observed previously. [9] The average decay values for dichroic dye and PEG-functionalized GNRs are 1.33 s and 1.38 s, respectively, relatively long because of the large cell thickness $d \approx 30$ μm, whereas rising approach milliseconds range at $U > 10$ V (Fig. 3.3(d, f)). These response times can be shortened further by orders of magnitude through reducing d due to the scaling $\tau_{\text{decay}} \propto d^2$, similar to that of pristine LCs. [6]

We also designed the nematic LC composite with $\Delta\varepsilon > 0$ doped with dichroic dye and DMOAP-SiO_2-GNRs (Fig. 3.4). DMOAP imposes homeotropic alignment of LC molecules on the surface of GNR nanostructures, resulting in a novel configuration where GNRs orient in the plane perpendicular to **N** and are able to freely rotate around **N**. In a planar cell at $U > U_{\text{th}}$, **N** reorients to align with the applied field, which is followed by reorientation of GNRs and dye molecules that tend to stay perpendicular and parallel to **N**, respectively (Fig. 3.4(a)). Extinction spectra of this composite demonstrate strong polarization and U dependence (Fig. 3.4(b)), allowing for the effective switching between the visible or near infrared absorbance bands in an alternating manner. U_{th} measured separately with the appropriate optical filter based on the responses of GNRs and dye molecules are consistent (Fig. 3.4(c)). Reorientation of GNRs is slower compared to both **N** and dichroic dye molecules reorientation (Fig. 3.4(d)). Characterization of τ_{rising} and τ_{decay} are shown in Fig. 3.4(e,f), respectively. The response times in this composite are faster as compared to its counterpart with the negative dielectric anisotropy owing to the larger absolute value of dielectric

anisotropy of the LC host. Further exploration of cell configurations and LC composites with various additives in the forms of organic and inorganic materials may allow pre-designed switching of electromagnetic radiation in visible and infrared ranges, depending on the needs of applications.

3.4 Conclusion

To conclude, we designed and implemented mesostructured guest-host LC composites based on co-doping nematics and cholesterics with dichroic dyes and shape-anisotropic plasmonic nanoparticles. Our findings demonstrate that nematic and cholesteric LC hosts with positive or negative dielectric anisotropies and different sample geometries can be used to design guest-host composite systems capable of synchronous (Fig. 3.3(b)) or alternating (Fig. 3.4(b)) switching of light transmission in visible and infrared spectral ranges. Relatively short (≤ 1 s) response times of our guest-host composites are superior as compared to typical responses of solid-state electrochromic devices like the ones utilized in smart windows. [17, 18] The response time can be reduced further down to hundreds or even tens of milliseconds by varying gap thickness of the used cells because the LCs are known to respond much faster in thinner cells, as studied before for positive dielectric LCs. [6] Our guest-host mesostructured composites are advantageous compared with other different LC-based composites that are already implemented in smart windows applications. For example, polymer dispersed liquid crystals (PDLC) provide operation modes based on switching between scattering and clear states. Moreover, the voltage required to switch PDLC is higher by almost one order of magnitude relative to our system, although the response time is faster compared to our system. [20, 21] The thermochromic LC systems are driven by higher voltages as well and suffer from nonuniform switching. [19] The dichroic dyes-based conventional guest-host LC displays which show similar response time as our system mainly function in the visible region of the light spectrum, not extending to cover the infrared region of the spectrum. [22] In contrast, we can selectively tune the IR absorbance peak through changing the aspect ratio of the inserted GNRs in these composites to modulate the radiation in many near infrared regions. Although our examples (Fig. 3.2(e),(f) and Fig. 3.3) of switching cholesteric LC configurations exhibit polarization-dependent properties,

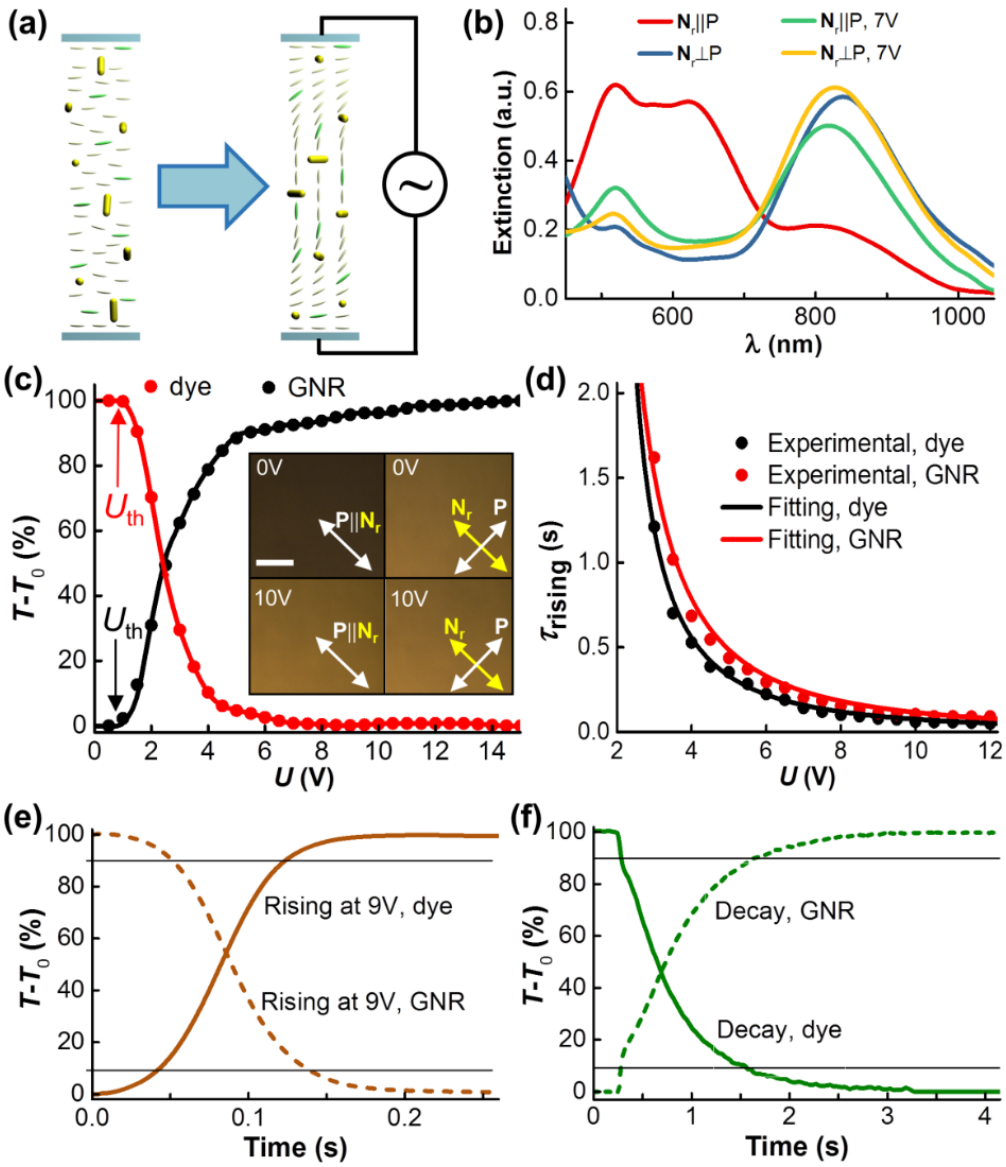

Fig. 3.4: Nematic LC co-doped with dye and DMOAP-SiO_2-GNRs in a planar cell. (a) Schematics of GNRs (yellow rods) and dichroic dye molecules (green ellipsoids) self-aligning with respect to $\mathbf{N}$ at (left) $U < U_{\rm th}$ and (right) $U > U_{\rm th}$. (b) Extinction spectra of the planar cell for polarizations $\mathbf{P}\|\mathbf{N}(r)$ and $\mathbf{P}\perp\mathbf{N}(r)$. Switching between the visible-range and the near infrared extinction bands can be done by rotating the cell 90° with respect to $\mathbf{P}$, or by applying U. (c) Relative change of transmittance versus U in the spectral ranges of absorption of GNRs and dye obtained using natural white light through the planar cell measured separately utilizing the appropriate optical filters. Insets show micrographs of the planar cell upon rotating $\mathbf{P}$ from $\mathbf{P}\|\mathbf{N}(r)$ to $\mathbf{P}\perp\mathbf{N}(r)$ and with applying U; the scale bar is 50 μm. (d) Comparison of U-dependent $\tau_{\rm rising}$ for dye and GNRs within the same sample. (e,f) Characterization of (e) $\tau_{\rm rising}$ and (f) $\tau_{\rm decay}$ for dye and GNRs based on relative changes of transmittance $(T - T_0)$ using optical filters to pre-select the respective absorbance bands. Average values of $\tau_d ecay$ are 1.37 s and 1.41 s, as determined for the dye and GNRs, respectively.

one can also extend this approach of composite guest-host LCs with both nanoparticles and dyes to the regime of polarization-independent responses when the Mauguin parameter is tuned to be small, $\Delta np/(2\lambda) < 1$, which was previously achieved for guest-host LCs utilizing only dichroic dyes. [4] This would be of interest for applications in a new breed of smart windows.

3.5 References

[1] B. Bahadur, "Handbook of Liquid Crystals," *Wiley-VCH*, Weinheim, 2A, 1998.

[2] G. H. Heilmeier, L. A. Zanoni, "Guesthost interactions in nematic liquid crystals. A new electrooptic effect," *Appl. Phys. Lett.*, 1968 **13** 91.

[3] T. Uchida, H. Seki, C. Shishido, M. Wada, "Bright dichroic guesthost LCDs without a polarizer," *Proc. Soc. Inf. Disp.*, 1981 **22** 41.

[4] B. Taheri, T. Kosa, V. Bodnar, L. Sukhomlinova, L. Su, C. Martincic, J. Chonko, E.-Y. Park, "Guest-host liquid crystal devices for adaptive window application," *Proc. SPIE Emerging Liquid Crystal Technologies V*, 2010 **7618**.

[5] P. M. Chaikin, T. C. Lubensky, "Principles of condensed matter physics," *Cambridge University*, 2000.

[6] Q. Liu, Y. Yuan, I. I. Smalyukh, "Electrically and optically tunable plasmotic guest-host liquid crystals with long-range ordered nanoparticles," *Nano Lett.*, 2014 **14** 4071.

[7] Q. Liu, Y. Cui, D. Gardner, X. Li, S. He, and I. I. Smalyukh. "Self-alignment of plasmonic gold nanorods in reconfigurable anisotropic fluids for tunable bulk metamaterial applications," *Nano Lett.*, 2010 **10** 1347.

[8] L. Jiang, H. Mundoor, Q. Liu, I. I. Smalyukh, "Electric Switching of Fluorescence Decay in GoldSilicaDye Nematic Nanocolloids Mediated by Surface Plasmons," *ACS Nano*, 2016 **10** 7064.

[9] Y. Zhang, Q. Liu, H. Mundoor, Y. Yuan, I. I. Smalyukh, "Metal nanoparticle dispersion, alignment and assembly in nematic liquid crystals for applications in switchable plasmonic color filters and E-polarizers," *ACS Nano*, 2015 **9** 3097.

[10] G. H. Sheetah, Q. Liu, I. I. Smalyukh, "Self-assembly of Predesigned Optical Materials in Nematic Codispersions of Plasmonic Nanorods," *Optics Letters*, 2016 **41** 4899.

[11] X. Ye, C. Zheng, J. Chen, Y. Gao, C. B. Murray, "Using binary surfactant mixtures to simultaneously improve the dimensional tunability and monodispersity in the seeded growth of gold nanorods," *Nano Lett.*, 2013 **13** 765.

[12] B. Nikoobakht, M. A. El-Sayed, "Preparation and growth mechanism of gold nanorods (NRs) using seed-mediated growth method," *Chem. Mater*, 2003 **15** 1957.

[13] D. F. Gardner, J. S. Evans, I. I. Smalyukh, "Towards reconfigurable optical metamaterials: Colloidal nanoparticle self-assembly and self-alignment in liquid crystals," *Mol. Cryst. Liq. Cryst.*, 2011 **545** 1227.

[14] L. M. Blinov, V. G. Chigrinov, " "Electrooptic effects in liquid crystal materials," *Springer-Verlag, New York*, 1996.

[15] I. I. Smalyukh, B. I. Senyuk, P. Palffy-Muhoray, O. D. Lavrentovich, H. Huang, E. C. Gartland, Jr., V. H. Bodnar, T. Kosa, B. Taheri, "Electric-field-induced nematic-cholesteric transition and three-dimensional director structures in homeotropic cells," *Phys. Rev. E*, 2005 **72** 061707.

[16] K. A. Crandall, M. R. Fisch, R. G. Petschek, C. Rosenblatt, "Vanishing Freedericksz transition threshold voltage in a chiral nematic liquid crystal," *Appl. Phys. Lett.*, 1994 **64** 1741.

[17] R. Baetens, B. P. Jelle, A. Gustavsen, "Properties, requirements and possibilities of smart windows for dynamic daylight and solar energy control in buildings: A state-of-the-art review," *Sol. Energy Mater. Sol. Cells*, 2010 **94** 87.

[18] E. L. Runnerstrom, A.Llordés, S. D. Lounis, D. J. Milliron, "Nanostructured electrochromic smart windows: traditional materials and NIR-selective plasmonic nanocrystals," *Chem. Commun.*, 2014 **50** 10555.

[19] I. Sage, "Thermochromic liquid crystals," *Liq. Cryst.*, 2011 **38** 1551.

[20] J. Heo, J.-W. Huh, and T.-H. Yoon, " "Fast-switching initially-transparent liquid crystal light shutter with crossed patterned electrodes," *AIP Adv.*, 2015 **5** 047118.

[21] H. Ren, S.-T. Wu, "Anisotropic liquid crystal gels for switchable polarizers and displays," *Appl. Phys. Lett.*, 2002 **81** 1432.

[22] Y.-C. Hsiao, K.-C. Huang, and W. Lee, "Photo-switchable chiral liquid crystal with optical tristability enabled by a photoresponsive azo-chiral dopant," *Opt. Express*, 2017 **25** 2687.

Chapter 4

Tuning and Switching a Plasmonic Quantum Dot "Sandwich" in a Nematic Line Defect

Adapted from: ACS NANO. 2018, **12** 2580-2590.

Chapter overview

We study the quantum-mechanical effects arising in a single semiconductor core/shell quantum dot controllably sandwiched between two plasmonic nanorods. Control over the position and the " sandwich" confinement structure is achieved by the use of a linear-trap, liquid-crystal line defect and laser tweezers that "push" the sandwich together. This arrangement allows for the study of exciton-plasmon interactions in a single structure, unaltered by ensemble effects or the complexity of dielectric interfaces. We demonstrate the effect of plasmonic confinement on the photon-antibunching behavior of the quantum dot and its luminescence lifetime. The quantum dot behaves as a single emitter when nanorods are far away from the quantum dot but shows possible multiexciton emission and a significantly decreased lifetime when tightly confined in a plasmonic sandwich. These findings demonstrate that liquid crystal defects, combined with laser tweezers, enable a versatile platform to study plasmonic coupling phenomena in a nanoscale laboratory, where all elements can be arranged almost at will.

4.1 Introduction

The properties of nanoparticles, often dramatically different from those of bulk materials despite identical chemical composition, can be further controlled through interactions with other nanoparticles. [3, 62, 63] The exploration of plasmonic phenomena as a means to control the behavior of excitonic systems is a field of active study. [4–15] Such interactions can be used to detect single molecules, [16,17] to drive up- and down-conversion, [18,19] to enhance optical absorption in solar cells, [20–22] to induce hot-electron charge transfer, [23] to drive solar-to-fuel photocatalytic systems,[24] and more. There is a great need for the exploration of plasmon-exciton interactions at the level of individual nanoparticles and nanostructured composites. Traditionally, such measurements are performed on nanoparticles deposited on thin glass substrates using scanning probe technique to move the particles at nanometer level or using a polymer layer to control the spacing between them. [9, 13]

However, such experimental explorations are often made challenging by the sensitivity of these interactions to the proximity of dielectric interfaces, which can cause various artifacts. [7] To mitigate these problems, we recently used laser tweezers and a point defect in the bulk of a liquid crystal (LC) to study the exciton/plasmon coupling of a co-entrapped quantum emitter and a single plasmonic particle. [7] This arrangement allowed for comparison of blinking characteristics of the quantum emitter before and after introducing a plasmonic particle to the LC point defect and showed that the radiative lifetime of the quantum dot (QD) decreased by an order of magnitude, resulting in a reduction of the blinking of the QDs luminescence and a concomitant increase in its radiative efficiency because of the Purcell effect. While this demonstrated the use of LC systems as nanoscale manipulation tools, the enhancement to the local electric field was induced with complex-shaped "nanoburst" gold nanoparticles around which the plasmonic field enhancement was very inhomogeneous. Although this arrangement of nanoburst and quantum emitter turned out to be fortuitous, greater control over the plasmonic field and the placement of the plasmonic particles

and the QD particle is needed.

In this paper, we demonstrate a system in which we use a topological line defect in the LC that traps QDs and well-defined gold nanorods (GNRs) along two dimensions but allows for controlled movement along one dimension (along the defect line) (Fig. 4.1). The GNRs can be moved along the defect line by using infrared laser tweezers and can be manipulated to form a linear "sandwich" structure, where the QD is localized between the tips of two nanorods, so that it resides in a well-defined optical field geometry. In this way, we can study the emission behavior of a single dot, as well as how the emission is influenced when the QD is sandwiched between GNRs inducing a well-defined plasmon-enhanced electromagnetic field. We show that the plasmon coupling induces multiphoton emission and discuss how our findings may have an impact on the ability to design and realize novel mesostructured composite materials with novel physical behavior arising from controlled plasmon-exciton interactions.

4.2 Materials and methods

4.2.1 GNR Synthesis

GNRs used in our experiments were synthesized following the seed-mediated method described in detail elsewhere. [14, 25] To prepare the seed, equal amounts of 5 ml of hexadecyltrimethylammonium bromide (CTAB, Sigma-Aldrich, 0.2M) and gold(III) chloride trihydrate ($HAuCl_4.3H_2O$, Sigma-Aldrich, 0.5 mM) were added to a clean glass bottle followed by 0.6 ml of freshly prepared ice-cold sodium borohydride ($NaBH_4$, Sigma-Aldrich, 10 mM) under vigorous stirring for 2 minutes, and kept at 30 °C for 30 minutes before use, allowing the reaction to complete and $NaBH_4$ to fully decompose. In the meantime, the growth solution was prepared by mixing 25 μl silver nitrate ($AgNO_3$, Sigma-Aldrich, 16 mM) with 10 ml of CTAB (0.2 M), 10 ml of $HAuCl_4$ (1 mM) and 75 μl of L-ascorbic acid (Sigma-Aldrich, 80 mM) under vigorous stirring for 30 seconds. The growth process was initiated by adding 12 μl of seed solution into the growth

solution, and then it was left undisturbed for 8 hours. The GNRs are separated from the solution by centrifugation at 9000 rpm for 30 minutes. These GNRs (Fig. 4.1(d)) were coated with silica shells, which were tuned to be $\sim$ 10 nm thick, and then surface-functionalized with dimethyloctadecyl[3-(trimethoxysilyl)propyl] ammonium chloride (DMOAP, Acros Organics) according to procedures described in our previous study. [27]

4.2.2 LC cell preparation

We used a chiral nematic LCs by using a commercially available nematic mixture E7 (Slichem, China) doped with a chiral dopant Cholesteryl Pelargonate (Sigma-Aldrich). The concentration of the chiral additive in the mixture was adjusted to yield a desired cholesteric pitch $\sim$ 12 μm. [60] LC cells used for the experiments were prepared by assembling two glass plates with a cell gap spacing of $\sim$ 10 μm set using glass fiber segments mixed in a UV-curable glue (Thorlabs). To obtain strong homeotropic boundary conditions for the orientation of the rod-like LC molecules and the director **N** describing their local average orientation, the inner surfaces of the glass plates were treated with DMOAP. Very dilute co-dispersion of GNR and QD in LC were prepared by mixing the nanoparticle dispersions with LC followed by evaporation at 70 °C. The LC mixture was infilitrated into the glass cells using capilary forces and sealed with a fast-setting epoxy.

4.2.3 Experimental setup.

The experimental set up was built around an inverted microscope (IX 81, from Olympus), equipped with lasers, spectrometer and a CCD camera (Flea, PointGrey) for imaging. The microscope is integrated with a holographic optical tweezer operating at 1064 nm output from a fiber laser (IPG photonics). The excitation beam is sent to the microscope with the help of dichroic mirrors (Thorlabs DMSP805R, Semrock FF495-Di03-25 $\times$ 36) (Fig. 4.4(a)) and focused onto the sample using a 100$\times$ oil immersion objective (Olympus, UPlanSApo, NA = 1.42). The emission from the QD particles is collected using the same objective and sent through the optical filters (Chroma HQ 610/75M) and pinhole before being analyzed by a Avalanche Photodiode (APD, from

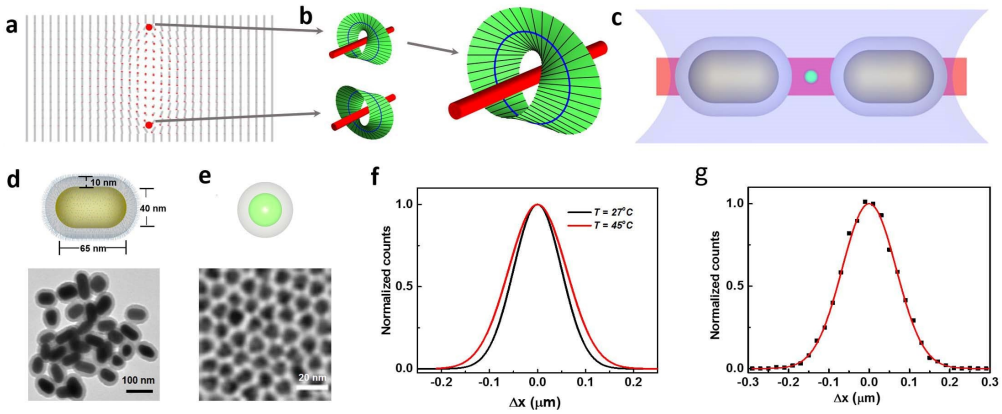

Fig. 4.1: Localization of GNR and QD nanoparticles in linear defect traps. (a) Director configuration in the vertical cross-section of the cholesteric finger with two line defects (marked with the red filled circles), which is translationally invariant along the normal to the cross-section. (b) Configurations of the director field around the defect lines at the top and bottom of the cross-section shown in (a), with details of the director configuration for one of them shown on the right side. The core regions of defects are shown using red color. (c) A schematic illustration of the experimental configuration of QD (green) and GNR (yellow) nanoparticles co-entrapped within the core of a singular line defect (red tube) within a chiral nematic LC. (d) Schematics of the GNR particle with a silica shell and DMOAP surfactant monolayer (top) with dimensions marked on the illustrations and TEM micrograph of the silica capped GNRs (bottom). (e) Schematics of the CdSe/ZnS QD particle representing a core-shell geometry and TEM micrograph of the QD particle (bottom) used in the experiments. (f) The probability distribution of the displacement made by a single GNR within time periods $\Delta t = 0.067$ s, showing the diffusion along the length of the line defect at room temperature and at 45 °C. (g) The probability distribution of the displacement made by a QD in time $\Delta t = 0.067$ s, describing its diffusion along the length of the line defect.

Pico Quant) or Hanbury Brown-Twiss interferometer arrangement for the antibunching analysis. The antibunching measurements were performed using the 473 nm CW output from a diode laser as the excitation source. The fluorescence signal incident on a 50:50 beam splitter is detected by two APDs, placed at the two out ports of the beam, as shown in Fig. 4.4(a). The electrical pulses generated by the APDs are analyzed using time-correlated single photon counting (TCSPC, SPC 130, from Becker and Heckle) hardware, by measuring the second-order cross-correlation between photons detected by the APDs with respect to the photon co-incidence time t. In order to obtain the correlation at the negative coincident time, the signal from one of the APD is delayed by 500 ns by employing delay electronics before being fed to the TCSPC. The fluorescence trajectories of the QD emission was recorded using an APD connected to a data acquisition board (NIDAQ-6363,

National Instruments) and analyzed using a MATLAB code. For fluorescence decay measurements, 467 nm pulsed output from a diode laser (Nano LED- Horiba Scientific, 1MHz, 200 ps) was used as the excitation source. The emission from the QD particles are detected using an APD and analyzed with the help of TCSPC hardware. The fluorescence spectra of a QD particle located in a LC line defect was measured using a spectrometer (SpectraPro-275, Acton Research Corporation) equipped with a grating of 600 g/mm. The detected spectra were recorded using an electron multiplying charge coupled device (EMCCD, iXon3 888, Andor Technology).

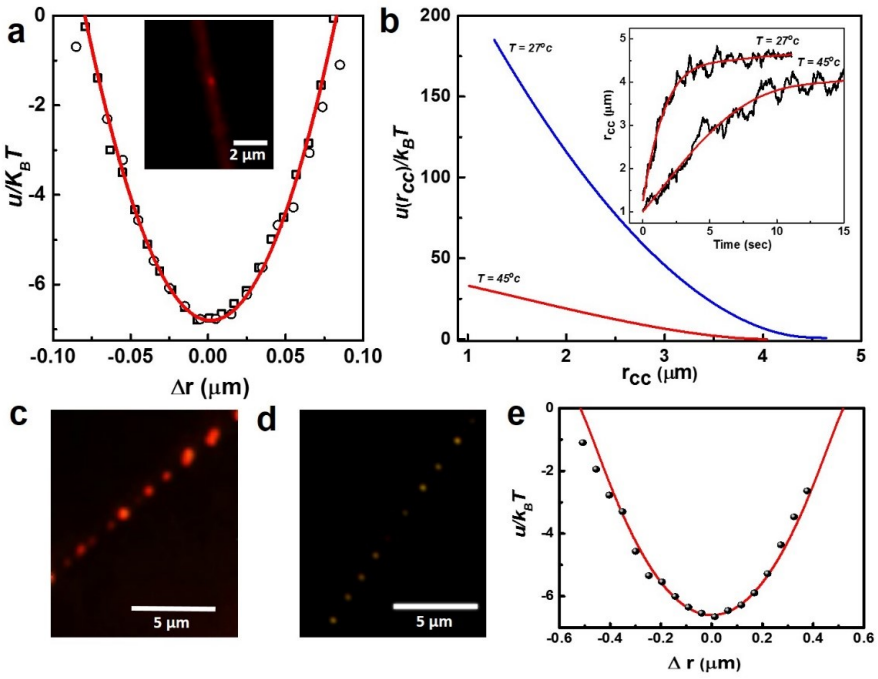

Fig. 4.2: Trapping and interactions of nanoparticles in the cores of defect lines. (a) Trapping potential extracted from the motion of a QD (○) and a GNR (□) in directions perpendicular to the line defect. Inset shows the image of QD particles trapped inside line defect. (b) Interaction potential between two GNR entrapped inside a core of the line defect, probed when they are brought close to each other using optical trapping and then released. The potential is measured at room temperature and at 45 °C. Inset shows the variation of inter-particle center-to-center spacing with time when the optical traps are switched off, demonstrating repulsion between the nanoparticles. (c,d) Assemblies of (c) small clusters of QDs and (d) individual GNRs in a line defect formed due to repulsive interactions and confinement along the defect line. (e) Potential energy of interaction between GNRs extracted from the motion of single particles within an assembly shown in (d).

4.2.4 Numerical modeling

The electromagnetic field enhancement and LSPR peak of GNR in the sandwich assembly was simulated using the nanoDDSCAT$^+$ tool based on the DDA method. [46–49] For the DDA simulations, the structures of GNR and QD are first defined using a 3D computer graphics program, Blender v:2.75 (Fig. 4.3(d)) and rendered to nanoDDSCAT$^+$ to form set of dipoles with refractive index values representing the gold core, silica shell and QD using a DDSCAT conversion tool.[49]

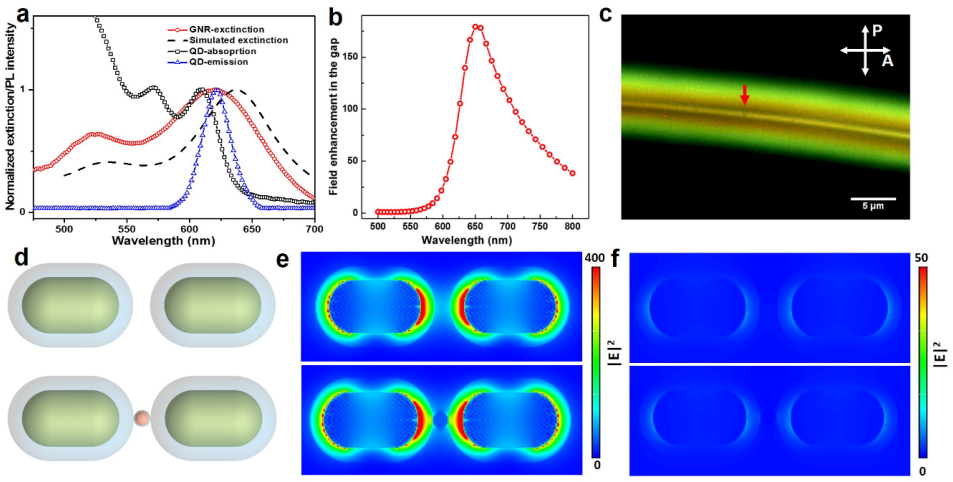

Fig. 4.3: Optical characterization of nanoparticles and modeling of SPR effects involving them. (a) Optical characterization of the nanoparticles used in the experiments showing extinction spectra of GNR (○) particles dispersed in water, simulated extinction spectra of GNRs when they are brought close to each other in the line defect, forming a dimer configuration, indicating a red-shift in the longitudinal LSPR peak. Absorption spectra of the QDs (□) dispersed in toluene and emission spectra of the QDs particles on a glass substrate (Δ). (b) Electric field enhancement at the QD location in the sandwich structure for different emission wavelengths, calculated based on electromagnetic simulations using COMSOL Multiphysics. (c) Optical microscopy image of a LC line defect viewed under crossed-polarizers, indicating strong birefringence of the LC line defect. The location of a GNR- QD sandwich assembly is marked with a red arrow. (d) Schematic of the experimentally realized configuration of the particles showing the dimer configuration of the GNR particles with a QD particle located at the center of the GNR particles. (e,f) Electric field intensity profile for the configuration shown in (d) simulated using DDA method at emission wavelength (e) 620 nm and (f) excitation wavelength 473 nm.

We then calculate the extinction spectra and electric field intensity $|\mathbf{E}|^2$ configuration around the GNRs in the sandwich structure. We have also estimated the electric field enhancement of GNRs in the sandwich structure using COMSOL Multiphysics (Fig. 4.3(b)). The incident un-

polarized electromagnetic wave excites the computational volume, enclosing the GNRs and QD. The simulation is performed in a spherical volume enclosed in a perfectly matched layer shell in the radial directions allowing the calculation of both scattering and absorption contributions. We used refractive index values reported in literature for gold, silica, CdSe, and ZnS. [61–63] The medium refractive index was set equal to the isotropic index of refraction of LC [64] representing the melted core of line defect. The simulations were performed for different interparticle separation between GNRs calculating the LSPR peak position and maximum field enhancement wavelength (see Appendix A, Fig. A.3).

4.3 Elastic trapping of nanoparticles in LC line defect

We used 40×65 nm GNRs (Fig. 4.1), which were synthesized by following the seed-mediated method described in detail elsewhere, [14, 25, 27] see above. We also utilized commercially available CdSe/ZnS core-shell QDs (Ocean nanotech) shown in Fig. 4.1(e), which were selected for their emission peak at 620 nm. These QDs are characterized by an average diameter of 10 nm with a CdSe core and a thin outer shell of ZnS forming a core-shell type structure. The design of our experiments was aimed to control the optical coupling between QDs and GNRs. For this reason, we chose to use GNRs that exhibit a longitudinal surface plasmon resonance (SPR) peak at about 620 nm, matching the emission peak of QD particles (as measured when deposited on a glass substrate). The 10 nm silica shells of GNRs effectively make their SPR properties insensitive to the LCs dielectric and order parameter tensor structures around nanoparticles within the surrounding host medium. As designed, our estimates show that, because of the shells, variations of the director structure within the LC do not cause shifts of the SPR peaks for more than 3 nm. The core-shell QD particles also provide a high quantum efficiency while remaining chemically stable under different experimental conditions used in our work. Very dilute colloidal co-dispersions of GNR and QD nanoparticles (with number densities of each estimated to be 0.01 μm^{-3} or even smaller) were obtained through a series of solvent exchanges in a chiral nematic LC with cholesteric pitch $\sim 12 \sim \mu$m, and infiltrated into a glass cell with a gap of ~ 10 μm, as described elsewhere [7]

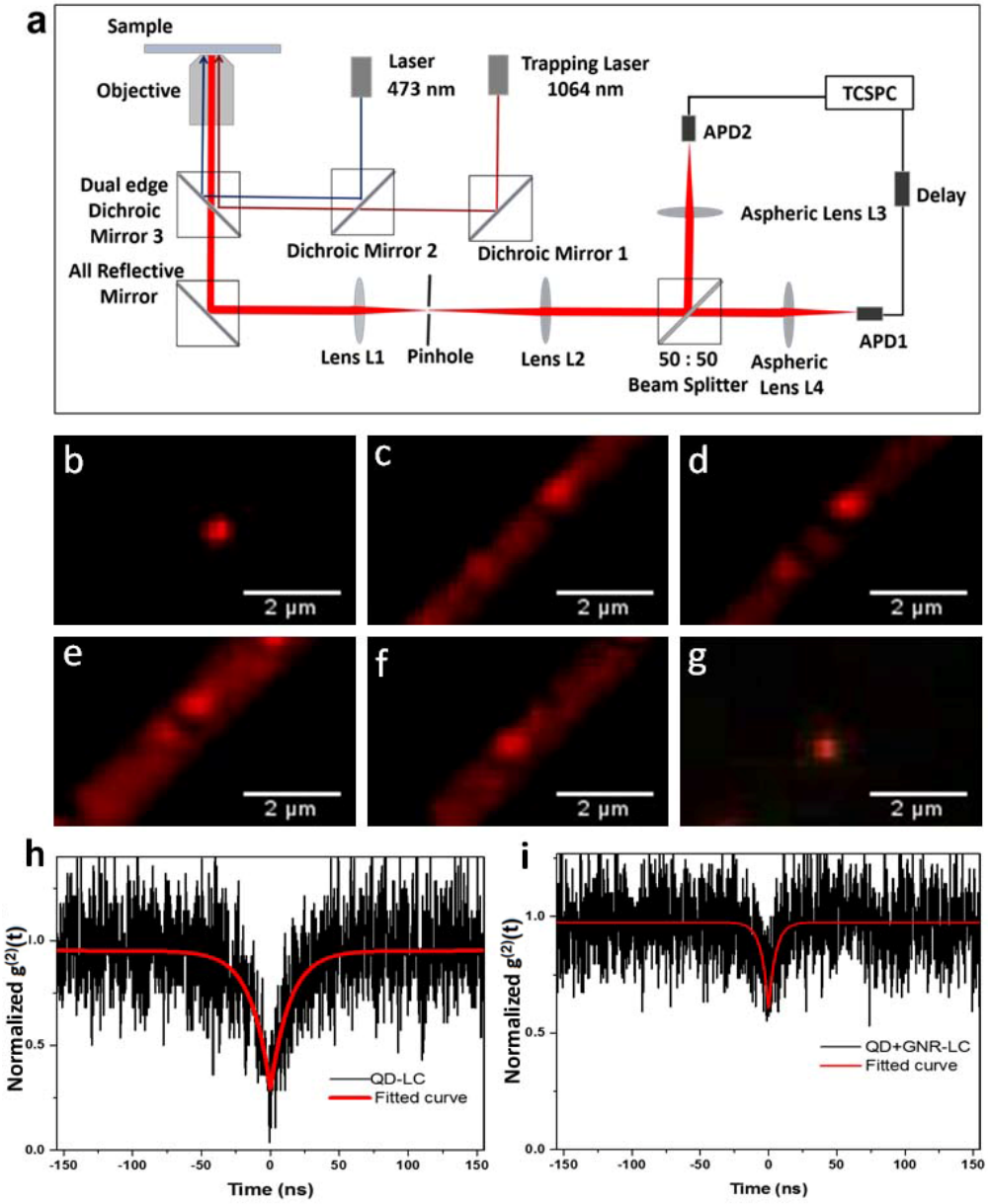

Fig. 4.4: Antibunching setup and characterization. (a) Schematic representation of the antibunching setup used in experiment (b) Fluorescence image of a QD particle trapped inside a LC line defect before moving the GNR close to it. (c-f) Dark field microscopy images viewed with a red filter, showing the nanorod assembly using an optical tweezer, sandwiching a QD particle between. The final sandwich structure is represented in (f). (g) Fluorescence image of a QD particle after forming the sandwich structure. (h,i) Antibunching data collected from the QD particle before (h) and after (i) moving the GNR close to the QD, forming a sandwich assembly.

(See materials and methods).

Free energy minimization for the confined frustrated chiral nematic LC with the cholesteric pitch to cell thickness ratio of ~ 1.2 promotes the formation of various cholesteric fingers and topological solitons like skyrmions, torons, and hopfions, [28] all embedded in a uniform homeotropic background with the far-field director $\mathbf{N}_0$ along the normal to substrates, as prescribed by the boundary conditions. These localized director structures arise to embed twisted regions within the unwound $\mathbf{N_0}$ background, which helps to locally alleviate the frustration associated with the incompatibility of perpendicular surface boundary conditions and the helicoidal twist tendency. Among these solitonic configurations are the cholesteric finger structures of the third kind depicted in Fig. 4.1(a), which are of interest for the present study. Within the translationally invariant director structure of this finger, the director field $\mathbf{N}(r)$ twists by π from left to right side of the cross-section (Fig. 4.1(a)), with the twist handedness matching that of the equilibrium chiral LC, as determined by the chirality of the molecular chiral additive. Singular line defects within the structure of these fingers, which terminate the bulk π-twist of $\mathbf{N}(r)$ near the confining substrates to again match the director to perpendicular boundary conditions, serve as linear topological traps for both the plasmonic and semiconductor nanoparticles (Fig. 4.1(c)). In a cross-section orthogonal to the axes of the finger and the defect lines, the molecular orientations of LC molecules and $\mathbf{N}$ around the cores (depicted as red wires in Fig. 4.1(b)) of the defect lines rotate by π while tracing the Möbius-strip-like patterns, with these orientations becoming undefined within the core (Fig. 4.1(b)). Thus, these cores have reduced scalar order parameter as compared to that of the bulk of LC and, in the simplest way, can be understood within the isotropic defect core model. [29]

Because of the associated increased free energy density, singular defect core regions can act as linear traps to spatially confine various nanoparticles (Fig. 4.1(c)). [**?**] Confinement of nanoparticles within a defect core reduces the overall free energy by displacing the energetically costly defect region with the nanoparticle. The nanoparticles entrapped inside of these defect

regions are strongly nano-confined in terms of their spatial positions in a plane orthogonal to the line defect (Fig. 4.1(c)), but undergo Brownian motion and diffuse freely along the length of the line defect due to thermal energy (Fig. 4.1(f, g)). The one-dimensional diffusion coefficients measured for individual defect-entrapped GNRs and QDs are estimated to be, respectively, 1.9×10^{-2} $\mu m^2 s^{-1}$ and 3.4×10^{-2} $\mu m^2 s^{-1}$ at room temperature, though they increase as the temperature is increased (for example, at the elevated temperature of 45 °C, we obtain the diffusion coefficient $D_{\mathrm{GNR}} = 2.7 \times 10^{-2} = \mu m^2 s^{-1}$ for the GNRs). Furthermore, the rod-like GNRs spontaneously align with their long axes along the defect line (Fig. 4.1(c)) because this maximally reduces the free-energy-cost of the core by maximally displacing high-energy regions with the volume of the nanoparticle. Although a detailed quantitative picture of the interactions between a singular defect line and nanoparticles requires numerical modeling based on the tensorial order parameter, [30] one can gain insights into the physical underpinnings behind our observations via simple estimates of potential energies involved. The simplest model of the defect lines singular core assumes that this core is an isotropic liquid and that its energetic cost is proportional to $k_B \Delta T_c$, where k_B is the Boltzmann constant and

$$\Delta T_c = T_{\mathrm{NI}} - T \tag{4.1}$$

is the difference between the nematic-isotropic transition temperature T_{NI} and the samples absolute temperature T. [30] The temperature dependence of diameter of the singular lines core can be estimated by comparing the free energy cost of melting LC to the isotropic state and the free energy of producing strong elastic distortions around the defect lines core, [30] which yields

$$d_c = \frac{2MK}{\sqrt{\rho N_A k_B \Delta T_c}}, \tag{4.2}$$

where K is the average Frank elastic constant, M is the molecular mass, N_A is the Avogadros number and ρ is the density of the LC. Although a typical value for d_c deep in the nematic phase is $\approx$ 10 nm, [31, 32] by varying ΔT_c one can tune d_c in the range $10 - 100$ nm. This capability provides a key advantage to the implementation of our experiments, as discussed below. The defect lines free energy reduction associated with the placement of a nanoparticle within its core can be

estimated using the free energy cost per unit length of a half-integer disclination line

$$W \approx \frac{\pi}{4} K \ln\left(\frac{2R}{d_c}\right) + W_c, \tag{4.3}$$

where R is a characteristic dimension of the sample and W_c is energy per unit length of the isotropic disclination core. [30] By following, [30] one can calculate the defects energies reduction that enable nanoparticle trapping as $\approx 23 k_B T$ for QDs and $450 k_B T$ for GNRs. Owing to the smaller polarizable volume of the QDs, laser tweezers at moderate powers of up to 50 mW and for the polarizability of nanoparticles do not exert optical trapping potential that would be sufficient to trap QDs, consistent with the well-known limitations of optical trapping of objects that are ≈ 10 nm or smaller in size. [33,34] At the same time, laser powers of $5-7$ mW were sufficient to robustly manipulate colloidal GNRs within the LC. The strength of these laser traps was insufficient to remove QDs or GNRs from the singular line traps[33, 34] or to reorient GNRs away from the long axis parallel to the defect line, [33,34] though these laser tweezers allowed for the translation of GNRs along the defect lines while controllably forming the sandwich structure. Since the laser manipulation of the GNRs by the optical tweezer can result in the increase of surface temperature of the gold particle, due to the absorption of 1064 nm laser light, this in turn could potentially cause local melting and transformation of the LC from nematic to isotropic phase. Following the method described in [35] (see details provided in Appendix A), we estimate maximum of $\sim$ 2 °C increase intemperature at the surface of silica layer of the GNR, when manipulated with trapping laser beam of 7 mW power at the sample plane. [35] This is consistent with our previous studies [36, 37] and with the fact that we never observe local melting transitions under the polarizing microscope (note that the nematic-isotropic transition is of the first order, associated with a sharp interface that would be easy to detect under a polarizing microscope if such a local melting transition were to occur). To quantify the strength of the topological defect line traps, we have characterized their stiffness. By measuring the small spatial displacements arising from the Brownian motion of the entrapped GNR and QD particles in the direction perpendicular to the defect line with the help of video microscopy (Fig. 4.2(a)), we find the defect traps stiffness $\xi_{\mathrm{DT}} = 4.2$ pN/μm. [7, 37] This ensures

a robust one-dimensional topological defect confinement of nanoparticles in our experiments. The studied silica-coated GNRs can be also effectively manipulated with the help of optical tweezers utilizing a 1064 nm fiber laser, which are described in detail elsewhere. [36, 40] Once entrapped within a line defects core, GNRs can be optically translated by pushing the nanoparticles by means of the optical forces generated by tightly focused infrared laser beam of the tweezers along the length of the line defect, which helps to realize the desired ideal configuration of nanoparticles depicted in Fig. 4.1(c). Within this basic configuration used in our work (Fig. 4.1(c)), a single QD nanoparticle is sandwiched between two GNRs, all positioned with their centers of mass, on average, along a single straight line coinciding with the central axis of the defect core. The GNRs are manipulated with laser tweezers to form a sandwhich-like configuration of the nanoparticles as depicted in Fig. 4.1(c), as further detailed below, which is important for the exploration of plasmon-exciton interactions associated with these nanoparticles. Such a linear configuration of spatially co-localized nanoparticles prompts strong changes in the photophysics of the QD particle, owing to the interaction between the excitonic resonance of the QD and surface plasmon resonance of the GNR.

4.4 Elastic interactions between the nanoparticles in a LC line defect

GNR particles, along with the silica shells and surfactant monolayers around them, have a diameter in the range $50 - 55$ nm, larger than the effective diameter of the reduced-order core regions of the line defect. The DMOAP functionalization assures perpendicular surface boundary conditions for $\mathbf{N}(r)$ at their surface in the locations where parts of this surface protrude outside of the melted reduced-order defect core (Fig. 4.1(c)). These radial (locally perpendicular to the cylindrical surface) boundary conditions for $\mathbf{N}(r)$ at the GNR periphery are incompatible with the π-twisted Möbius-strip-like $\mathbf{N}(r)$ structure of the twist disclination around its core. This causes further elastic distortions, which effectively create a repulsive interaction between the GNR particles (note that previously colloidal interactions mediated by elasticity were considered in the bulk of uniformly aligned LCs [41, 42]). The elastic repulsion stems from the fact that these additional

elastic distortions are squeezed to a smaller region when two GNRs are brought closer along the defect line, which costs more elastic energy. We have characterized the interaction potential between two GNR particles by tracing the inter-particle spacing with time when they are moved close to each other with the help of optical tweezers and then released (Fig. 4.2(b)). When the temperature of the LC is increased, the effective diameter of the melted defect core becomes larger, leading to a reduction in the repulsive interaction potential, as demonstrated in Fig. 4.2(b). It should be noted that the van der Waals force of attraction between the GNRs at these distances are negligible compared to the repulsive elastic interaction between the particles (see details provided in Appendix A). [43] Due to the repulsive interaction, GNR particles entrapped inside the core of the line defect form an assembly of equally spaced particles, with the one-dimensional crystal-like order emerging at sufficiently high concentrations and tweezer-assisted or other types of confinement along the length of the defect line (Fig. 4.2(c),(d)). The maximum repulsive potential ranges from 10 to 200 k_BT (Fig. 4.2(b)), making one-dimensional dispersions of GNRs along the defect cores robust with respect to thermal fluctuations (Fig. 4.2(e)). Under these conditions, relatively large GNRs mutually repel and never aggregate, though they can be pushed towards each other to effectively form dimers at elevated temperatures (still below the nematic-isotropic transition temperature) with the help of laser tweezers, which we will utilize in the experiments described below.

Unlike GNRs, because their outer shell diameter is always smaller than the defect line core, QD particles entrapped inside line defects do not exhibit strong elasticity-mediated repulsive interactions. However, when the number density of QDs is high, they can interact with each other to form small aggregates, so that similar elasticity-mediated repulsive interaction between the aggregates emerge when they grow larger than the diameter of the defect core (Fig. 4.2(c)). In the present study, however, we use vanishingly small number densities of QDs to ensure individually dispersed QDs entrapped within defect lines, which is further confirmed by characterization detailed below.

4.5 Plasmon-exciton interaction studies

In our experiments, we first locate a single QD inside a line defect on the basis of analyzing its luminescence blinking characteristics when the QD is excited with the 436 nm line from a mercury lamp. Individual GNR particles are detected/imaged using dark field microscopy, which can be done in parallel with their optical manipulation using laser tweezers. The experimental configuration depicted in Fig. 4.1(c) is realized by using an optical tweezer to move the GNRs close to the QD particle in-between. To reduce the strength of repulsive interaction between the GNR particles, we increase the temperature of the LC medium with an objective heater (Bioptechs). The CdSe/ZnS QDs used in our experiments have an emission peak centered at 620 nm, matched to the longitudinal SPR peak of GNR particles, as shown in Fig. 4.3(a). Since the surface of the GNR is coated with a silica shell, the shift in the localized surface plasmon resonance (LSPR) peak due to the higher effective refractive index of the liquid crystal E7 is minimal. However, when two GNRs are brought close to each other, their longitudinal LSPR peak shifts to the higher wavelength owing to the plasmon coupling between the two GNRs [44, 45] (Fig. 4.3(a)). Observation of the LSPR shift and measurements of the scattering spectra of the GNRs in our sandwich assembly are limited due to the strong birefringence (Fig. 4.3(c)) and thermal fluctuations of the LC line defect. We estimate a redshift ~ 15 nm for the longitudinal LSPR peak of the GNR, when they are assembled to form a sandwich structure as depicted in Fig. 4.3(d) (Appendix A, Fig. A.3). It is evident that considerable spectral overlap between the QD emission and longitudinal LSPR of GNRs is present in the sandwich assembly. However, the $|\mathbf{E}|^2$ field enhancement spectrum of the sandwich assembly peaks at wavelengths slightly longer than the absorption maximum as shown in Fig. 4.3(b) and Fig. A.3 in Appendix A.

The linear arrangement of the GNRs, with the nanoscale separation between their surfaces controlled by tweezers, induces strong optical interaction between the SPR and QD emission due to the high Purcell factor achievable with such a configuration. To obtain additional insights into this

phenomenon, we simulated the plasmonic field enhancement by using the Discrete Dipole Approximation (DDA) method. [46–49] We plot $|\mathbf{E}|^2$ for an unpolarized light at wavelength 473 nm and 620 nm incident on the particles, as shown in Fig. 4.3(e,f). We verified these calculations by doing full electromagnetic simulations using COMSOL Multiphysics as shown in Fig. A.3 (Appendix A). The strong plasmonic field enhancement (~ 250 at QD location) arising from the LPSR of GNRs at 620 nm is evident and mediates plasmon-exciton interactions that we discuss next.

We have analyzed the luminescence of individual QDs with the help of a photon antibunching setup (Fig. 4.4(a)), which helps us to identify a single QD particle when it is far away from the GNRs. We first identify a single QD located inside the line defect as shown in Fig. 4.4(b), with two GNRs on both sides of the QD along the defect line but far away from it (Fig. 4.4(c)). Light emission from this QD is analyzed using the antibunching technique, as shown in Fig. 4.4(h). The data is fit using the expression

$$g^{(2)}(t) = g^{(2)}(0) + \frac{1 - e^{-|t/\tau|}}{N}, \tag{4.4}$$

where τ is the exciton lifetime, N is the number of photons and $g^{(2)}(0)$ is the second order correlation at the coincidence time $t = 0$. [50, 51] Under the low excitation regime, the ratio of biexciton to exciton quantum yields of single QDs can be determined from the value of $g^{(2)}(0)$. Single photon emission is characterized by $g^{(2)}(0) = 0$ and $N = 1$, although experimental observations are limited by the dark counts of the detector offsetting the value of N and $g^{(2)}(0)$ as shown previously. [52] For the data shown in Fig. 4.4(h), we obtain $N = 1.5$, $g^{(2)}(0) = 0.25$ indicating single photon emission, with an exciton lifetime $\tau = 14.2$ ns, which is close to the value previously reported for CdSe QDs with core-shell structure. [53] Following this characterization of the QD alone, we moved the GNR particles closer to the QD by using the optical tweezer, realizing the "sandwich" configuration depicted in Fig. 4.1(c). In order to reduce the repulsive interaction between the GNRs, the sample temperature was raised to 45 °C with an objective heater and cooled to room temperature after the assembly process (Fig. 4.4(b-g)). We observed considerable changes in the antibunching data

curve when the QD particle was squeezed between the GNRs, as shown in Fig. 4.4(i). Fitting similarly to that described above yields $N = 2.67$, $g^{(2)}(0) = 0.6$ and a faster radiative decay rate of $\tau = 5$ ns. These results are possible indications of multiphoton emission from QDs with a faster decay rate modified by the Purcell effect. In order to analyze the fluorescence enhancement and blinking characteristics of the QD particles, we measured the fluorescence trajectories of the particle before and after forming the sandwich assembly. Fig. 4.5(a, b) represent typical blinking trajectories of the QD particles collected with a binning time of 10 ms, without GNRs (Fig. 4.5(a)) and within sandwich structure (Fig. 4.5(b)), respectively. It is clear that the QD particle stays predominantly in the "on" state after sandwiching the particle between two GNRs as shown by the histogram presented in the right-hand side of the Fig. 4.5(a, b). Moreover, the QD emission intensity is enhanced by almost two times indicating the enhanced detection of the QD after forming the sandwich assembly caused by preferential beaming of the emission light due to the antenna-like arrangement. [54] Furthermore, we have performed a detailed analysis of the blinking trajectories by constant thresholding method and calculated the probability distribution of "on" (t_{on}) and "off" (t_{off}) times of the fluorescence emission as shown in Fig. 4.5(c, d). A power law dependence, typical of the QD emission with increased "on" state probability is evident from Fig. 4.5(c, d). Additional insight to the exciton-plasmon interaction is gained by analyzing the fluorescence decay curves shown in Fig. 4.5(e). The decay curves can be well fitted using a biexponential function,

$$I = A_1 e^{-t/\tau_1} + A_2 e^{-t/\tau_2}, \tag{4.5}$$

where τ_1 and τ_2 are the slow and fast lifetime component, A_1 and A_2 represent the corresponding amplitudes, respectively. Before the formation of the sandwich assembly, the QD fluorescence yields typical values of decay time $\tau_1 = 1.1$ ns and $\tau_2 = 19$ ns. On the other hand, when sandwiched between GNRs, the faster decay component is more prominent and the lifetime of the slower decay component is also reduced to 5 ns, indicating more than three times increase in the decay rate. We identify the slower decay component associated with the radiative decay as corresponding to the single exciton emission. Although the reported values for the lifetime of the biexciton emission is of

the order of hundreds of picoseconds, we believe the faster decay component in our measurements represents the radiative decay corresponding to the biexciton emission. Accurate estimation of the biexciton decay time in our experiment is limited by the time resolution of the TCSPC hardware. The values of decay rates estimated by fitting double exponential curves (Fig. 4.5(e)) match well with the values extracted from the antibunching data (Fig. 4.4(h, i)). Both experiments convincingly show that the proximity of plasmonic particles increases the radiative decay rate of the QD by more than three times, indicating a strong coupling of the QD emission with the SPR of GNR particles. The observed optical properties of the QD particle in sandwich assemblies were highly reproducible and found to be independent of the excitation polarization. Moreover, the analysis of emission intensity of the QD particle revealed minimal effect on the excitation polarization; which is expected due to the relatively modest field enhancement at the excitation wavelength as demonstrated in Fig. 4.3(f). The resultant absorption enhancement of the QD absorption in the sandwich assembly is expected to be minimal at the excitation wavelength used in our experiments 56. Measurements of the fluorescence spectra of QD particle in the sandwich assembly indicate increased fluctuations in the fluorescence peak position with respect to the spectra collected before forming the sandwich assembly (Fig. A.2, Appendix A). The experiments were repeated on several QDs GNR pairs in line defects forming a sandwich assembly and the observed optical properties are found to be highly reproducible (Fig. 4.6). The values of g(2)(0), emission enhancement and fluorescence decay curves are shown in Fig. 4.6(a,b) and Fig. A.1, and Table A.1 in Appendix A.

The study of multiexciton generation in semiconducting nanostructures has been intensively pursued over the last couple of decades.[56, 57] Recent efforts in this field have been directed towards employing the LSPR of metal nanoparticles for generating multiexcitons in semiconducting nanoparticles, [8–13] though studies on self-assembled nanoparticles have been rarely reported. Reports on QDs deposited on a roughened, gold-coated surface indicate enhanced multiphoton emission and decreased single photon emission on these substrates. [8] The quantum efficiencies of the multiexciton states in a QD are relatively low, due to Auger and other non-radiative decay

channels quenching the multiphoton radiative process. The surface plasmon effects on the higher order exciton states are much different from the effects on the single exciton state.

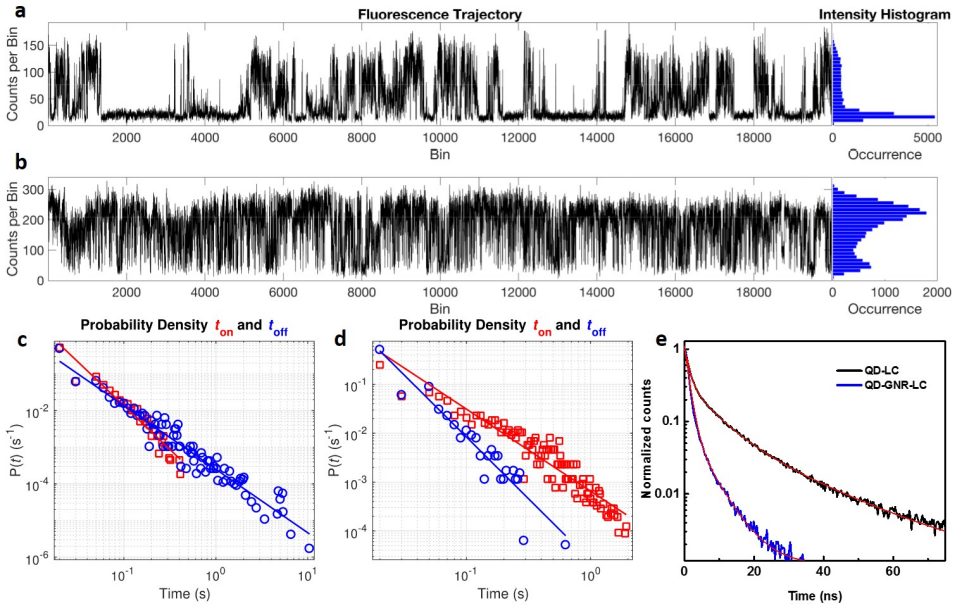

Fig. 4.5: Characterization of fluorescence intermittency and fluorescence decay. (a, b) Fluorescence time traces of a QD particle trapped inside a line defect before (a) and after bringing two GNRs forming a sandwich assembly (b). The "on" and "off" times of the QD particle is presented by the corresponding histogram in the right side. (c, d) Analysis of fluorescence time trace with constant thresholding for the curves presented in (a) and (b) representing the probability density $P(t)$ of sustained "on" (t_{on}) and "off" (t_{off}) times of the QD particles before (c) and after (d) bringing two GNRs forming a sandwich assembly. Solid lines represent linear fits to the data, showing a power law dependence. (e) Typical fluorescence decay curves of a QD particle (black curve), representing a faster fluorescence decay when the QD particle is sandwiched between two GNRs (blue curve). Solid lines represent the double exponential fit to the experimental decay data.

Significant enhancement of the radiative decay rates of the biexcitonic states can be achieved when coupled with SPR, effectively increasing the quantum efficiency of the biexciton states. In our experiments, emission from the QDs couples strongly with SPR of the GNR particles, which could enhance the biexcitonic radiative rates according to the Purcell effect, resulting in an increased probability of multiphoton emission from the QDs. At the same time, the radiative decay rate of the single exciton states are enhanced by almost 4 times, as revealed by the fluorescence decay measurements (Fig. 4.5(e)) and also consistent with previous observations. [7–13] However, based

on the fluorescence trajectories of the QD particles, collected before and after bringing the GNRs, the fluorescence intensity enhancement for the QD particle in the sandwich assemblies is only about 2 times which is expected due to the only modest enhancement of the light collection efficiency in the sandwich geometry. Although the nonradiative energy transfer between the QD and GNR particles can affect the emission properties of the particles, previous studies have shown that biexcitonic states are less affected by this interaction in comparison with the excitonic emission. [10]

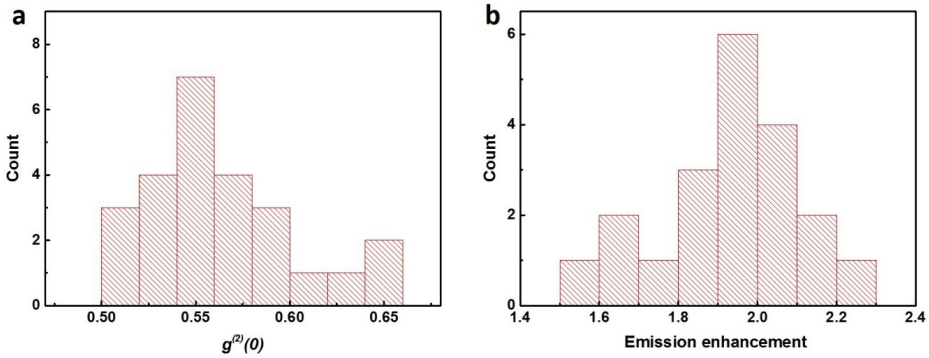

Fig. 4.6: Variations of $g^{(2)}(0)$ and enhancement factor. Histogram representing the variations of $g^{(2)}(0)$ estimated from the photon antibunching measurements (a) and emission enhancement of QD fluorescence (b), calculated based measurements on multiple sandwich assemblies in LC line defect.

Moreover, as intended by our experimental design, specially-designed silica shells around the GNRs ensure that the QDs are separated from the GNR surface by about 10 nm, limiting the non-radiative energy transfer towards GNRs, preventing the complete quenching of the QD emission. At large silica thickness, the effect of plasmon coupling is expected to be diminished resulting in a significant reduction in the Purcell factor and reduced probability for the multiexciton emission. On the other hand, lowering silica thickness is expected to result in strong coupling between the QD emission and LSPR of GNR at the same time decreasing the QD emission due to the increased non radiative decay. In effect, coupling the SPR of the GNRs to the biexciton states of the QD allows for the branching of the biexciton state to multiphoton emission through the enhanced radiative rate of the biexcitonic states of QDs without significant change in the nonradiative Auger dominated

recombination rate, effectively making the non-radiative decay channels of the biexcitonic states less prevalent. The excitation intensity aided by the field enhancement by the GNR provides sufficient field intensity for the generation of multiexciton states in the QD, even though the field enhancement at the excitation wavelength is relatively modest compared to the emission wavelength at 620 nm. The exact modelling of the SPR effect on the higher order states of the QD is challenging due to the complexities of the optical interactions involved. For example, plasmon modes give rise to a strong electric field gradient near the metal particle in the near field which could influence the dipole-forbidden, higher-order interactions in the QD emission. [14, 15] A future successful model should include the interaction of higher-order exciton states with hot electrons, thermal and Auger relaxation in addition to accounting for the delocalization of electron and hole wave functions in case of core-shell type particles. Moreover, the interaction of semiconductor nanoparticles with surface ligands and the host medium will require separate detailed theoretical and experimental studies for more quantitative modeling of the role of SPR on the multiphoton emission from QDs.

4.6 Results and Conclusions

In conclusion, we have demonstrated the use of LC line defects to control the position and orientation of GNR and QD particles to study the optical interaction with a QD in a well-defined geometry and in the bulk of a dielectric LC medium, unaffected by the proximity to a substrate. Our results indicate possible multiphoton emission from a single QD particle when located in between two GNRs, which originates from the strong coupling with the SPR of these rod-like plasmonic nanoparticles. This method provides a useful framework for the study of nanoscopic optical interation between single nanoparticles and can be applied to wide varieties of systems with particles of different shape, chemical composition and dimensions ranging from nanometer to the sub-micrometer size. The orientation of the elastically trapped particles in the line defect can be controlled by tuning the chemical functionalization of the particles surface, which allows one to set well-defined boundary conditions for the molecular alignment at the nanoparticle surface, as needed for controlling inter-particle interactions mediated by the LC. For example, our method could be

extended to the study of plasmon-exciton interactions when using quantum wells [58] or photon-upconverting nanocubes and nanorods [59] instead of the quantum dots used in the present study. Although the present study was performed using individual nanoparticles, it provides insight into the possibility of designing mesostructured composite materials with arrays of defects entrapping both plasmonic and semiconductor nanoparticles, where the optical properties of the medium can be potentially controlled by tuning the inter-particle spacing through the LCs facile response to external stimuli.

4.7 References

[1] S. Dey, J. Zhao, "Plasmonic Effect on Exciton and Multiexciton Emission of Single Quantum Dots," *J. Phys. Chem. Lett.*, 2016 **7** 2921.

[2] C. Livache, E. Izquierdo, B. Martinez, M. Dufour, D. Pierucci, S. Keuleyan, H. Cruguel, L. Becerra, J. L. Fave, H. Aubin, A. Ouerghi, E. Lacaze, M. G. Silly, B. Dubertret, S. Ithurria, E. Lhuillier, "Charge Dynamics and Optolectronic Properties in HgTe Colloidal Quantum Wells," *Nano Lett.* 2017 **17** 4067.

[3] L. Jiang, H. Mundoor, Q. Liu, I. I. Smalyukh, "Electric Switching of Fluorescence Decay in GoldSilicaDye Nematic Nanocolloids Mediated by Surface Plasmons," *ACS Nano*, 2016 **10** 7064.

[4] J. C. Johnson, T. H. Reilly, A. C. Kanarr, J. van de Lagemaat, "The Ultrafast Photophysics of Pentacene Coupled to Surface Plasmon Active Nanohole Films," *J. Phys. Chem. C*, 2009 **113** 6871.

[5] B. Ji, E. Giovanelli, B. Habert, P. Spinicelli, M. Nasilowski, X. Xu, N. Lequeux, J. Hugonin, F. Marquier, J. Greffet, B. Dubertret, "Non-Blinking Quantum Dot With a Plasmonic Nanoshell Resonator," *Nat. Nanotechnol.*, 2015 **10** 170.

[6] D. E. Gómez, K. C. Vernon, P. Mulvaney, T. J. Davis, "Surface Plasmon Mediated Strong ExcitonPhoton Coupling in Semiconductor Nanocrystals," *Nano Lett.* 2010 **10** 274.

[7] P.J. Ackerman, H. Mundoor, I. I. Smalyukh, J. van de Lagemaat, "PlasmonExciton Interactions Probed Using Spatial Coentrapment of Nanoparticles by Topological Singularities," *ACS Nano*, 2015 **9** 12392.

[8] S. J. LeBlanc, M. R. McClanahan, M. Jones, P. J. Moyer, "Enhancement of Multiphoton Emission from Single CdSe Quantum Dots Coupled to Gold Films," *Nano Lett.* 2013 **13** 1662.

[9] S. Masuo, K. Kanetaka, R. Sato, T. Teranishi, "Direct Observation of Multiphoton Emission Enhancement from a Single Quantum Dot Using AFM Manipulation of a Cubic Gold Nanoparticle," *ACS Photonics*, 2016 **3** 109.

[10] Y.-S. Park, Y. Ghosh, Y. Chen, A. Piryatinski, P. Xu, N. H. Mack, H.-L. Wang, V. I. Klimov, J. A. Hollingsworth, H. Htoon, "Super-Poissonian Statistics of Photon Emission from Single CdSe-CdS Core-Shell Nanocrystals Coupled to Metal Nanostructures," *Phys. Rev. Lett.*, 2013 **110** 117401.

[11] S. Dey, Y. Zhou, X. Tian, J. A. Jenkins, O. Chen, S. Zou, J. Zhao, J. "An Experimental and Theoretical Mechanistic Study of Biexciton Quantum Yield Enhancement in Single Quantum Dots Near Gold Nanoparticles," *Nanoscale*, 2015 **7** 6851.

[12] H. Naiki, S. Masuo, S. Machida, A. Itaya, "Single-Photon Emission Behavior of Isolated CdSe/ZnS Quantum Dots Interacting with the Localized Surface Plasmon Resonance of Silver Nanoparticles," *J. Phys. Chem. C.*, 2011 **115** 23299.

[13] K. Matsuzaki, S. Vassant, H. W. Liu, A. Dutschke, B. Hoffmann, X. Chen, S. Christiansen, M. R. Buck, J. A. Hollingsworth, S. Gtzinger, V. Sandoghdar, "Strong Plasmonic Enhancement of Biexciton Emission: Controlled Coupling of a Single Quantum Dot to a Gold Nanocone Antenna," *Sci. Rep.*, 2017 **7** 42307.

[14] P. K. Jain, D. Ghosh, R. Baer, E. Rabani, P. A. Alivisatos, "Near-Field Manipulation of Spectroscopic Selection Rules on the Nanoscale," *Proc. Natl. Acad. Sci. U.S.A.*, 2012 **109** 8016.

[15] M. L. Andersen, S. Stobbe, A. S. Sorensen, P. Lodahl, "Strongly Modified PlasmonMatter Interaction with Mesoscopic Quantum Emitters," *Nat. Phys.*, 2011 **7** 215.

[16] P. Zijlstra, P. M. R. Paulo, M. Orrit, "Optical Detection of Single Non-Absorbing Molecules Using the Surface Plasmon Resonance of a Gold Nanorod," *Nat. Nanotechnol.*, 2012 **7** 379.

[17] V. G. Kravets, F. Schedin, R. Jalil, L. Britnell, R. V. Gorbachev, D. Ansell, B. Thackray, K. S. Novoselov, A. K. Geim, A. V. Kabashin, A. N. Grigorenko, "Singular Phase Nano-Optics In Plasmonic Metamaterials for Label-Free Single-Molecule Detection," *Nat. Mater.*, 2013 **12** 304.

[18] L. Rogobete, F. Kaminski, M. Agio, V. Sandoghdar, "Design of Plasmonic Nanoantennae for Enhancing Spontaneous Emission," *Opt. Lett.*, 2007 **32** 1623.

[19] Qi-C. Sun, H. Mundoor, J. C. Ribot, V. Singh, I. I. Smalyukh, P. Nagpal, "Plasmon-Enhanced Energy Transfer for Improved Upconversion of Infrared Radiation in Doped-Lanthanide Nanocrystals," *Nano Lett.*, 2014 **14** 101.

[20] W. R. Erwin, H. F. Zarick, E. M. Talbert, R. Bardhan, "Light Trapping in Mesoporous Solar Cells with Plasmonic Nanostructures," *Energy Environ. Sci.*, 2016 **9** 1577.

[21] H. A. Atwater, A. Polman, "Plasmonics for Improved Photovoltaic Devices," *Nat. Mater.*, 2010 **9** 205.

[22] A. J. Morfa, K. L. Rowlen, T. H. Reilly, M. J. Romero, J. van de Lagemaat, "Plasmon-Enhanced Solar Energy Conversion in Organic Bulk Heterojunction Photovoltaics," *Appl. Phys. Lett.*, 2008 **92** 013504.

[23] K. Wu; J. Chen, J. R. McBride, T. Lian, "Charge transfer. Efficient Hot-Electron Transfer by a Plasmon-Induced Interfacial Charge-Transfer Transition," *Science*, 2015 **349** 632.

[24] I. Thomann, B. A. Pinaud, Z. Chen, B. M. Clemens, T. F. Jaramillo, M. L. Brongersma, "Plasmon Enhanced Solar-to-Fuel Energy Conversion," *Nano Lett.*, 2011 **11** 3440.

[25] J. Perez-Juste, L. M. Liz-Marzan, S. Carnie, D. Y. C. Chan, Mulvaney, P. "Electric-Field-Directed Growth of Gold Nanorods in Aqueous Surfactant Solutions," *Adv. Funct. Mater.*, 2004 **14** 571.

[26] X. Ye, L. Jin, H. Caglayan, J. Chen, G. Xing, C. Zheng, V. Doan-Nguyen, Y. Kang, N. Engheta, C. R. Kagan, C. B. Murray, "Improved Size-Tunable Synthesis of Monodisperse Gold Nanorods Through the Use of Aromatic Additives," *ACS Nano*, 2012 **6** 2804.

[27] G. H. Sheetah, Q. Liu, I. I. Smalyukh, "Self-assembly of Predesigned Optical Materials in Nematic Codispersions of Plasmonic Nanorods," *Optics Letters*, 2016 **41** 4899.

[28] P. J. Ackerman, I. I. Smalyukh, "Diversity of Knot Solitons in Liquid Crystals Manifested by Linking of Preimages in Torons and Hopfions," *Phys Rev X*, 2017 **7** 011006.

[29] "P. M. Chaikin, T. C. Lubensky, Principles of Condensed Matter Physics," *Cambridge Univ. Press*, 1995.

[30] P. G. de Gennes, J. Prost, "The Physics of Liquid Crystals," *2nd ed. Clarendon*, 1993.

[31] X. Wang, D.S. Miller, E. Bukusoglu, J. J. de Pablo, N. L. Abbott, "Topological Defects In Liquid Crystals as Templates for Molecular Self-Assembly," *Nat. Mater.*, 2016 **15** 106.

[32] M. Ravnik, S. Zumer, "Landau-De Gennes Modelling of Nematic Liquid Crystal Colloids," *Liq. Cryst.*, 2009 **36** 1201.

[33] A. Ashkin, J. M. Dziedzic, J. E. Bjorkholm, S. Chu, "Observation of a Single-Beam Gradient Force Optical Trap for Dielectric Particles," *Opt. Lett.*, 1986 **11** 288.

[34] O. M. Marag, P. H. Jones, P. G. Gucciardi, G. Volpe, A. C. Ferrari, "Optical Trapping And Manipulation of Nanostructures," *Nat. Nanotechnol.*, 2013 **8** 807.

[35] A. Kyrsting, P. M.Bendix, D. G. Stamou, L. B. Oddershede, "Heat Profiling of Three-Dimensionally Optically Trapped Gold Nanoparticles using Vesicle Cargo Release," *Nano Lett.*, 2011 **11** 888.

[36] B. Senyuk, J. S. Evans, P. J. Ackerman, T. Lee, P. Manna, L. Vigderman, E. R. Zubarev, J. van de Lagemaat, I. I. Smalyukh, "Shape-Dependent Oriented Trapping and Scaffolding of Plasmonic Nanoparticles by Topological Defects for Self-Assembly of Colloidal Dimers in Liquid Crystals," *Nano Lett.*, 2012 **12** 955.

[37] H. Mundoor, T. Lee, D. G. Gann, P. J. Ackerman, B. Senyuk, J. van de Lagemaat, I. I. Smalyukh, "Optically and Elastically Assembled Plasmonic Nanoantennae for Spatially Resolved Characterization of Chemical Composition in Soft Matter Systems Using Surface Enhanced Spontaneous and Stimulated Raman Scattering," *J. Appl. Phys.*, 2014 **116** 063511.

[38] F. Hajizadeh, S. N. S. Reihani, "Optimized Optical Trapping of Gold Nanoparticles," *Opt. Express*, 2010 **18** 551.

[39] P. M. Hansen, V. K. Bhatia, N. Harrit, L. Oddershede, "Expanding the Optical Trapping Range of Gold Nanoparticles," *Nano Lett.*, 2005 **5** 1937.

[40] J. S. Evans, Y. Sun, B. Senyuk, P. Keller, V. M. Pergamenshchik, T. Lee, I. I. Smalyukh, "Active Shape-Morphing Elastomeric Colloids in Short-Pitch Cholesteric Liquid Crystals," *Phys. Rev. Lett.*, 2013 **110** 187802.

[41] P. Poulin, H. Stark, T. C. Lubensky, D. A. Weitz, "Novel Colloidal Interactions in Anisotropic Fluids," *Science*, 1997 **275** 1770.

[42] H. Mundoor, B. Senyuk, I. I. Smalyukh, "Triclinic Nematic Colloidal Crystals from Competing Elastic and Electrostatic Interactions," *Science*, 2016 **352** 69.

[43] J. Gargiulo, I. L. Violi, S. Cerrota, L. Chvátal, E. Cortés, E. M. Perassi, F. Diaz, P. Zemnek, F. D. Stefani, "Accuracy and Mechanistic Details of Optical Printing of Single Au and Ag Nanoparticles," *ACS Nano*, 2017 **11** 9678.

[44] K. G. Thomas, S. Barazzouk, B. I. Ipe, S. T. .S. Joseph, P. V. Kamat, "Uniaxial Plasmon Coupling Through Longitudinal Self-Assembly of Gold Nanorods," *J. Phys. Chem. B*, 2004 **108** 13066.

[45] P. K. Jain, S. Eustis, M. A. El-Sayed, "Plasmon Coupling in Nanorod Assemblies: Optical Absorption, Discrete Dipole Approximation Simulation, and Exciton-Coupling Model," *J. Phys. Chem. B*, 2006 **110** 18243.

[46] B. T. Draine, P. J. Flatau, "Discrete-Dipole Approximation for Scattering Calculations," *J. Opt. Soc. Am. A*, 1994 **11** 1491.

[47] B. T. Draine, P. J. Flatau, "Discrete-Dipole Approximation for Periodic Targets: Theory and Tests," *J. Opt. Soc. Am. A*, 2008 **25** 2593.

[48] P. J. Flatau, B. T. Draine, "Fast Near Field Calculations in the Discrete Dipole Approximation for Regular Rectilinear Grids," *Optics Express*, 2012 **20** 1247.

[49] P. K. Jain, N. Sobh, J. Smith, A. R. N. Sobh, S. White, J. Faucheaux, J. Feser, "nanoDDSCAT," https://nanohub.org/resources/dda. 2015, DOI: 10.4231/D32V2CB3M.

[50] S. C. Kitson, P. Jonsson, J. G. Rarity, P. R. Tapster, "Intensity Fluctuation Spectroscopy of Small Numbers of Dye Molecules In A Microcavity," *Phys. Rev. A*, 1998 **58** 620.

[51] C. W. Hollars, S. M. Lane, T. Huser, "Controlled Non-Classical Photon Emission from Single Conjugated Polymer Molecules," *Chem. Phys. Lett.*, 2003 **370** 393.

[52] C. Santori, M. Pelton, G. Solomon, Y. Dale, Y. Yamamoto, "Triggered Single Photons from a Quantum Dot," *Phys. Phys. Rev. Lett.*, 2001 **86** 1502.

[53] B. Omogo, J. F. Aldana, C. D. Heyes, "Radiative and Non-Radiative Lifetime Engineering of Quantum Dots in Multiple Solvents by Surface Atom Stoichiometry and Ligands," *J. Phys. Chem. C*, 2013 **117** 2317.

[54] A. G. Curto, G. Volpe, T. H. Taminiau, M. P. Kreuzer, R. Quidant1, N. F. van Hulst, "Unidirectional Emission of a Quantum Dot Coupled to a Nanoantenna," *Science*, 2010 **329** 930.

[55] S. Arena, F. Cucinotta, O. Di Stefano, A. Cacciola, R. Saija, S. Savasta, "Plasmonic Absorption Enhancement of a Single Quantum Dot," *Plasmonics*, 2015 **10** 955.

[56] B. Patton, W. Langbein, U. Woggon, "Trion, Biexciton, and Exciton Dynamics in Single Self-Assembled CdSe Quantum Dots," *Phys. Rev. B*, 2003 **68** 125316.

[57] Y. -S. Park, A. V. Malko, J. Vela, Y. Chen, Y. Ghosh, F. Garcia-Santamaria, J. A. Hollingsworth, V. I. Klimov, H. Htoon, "Near-Unity Quantum Yields of Biexciton Emission from CdSe/CdS Nanocrystals Measured Using Single-Particle Spectroscopy," *Phys. Rev. Lett.*, 2011 **106** 187401.

[58] S. Jana, P. Davidson, B. Abécassis, "CdSe Nanoplatelets: Living Polymers," *Angew. Chem. Int. Ed.*, 2016 **55** 9371.

[59] S. Gai, C. Li, P. Yang, J. Lin, "Recent Progress in Rare Earth Micro/ Nanocrystals: Soft Chemical Synthesis, Luminescent Properties, and Biomedical Applications," *Chem. Rev.*, 2014 **114** 2343.

[60] M. C. M. Varney, Q. Zhang, B. Senyuk, I. I. Smalyukh, "Self-Assembly of Colloidal Particles in Deformation Landscapes of Electrically Driven Layer Undulations in Cholesteric Liquid Crystals," *Phys. Rev. E*, 2016 **94** 042709.

[61] P. B. Johnson, R. W. Christy, "Optical Constants of the Noble Metals," *Phys. Rev. B*, 1972 **6** 4370.

[62] S. Ninomiya, S. Adachi, "Optical Properties of Cubic and Hexagonal CdSe," *J. Appl. Phys.*, 1995 **78** 4681.

[63] S. Ozaki, S. Adachi, "Optical Constants of Cubic ZnS," *Jpn. J. Appl. Phys.*, 1993 **32** 5008.

[64] G. Abbate, V. Tkachenko, A. Marino, F. Vita, M. Giocondo, A. Mazzulla, L. De Stefano, "Optical Characterization of Liquid Crystals by Combined Ellipsometry and Half-Leaky-Guided-Mode Spectroscopy in the Visible-Near Infrared Range," *J. Appl. Phys.*, 2007 **101** 073105.

Chapter 5

Entropy-driven self-assembly of colloidal membranes of gold nanorods

Adapted from: Manuscript in preparation, Y. Xie, Q. Liu, G. H. Sheetah *et al.*

Chapter Overview

Depletion forces have been widely utilized for guiding colloidal self-assembly, albeit their use in achieving robust assemblies of anisotropic plasmonic nanoparticles into well-defined superstructures remains limited. Here we describe how depletion forces, enabled by a non-adsorbing polymer (dextran), drive spontaneous assembly of monolayer and multilayer colloidal membranes formed by gold nanorods. While forming hexagonal crystalline lattices in the interior of large membranes, gold nanorods exhibit liquid crystalline ordering at the membrane periphery. To maximize entropy, the nanorods twist at the membrane periphery from a vertical orientation in the interior to a horizontal orientation at the colloidal membrane edges. And depending on the spontaneous directionality of the twist of the nanorods at membrane edges, the membranes merge either by forming a π-twist domain wall or a single continuous structure without giving rise to such walls. Transmission Electron Microscopy (TEM), Scanning Electron Microscopy (SEM) imaging and analysis on the basis of theoretical models developed to describe similar behavior in other colloidal nanorod systems provide insights into the physical underpinnings and the potential for realizing complex, yet robust and well defined, plasmonic superstructures through the depletion-driven self-assembly.

5.1 Introduction

Gold nanorods (GNRs) make good building blocks to form various kinds of self-assembled structures. Their shape- and size-dependent optical and plasmonic properties allow for new collective properties to emerge with these self-assembled structures. However, these structures show different fine-textures (FT) within the self-assembled membrane. [1–5] Although self-assembly of some textural structures of GNRs, CdSe nanorods, carbon nanoparticles and filamentous Viruses (*fd*-viruses) have been reported, [6–13] showing textures within the assembly with some types of symmetries, chiral twists, and symmetry breaking morphologies, these distinctive interior textures are not fully understood. Extensive experimental work and theoretical models have demonstrated that diverse textural structures can be controlled and formed within the self-assemblies precisely by tuning the experimental conditions.

GNRs dispersions with uniform size-distribution are good colloidal candidates for the self-assembled structures, and better assist with understanding the different FT. Adding non-adsorbing polymers, such as dextran, induces the GNRs lateral rod-rod attraction via depletion interaction, where dextran polymers exert an osmotic pressure onto the GNRs forcing them to align and form the membranes, maximizing the entropy of the system, and assisting with forming the self assembled structures. The GNRs readily self-assemble into monolayer structures that exhibit diverse interior FT. The self-assembled structures may attach to the interior surfaces of the glass container, which provide a constrained way to design and characterize the complicated FT. Here, we use the polymer dextran with an average stokes radius of 2.36 nm (MW 10K). The growth dynamics of the self-assemblies FT can be controlled by subtle adjustments of the experimental conditions of GNRs concentration, dextran concentration, and duration of thermal perturbation. In addition to the monolayer assemblies, multilayer self-assemblies were also observed, which exhibit rich morphologies of interior FT. Lateral twist and in-plane twist modes, and polarized scattering of the edges as well as the twist domain walls (π-wall) of the self-assembly were observed and investigated using Optical

Microscopy (OM) and Polarized Optical Microscopy (POM) under different subtle adjustments. Details of the internal structures within the self-assembly are demonstrated further with schematics, TEM, and SEM images in Appendix B.

5.1.1 Synthesis of GNRs

GNRs were synthesized in this work with different aspect ratios ranging from 3.8 to 4.4. The synthesis method is a seed-mediated method that has been followed previously. [14] The as-prepared GNRs were stabilized by the surfactant cetyltrimethylammonium bromide (CTAB) in an aqueous dispersion. It is worth noting that having a uniform distribution of GNRs assist with achieving the desired assemblies.

5.1.2 Preparation of the Self-assembly

DEAE-Dextran (average mol wt $10,000$) was purchased from Sigma-Aldrich and used without further purification. First, the dextran solution was prepared with a concentration of 50 mg/ml. GNRs solution was also prepared with an optical density (OD) of $\sim$ 120 and with CTAB concentration of $\sim$ 4 mM. An amount of 2.5 μl of the dextran solution was added into 6 μl of the GNRs dispersion under rapid mixing to prevent any aggregation of the GNRs. A glass cell was then prepared with a glass slide and a cover slip, and using a 15 μm spherical SiO_2 spacer mixed in ultraviolet curing adhesive to fix the thickness of the cell. The mixed solution of dextran and GNRs was then pipetted into the cell and observed under POM. The GNRs concentrations and dextran concentrations were subtly adjusted. Controlling the light illumination was also carried out to tune the different FT of the self-assemblies.

5.1.3 Characterization

POM imaging of GNRs self-assembly was performed using an optical microscope BX-51 (Olympus) with 10×, 20×, 50×, and 100× dry objectives (all from Olympus) that has numerical aperture NA $= 0.3 - 0.9$, a CCD camera (Spot 14.2 Color Mosalc, obtained from Diagnostic

instruments, Inc.), crossed polarizers, and a 530 nm full-wavelength retardation plate. Also, for dark-field imaging, oil objectives were used of 60× and 100× with NA = 1.42. SEM images of the self-assembly were acquired with a Hitachi S-4800 microscope operating at 10 kV for secondary electron imaging.

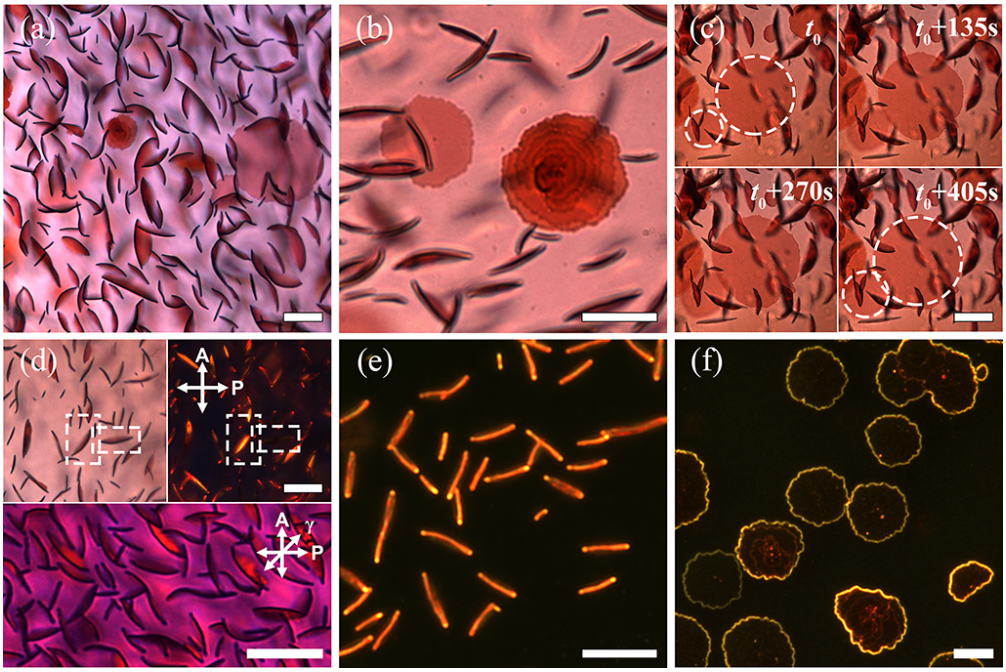

Fig. 5.1: (a) The self-assembly of gold nanorods induced by dextran in an open glass cell. (b) Monolayer and multilayer self-assemblies. (c) The difference growth stages of the self-assembly in the polymer rich aqueous background. (d) Demonstration of the birefringence taken under OM (top-left) and POM (top-right), the bottom image was taken under POM with a retardation plate γ inserted at a 45° angle reflecting the orientation of the director **N** in the well self-assembled structures. The self-assemblies in a side-view and in-plane view are shown in (e, f), respectively, and both were taken with dark-field imaging mode. All scale bars are 20 μm.

5.2 Experimental design

The self-assemblies of membranes with different FT are obtained at various concentrations of dextran, which as mentioned work as the depletant in the aqueous solution that permeate in a glass cell with a thickness of 15 μm. The gold nanorods are coated with a bilayer of a surfactant (CTAB) on their surfaces, and suspended at high concentrations in the thin cell. The geometry of the hard-rods support a stronger attraction along the lateral sides of the rods leading to forming

the membranes. This also gives rise to lamellar self-assembly patterns. Many of these assemblies were observed tilted or flat on the substrate of the thin cell. Fig. 5.1(a) shows a number of membranes form within the glass cell simultaneously. The assemblies show symmetrical growth profile with an average diameter of the assembly in-plane of about 25 μm. Additionally, monolayer and multilayer formations were observed, as shown in Fig. 5.1(b). Noticeably, the multilayer assembly form with decreasing diameters in the proceeding layers compared to its base layer. In this experimental setup, it is difficult to form multilayer assemblies, mainly because of the relatively larger electrostatic repulsion associated with vertical area of the assembly compared to horizontal or in-plane assembly of the membrane edge. The spontaneous self-assembly is mainly induced through depletion attraction, where the assemblies form within intervals of several minutes. The growth process of the self-assemblies were monitored under an OM as marked in the panels in Fig. 5.1(c) indicating a linear growth-rate. The birefringence property of the self-assemblies were also observed under crossed polarizers. The Dotted boxes in Fig. 5.1(d) (top) show both the brightest and the darkest extinction states of the self-assemblies under the crossed polarizers. Where the bright and dark states of the assemblies' edge are observed when at an angle of 45° and 0° with respect to the polarizer P, respectively. In Fig. 5.1(d) (bottom) the director field distribution in these assemblies is demonstrated with the retardation plate γ inserted at a 45° angle with respect to either of the polarizers. Fig. 5.1(e) shows dark-field image of the lamellar self-assemblies with a noticeable edge-scattering that occurs along the lateral side of the monolayer assemblies. While Fig. 5.1(f) shows an in-plane view of the self-assembly with a clear enhanced scattering on the peripheries.

5.3 Conclusion

In summary, a few observations of the fine textures of the GNRs lamellar self-assembly have been reported and under further investigation. Diverse interior fine textures of the self-assemblies were observed with unique director field distributions. Growth dynamic process as well as the polarized dependent properties have also been demonstrated. TEM and SEM images assist with

investigating the π-wall configurations, providing evidence of the twist that occurs in between the volatile unit of two merged self-assemblies. More details and schematics are presented in Appendix B. The results are promising in developing diverse optical, electronic, and plasmonic devices for applications in the fields of sensors, solar energy, and electronics.

5.4 References

[1] L. Vigderman, B. P. Khanal, E. R. Zubarev, "Functional gold nanorods: synthesis, self-assembly, and sensing applications," '*Advanced Materials*, 2012 **24** 4811.

[2] F. Li, D. P. Josephson, A. Stein, "Colloidal assembly: the road from particles to colloidal molecules and crystals," *Angewandte Chemie International Edition*, 2011 **50** 360.

[3] D. A. Walker, B. Kowalczyk, M. O. de la Cruz, B. A. Grzybowski, "Electrostatics at the nanoscale," *Nanoscale*, 2011 **3** 1316.

[4] Q. Liu, M. G. Campbell, J. S. Evans, I. I. Smalyukh, "Orientationally ordered colloidal co-dispersions of gold nanorods and cellulose nanocrystals," *Advanced Materials*, 2014 **26** 7178.

[5] Q. Liu, B. Senyuk, J. Tang, T. Lee, J. Qian, S. He, I. I. Smalyukh, "Plasmonic complex fluids of nematic-like and helicoidal self-assemblies of gold nanorods with negative order parameter," *Physical Review Letters*, 2012 **109** 088301.

[6] Y. Xie, Y. Liang, D. Chen, X. Wu, L. Dai, Q. Liu, "Vortical superlattices in a gold nanorods' self-assembled monolayer," *Nanoscale*, 2014 **6** 3064.

[7] D. V. Talapin, E. V. Shevchenko, C. B. Murray, A. Kornowski, S. Förster, H. Weller, "CdSe and CdSe/CdS nanorod solids," *Journal of the American Chemical Society*, 2004 **126** 12984.

[8] L. S. Li, A. P. Alivisatos, "Origin and Scaling of the Permanent Dipole Moment in CdSe Nanorods," *Advanced Materials*, 2003 **15** 408.

[9] M. Ozawa, H. Goto, M. Kusunoki, E. Osawa, "Continuously growing spiral carbon nanoparticles as the intermediates in the formation of fullerenes and nanoonions," *The Journal of Physical Chemistry B*, 2002 **106** 7135.

[10] F. Kim, S. Kwan, J. Akana, P. Yang, "Langmuir-Blodgett nanorod assembly," *Journal of the American Chemical Society*, 2001 **123** 4360.

[11] L. Kang, T. Gibaud, Z. Dogic, T. C. Lubensky, "Entropic forces stabilize diverse emergent structures in colloidal membranes" *Soft Matter*, 2016 **12** 386.

[12] L.-s. Li, J. Walda, L. Manna, A. P. Alivisatos, "Semiconductor nanorod liquid crystals," *Nano Letters*, 2002 **2** 557.

[13] M.-T. F. Rodrigues, P. M. Ajayan, G. G. Silva, "Fast Vortex-Assisted Self-Assembly of Carbon Nanoparticles on an AirWater Interface," *The Journal of Physical Chemistry B*, 2013 **117** 6524.

[14] X. Ye, L. Jin, H. Caglayan, J. Chen, G. Xing, C. Zheng, V. Doan-Nguyen, Y. Kang, N. Engheta, C. R. Kagan, C. B. Murray, "Improved Size-Tunable Synthesis of Monodisperse Gold Nanorods Through the Use of Aromatic Additives," *ACS Nano*, 2012 **6** 2804.

Chapter 6

Summary and Prospectives for Future Work

LC is a great medium to tune the properties of different nanoparticles, either actively or passively, in a controlled fashion through mechanical coupling between the particles and the LC, especially with the assistance of relatively weak external stimuli. My work involves creating materials that involve complex inclusions of nanoparticles from GNRs with different aspect ratios, dichroic dyes, and QDs, all in different LCs. However, expanding this work to other nanoparticles with different compositions and different properties allows for more opportunities for future research with new directions and perspectives. Herein, I discuss envisioned work and research opportunities that reveal the importance of LCs and their unique adaptation of nanoparticles to create new composites with unique properties that can solve some of the world's current energy problems.

6.1 Plasmonic Aerogels

Aerogels, specifically cellulose-based porous gels, can have a liquid crystalline property with self-assembled nanofibers. They are commonly known for being thermally insulative, flexible, and transparent to the visible light spectrum. This makes them of practical use in energy saving applications. Some initial data were collected as part of collaborative work, and it show some promising results.

Aerogels can be used as a host medium to guest particles with specific properties to create novel systems. For example, incorporating plasmonic nanorods with a well-defined LSPR in the aerogel matrix to make plasmonic aerogels can be beneficial for many different applications. This

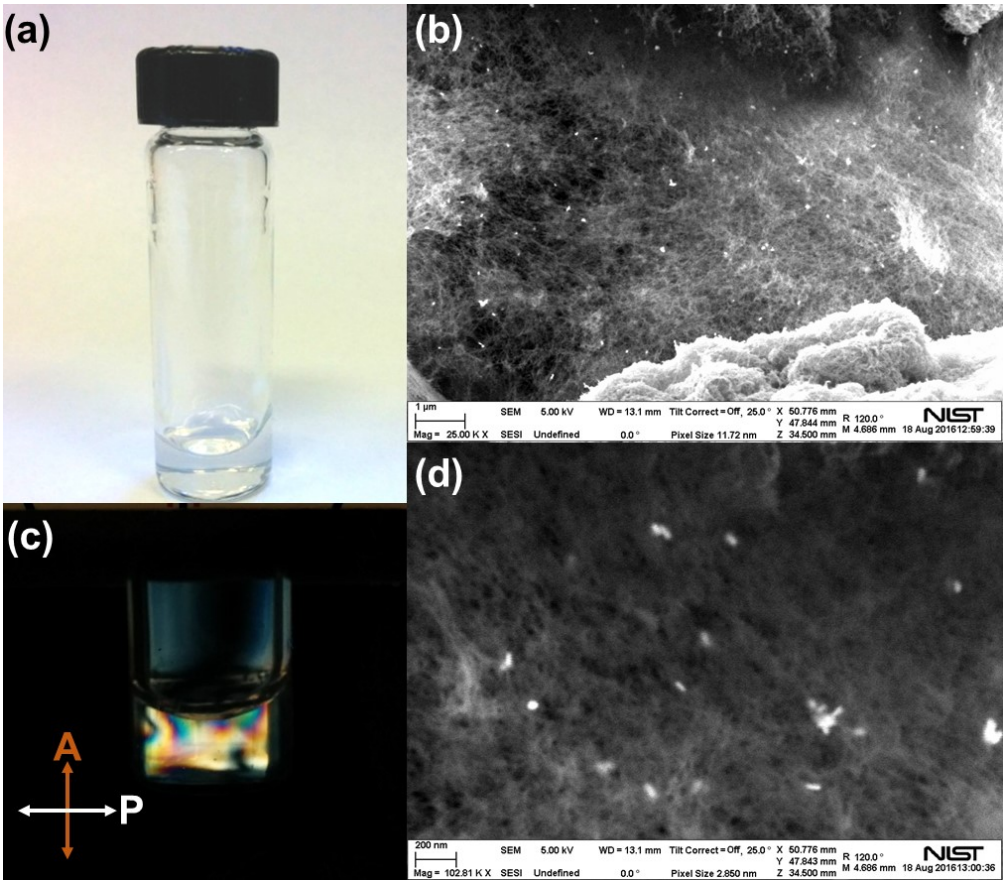

Fig. 6.1: (a) Transparent cellulose LC. The birefringence is observed under a cross polarizer in (c). (b, d) SEM images of different magnifications that show incorporated GNRs in the matrix of the porous cellulose nanofibers.

will be especially unique when there is more order present in the cellulose-based arogels that would allow order in GNRs. Fig. 6.1(a) shows the LC phase of the nanofibers in an aqueous medium, which can be detected with cross polarizers to observe the birefringence, as seen in Fig. 6.1(c).A gel can then be achieved through a series of chemical processes, [1] and later the GNRs can be incorporated in the matrix of the porous cellulose nanofibers, as shown in the SEM images in Fig. 6.1(b, d). Tuning the concentration of GNRs and controlling their orientational order in the bulk of the cellulose nanofibers gel will be of interest for optical meta-material applications, for example. [2]

Moreover, an image of a square inch of the porous aerogel doped with GNRs, demonstrated in Fig. 6.2(b), shows the color of the gel changes in different mediums due to the change of the

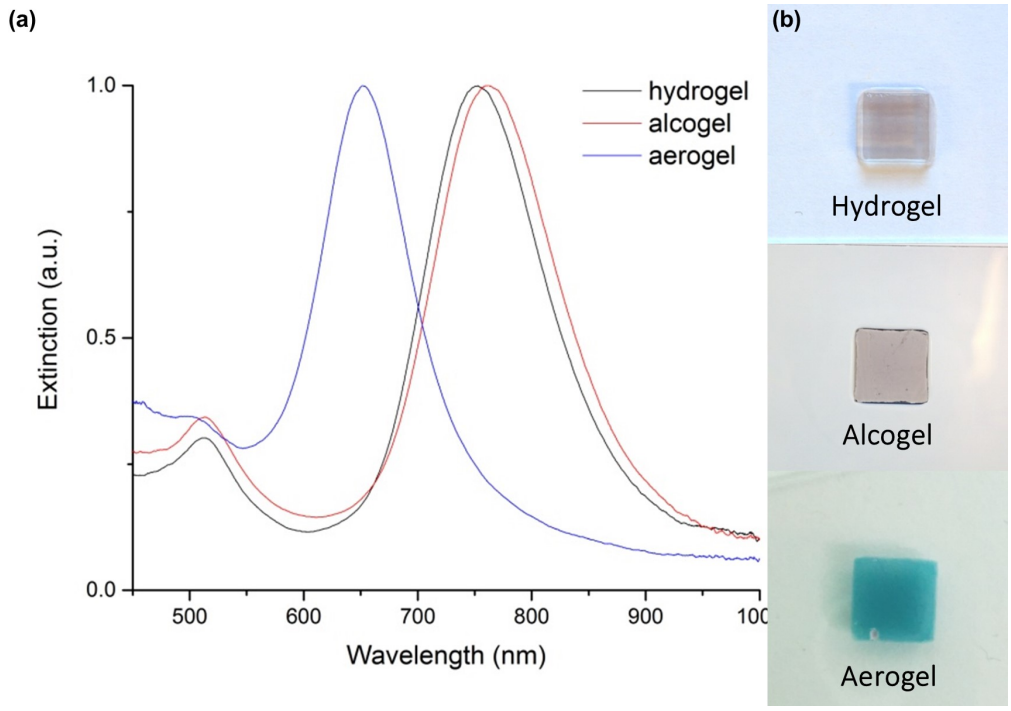

Fig. 6.2: GNRs incorporated in the porous cellulose matrix host in different mediums: water, solvent, and in air. (a) Extinction spectra of GNRs in the cellulose host in water (hydrogel), methanol (alcogel) and in air (aerogel). The LSPR shifts drastically when the porous cellulose nanofibers dries out of the solvent (blue line). The original LSPR of the GNRs used here is 750nm. (b) insets of images of the GNRs inclusions in the gel under the different solvent treatments, and in air.

medium. This affects the spectra of the GNRs, specifically the LSPR peak, since it is the most sensitive to the medium refractive index. As the medium of the porous nanofibers network changes, the LSPR peak of the GNRs built in the porous matrix shifts accordingly. The shift in the LSPR peak can be detected optically via extinction measurements, which can be valuable for chemical sensing applications.

The idea can be extended to incorporate other nanoparticles in the cellulose LC matrix, thus creating different composites with interesting properties that can be useful for other potential applications. Additionally, inclusions of ferromagnetic nanoparticles in the cellulose aerogel matrix create new ferromagnetic aerogels that can be actuated by certain materials in the surrounding environment of the aerogel, as well as creating new materials with magnetic shape memory effects, etc. The possibilities of different applications are endless by creating ordered colloidal dispersions

within gels, which have been approached and patented by Smalyukh's group. [3]

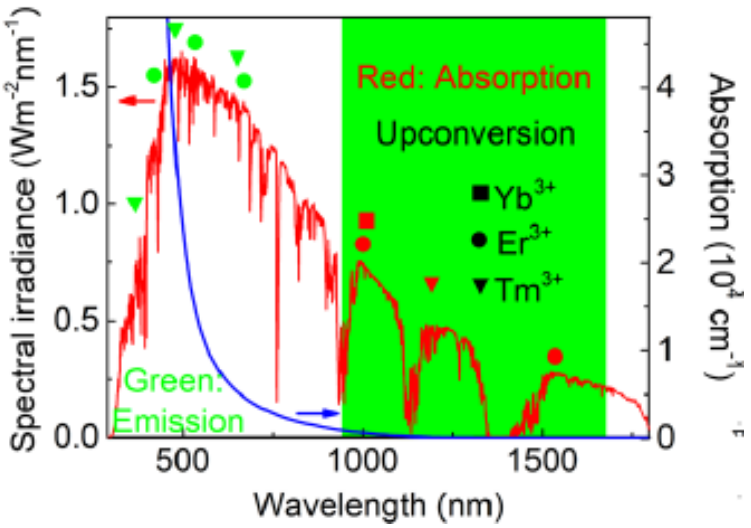

Fig. 6.3: Incident solar radiation spectrum (red curve) and the absorption of silicon (blue curve). More than a third of the incident solar radiation is simply transmitted through a typical silicon photocell. The green shaded region indicates the up-conversion region, where the doped lanthanide ions (Yb^{3+}, Er^{3+}, and Tm^{3+}) absorb the infrared radiation. Green circles and triangles show the visible up-converted emissions of Er^{3+}, and Tm^{3+}, whereas red circles, triangles, and squares indicate the infrared absorption of Er^{3+}, Tm^{3+}, and Yb^{3+}, respectively (Adopted from: Q.-C. Sun, H. Mundoor, *et al. Nano Letters*, 2014, **14**, 101).

6.2 Harvesting solar energy

Another interesting research opportunity is working with Up-Conversion Nano-Particles (UC-NPs), which are especially useful for increasing the efficiency of silicon solar cells. These particles absorb light in the Near-Infrared (NIR) region of the solar spectrum then convert it and emit light with higher energies in the visible range of the spectrum. [4] Figure 6.3 shows the solar spectrum and the silicon absorption spectrum, which is the main element used in conventional photocells. It is clear that most of the NIR part of the spectrum pass through the photocell, since they do not operate in that region. However, one way to increase their efficiency is to convert the NIR light into visible light using UCNPs. The corresponding absorption and emission peaks positions of UCNPs in the solar spectrum are mainly influenced by the chemical composition of the UCNPs, specifically the multiple ionic Lanthanide dopants, as marked in Fig. 6.3. A number of studies have

already demonstrated that the luminescence intensity of the UCNPs can be enhanced when brought within the close proximity of plasmonic nanoparticles. [5,6] For example, matching the LSPR and TSPR peaks of plasmonic nanorods with the UCNPs absorption and emission peaks of the spectra, respectively, further enhancement of the overall up-conversion luminescence can be achieved. The simultaneous enhancement of the excitation and emission in up-conversion luminescence using this plasmonic "double-resonant" gold nanorods can also be controlled by optimizing the separation distance between GNRs and the UCNP. [7]

The synthesis method is reported by F. Wang *et al.* [8] Fig. 6.4(a) A TEM image showing the uniform rod-like shape of the synthesized UCNPs, which are mainly doped with Lanthanide ions. These specific UCNPs absorb in the NIR region around 980nm. And with a process of energy transfer up-conversion, [9] they emit light with higher energy in the visible region of the spectrum, particularly red and green light. The principle behind the design of this composition of UCNPs and plasmonic nanoparticles, GNRs for example, is to create coupling between the two particles with the GNRs LSPR peak at $\sim$ 980 nm in a LC medium, where the GNRs work as antennas enhancing the intensity of the luminescence of these UCNPs through the Purcell effect.[5,6] Figure 6.4(b) illustrates the absorbance spectra of GNRs with an inset of the multi-emission spectra of UCNPs.

Incorporating this assembly of plasmonic nanoparticles and UCNPs in a LC medium gives more control over the experimental settings. Moreover, taking advantage of the switching properties of LCs enables activating the up-conversion luminescence enhancement and/or the absorption of the NIR light using the GNRs either separately or simultaneously. This is especially useful if the visible emissions of the UCNPs are polarization dependent, [8] which allows for novel systems with unique features to emerge.

The UCNPs must be close within the vicinity of the GNRs to enhance the luminescence of the UCNPs. This could be approached either through elastic interaction between the particles in the LC or through electrostatic interaction by chemically treating the GNRs and functionalize their surfaces to have an opposing charge to the positively charged UCNPs. This design also enables

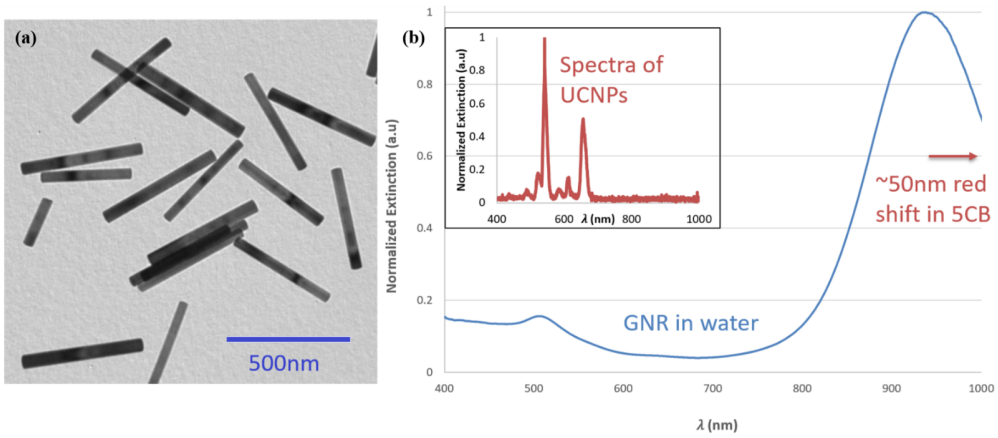

Fig. 6.4: (a) TEM image of UCNPs. (b) A normalized extinction spectra of the GNRs in water, with an LSPR that would shirt in 5CB to localize around the NIR of light spectrum ($\sim$ 980nm) enhancing the absorbnce of the UCNPs. The inset of a red curve shows the normalized extinction spectra of UCNPs; a multicolor emission in the red and green region of the spectra after absorbing light from a continuum wave laser in the NIR with the wavelength of 980nm.

single particle analysis, which would lead to a detailed understanding of interactions between these particles, just like the work done with QDs and GNRs in chapter four. [10]

6.3 Smart windows

In this section, I demonstrate possible consideration to further utilize some of the studies done in chapter two and three for future outlooks and possible implementation of the studies in some useful applications, specifically in smart windows applications. Smart windows are glass panels with dynamically switchable self-tinting features that can change from transparent to partly or completely opaque by controlling the voltage, light, or temperature. Smart windows are attractive and extensively investigated. This is mainly to manufacture and replace conventional windows and provide a more convenient and efficient alternative for all types of windows in different buildings.

LC is an excellent candidate for smart window applications given their sensitivity to weak stimuli and fast switching. They also provide a great guest-host medium and many nanoparticles, such as plasmonic gold nanorods, can be incorporated in the LC medium, allowing for further

control over energy flow of light. This creates a new breed of smart windows. In such case, substantial energy saving aspects will be combined with architectural appeal, affordable costs, and uncompromisable functionality. The key advantage of this approach is that, despite low material and manufacturing costs, it is poised to allow for millisecond switching and separately control of light/energy transmission in the visible and infrared spectral ranges, making these smart windows not only efficient, but also attractive from an architectural perspective. However, for this technology to translate into the market, there are still some challenges to overcome that need to be investigated, which allow for opportunities for further research. Here are a few points that need to be considered in investigating the possibility of bringing smart windows to use. This work requires the help of researchers from different related fields to better understand current drivers that are limiting the development and adoption of smart window technologies. The particular emphasis here is placed on technological development of smart windows technology based on switchable plasmonic nanoparticles, as well as understanding the market drivers and technical limitations on adoption and a thorough analysis of the energy savings.

6.3.1 Relevance and Outcomes

In 2010 for example, according to the U.S. Green Building Council, [11] the buildings sector consumed 40% of the total primary energy use of the United States. And poorly insulated windows can account for 10% to 30% of a buildings energy loss. Smart windows that change light transmission properties of light or heat under the application of voltage is an emerging industry. Nanomaterials combined with LC technology may lead to cheaper and more efficient technology in renewable energy and optoelectronics applications. [12] It is possible to develop novel functional nanomaterials through co-dispersion of plasmonic nanoparticles with pre-engineered optical properties in a LC host medium.

The plasmonic co-dispersion in LC medium is unique because first, the metallic nanoparticles are much more stable compared to organic molecules; secondly, metallic nanoparticles are designed to selectively absorb and scatter specific wavelengths compared to electrochromic and other ap-

proaches, given that the metallic plasmonic nanoparticles are particles with an electron density that can couple with specific wavelengths of electromagnetic radiation leading to strong scattering and absorbance based on the particles' geometries; and lastly, a smart window comprised of co-dispersion of plasmonic nanoparticles in LC host medium can be switched by low-voltage fields and low-intensity light.

Introducing these plasmonic nanoparticles in nematic LC lead to strong polarization-sensitive SPR effects with long-range ordered structure. The nanoparticles can be surface-functionalized by polymer or small molecules to improve their stability and impose surface boundary conditions for orientation of host liquid crystal molecules. [1] Evidentially, co-dispersing plasmonic nanoparticles with anisotropic shapes and different aspect ratios in LC can provide a method to control the transmission of light in these glass panels in both visible or near-infrared range of the light spectrum, either simultaneously or alternatively, which can lead to different states of light transmission, *i.e.* transparent, dark, or translucent. In a transparent state, for example, it is possible to create a composite where more than 90% of visible light can go through the window while it blocks nearly 100% of infrared light. An additional feature can be developed through the use of photo alignment layers on the plasmonic nanoparticles, which can re-orient the nanoparticles in LC by low-intensity light. For example, the smart window can reduce its transparency under the illumination of ambient light of some threshold intensity. Such design will enable composites with tunable properties emerging from combining co-dispersion of anisotropic plasmonic nanoparticles and switchable LC to fabricate glass panels and devices for renewable energy applications.

So far, I have built a successful proof-of-principle demonstration of the plasmonic co-dispersion in LC using cells of about two square inch area, and it is promising for building and testing a one-square-meter smart window prototype. This new breed of smart windows can be developed based on an integral approach of considering the efficiency of energy saving along with the architectural appeal and economic potential. However, there might be some challenges that necessitate establishing new strategies to avoid the potential problems with the deployment of this technology on

a global level. For example, there is a need to check the stability of the nanoparticles in the LC matrix at different or varying temperatures. These smart windows can present the first and only fully-autonomic dynamic window technology that can be remotely controlled and integrated with other high-tech computerized building technologies, which can be controlled in the future using devices like smart phones. This technology is cost efficient, since the dispersing LC medium is a dielectric material and the response is triggered by potential difference of $\sim$ 1V or so, the energy costs needed to power the plasmonic smart windows are negligible. For example, a battery similar to that in an electronic watch would be sufficient to power a square-meter window for a year or so; a small PV cell can be used instead of the battery. The plasmonic smart windows can also eliminate the need for window blinds as well as creating a foundation for new building window architectural designs. Energy consumption is negligible when compared to the anticipated energy savings.

6.3.2 Feasibility

This plasmonic smart window technology would be the only one based on voltage- and light-controlled plasmonic nanoparticles which can provide fast selective control over both visible light and heat-producing IR light, since nobody else so far was able to develop switchable plasmonic nanoparticle co-dispersions. This designed plasmonic co-dispersion can switch between three modes: fully transparent, transparent but blocking IR radiation, and blocking of both visible and IR radiation according to the amount of applied voltage. [1] The tune-ability of this smart window can be controlled from the dark state of $< 1\%$ transmission to clear state of $> 90\%$ transmission while it blocks nearly 95% of IR light.

Globally, implementing these smart windows in buildings could translate into energy savings on the order of \$20 billion per year. They can be manufactured in the form of glass panels of different sizes with simple installation, similar to that of regular windows, for example, and the price can be $\sim$ \$15/ft^2. The LC and plasmonic particles can be encapsulated into polymer films that can be laminated on existing windows, for example, or sandwiched between two glass panels.

Tests to its long-term stability, life time, switching cycles and the efficiency of energy saving should be studied as well. The constituent nanoparticles and the adaptive windows will be designed to dynamically adjusts light transmission through the window across the solar spectrum: automatically transmitting less sunlight during high ambient temperatures to reduce cooling costs while allowing more sunlight to pass during cooler temperatures to assist with heating. A high concentration of switchable plasmonic co-dispersions in LC had been achieved in the lab. The challenge remains in fabricating the large-area smart window, testing the window performance, reliability, and stability under different conditions.

6.3.3 Innovation and Impacts

Current smart window technologies include Thermochromatics, Photochromatics, Electrochromics, Polymer Dispersed Liquid Crystals (PDLC), and Suspended Particle Displays (SPD). However, there are many challenges in this market, including material costs, installation costs, electricity costs and durability, as well as functional features expected from windows, such as the speed of control, possibilities for dimming, and the degree of transparency. Among these technologies, the competing products are based on electrochromic technology. Companies are working on reducing the cost so that they can be competitive and increase their revenues. However, electrochromic windows, as well as all other technologies, have inherent problems. Any small variation in their ability to block infrared radiation can only occur when visible light is also blocked. Also, their switching is nonuniform and cost is much higher than that of \$5-15/ft^2 of regular windows.

It is well known that many old cathedrals have colored windows because of the presence of various gold nanoparticles in the specially prepared glass. Can modern architecture and building design take advantage of nanostructured materials as well to make them not only architecturally appealing but also energy efficient? The preliminary results from Q. Liu *et al* work, [12] for example, indicate the great potential for this when plasmonic nanoparticles are combined with LC technology. And co-dispersing different plasmonic metal nanoparticles with different anisotropic

shapes in LC will result in selective control over both visible light and heat-related infrared electromagnetic radiation.

So far, none of the available smart window technologies are capable of yielding large-area inexpensive smart window designs with safe low-voltage ($\sim$ 1V) switching of light and energy transmission in both visible and infrared spectral ranges, all highly desired features for these applications. The current technologies are lacking selective control over visible light and heat-producing near infrared radiation, and they are costly. All of this suggests that this smart window technology is promising and possible to deploy on a large scale as one of the renewable energy applications, and can be pursued further by other researchers, perhaps becoming the building block of new companies.

6.4 Thesis Summary

Our abilities to harvest, store, and efficiently use and convert energy among different forms highly depends on available materials and their properties. Self-assembly of mesoscale structures composed of nano-sized functional units such as quantum dots and plasmonic metal nanoparticles is an exceptionally promising way of designing artificial composite materials with new macroscopic physical behavior and the properties needed for many energy-related applications. As part of my work, I explored mesoscale self-assembly of anisotropic plasmonic nanoparticles, namely gold nanorods, that are dispersed in responsive liquid crystalline host media. I have also developed a system that controls optical properties of plasmonic nanostructured composites by controlling the alignment of polarized surface plasmon resonance modes of gold nanorods with different shapes co-dispersed within an ordered thermotropic liquid crystal host.

Subsequently, this work was extended further through designing nanostructured composites by co-doping dichroic dyes and anisotropic plasmonic nanoparticles in both nematic and cholesteric liquid crystals. Because these composites exhibit facile and unique switching properties, a function that can control light transmission in the near-infrared and visible spectral ranges, which allows for

the engineering of the physical behavior of self-assembled optical metamaterials and many other possible applications, such as smart and privacy windows, among other possible adaptations of the technology in the market. This can further be enriched and investigated with the assistance of researchers and/or students of different backgrounds, such as engineering, business, architecture, etc, to better study the possibility and minimize the risks and limitations.

In addition, I have established, along with some members of Smalyukh's group, a controlled quantum mechanical effects of a core/shell quantum dots utilizing a coupling effect between the quantum dot and two neighboring plasmonic particles with the assistance of liquid crystal and demonstrated that with reproducible measurements. The technique employed in this work entrenched a platform for the study of plasmonic nanosystems in general, and for the study the plasmonic coupling phenomena. Furthermore, I explored the self-assembly of gold nanorods via entropic forces, namely depletion forces, forming lamellar self-assembled membranes with interesting structures. These self-assembled structures can be useful for a variety of applications in electro-optical and plasmonic devices.

My work will open doors for researchers to further investigate different co-dispersions of different nanoparticles utilizing the properties of liquid crystal to either control the flow of energy and/or manipulate the interaction between these particles. Many examples of different composition of different liquid crystals and nanoparticles were introduced in this chapter. For example, the plasmonic arogels and their possible uses in sensing air or water quality. Alternatively, researchers can investigate the enhancement of the luminescence of up-conversion nanoparticles in the presence of gold nanorods in the liquid crystal medium utilizing the elastic interaction to the advantage of the newly designed composition. This will surely advance new findings in science and contribute to different potential applications.

Overall, this research assists the development of new, tunable nanostructured composites

based on plasmonic nanorods, up-conversion nanoparticles, quantum dots, and many other nanoparticles with unique properties that can be manipulated in dispersions of liquid crystals to provide new, cheaper, and more efficient adaptive technologies, as well as a providing a fertile ground for a new basic science.

6.5 References

[1] Q. Liu and I. I. Smalyukh, "Liquid crystalline cellulose-based nematogels," *SCIENCE ADVANCES*, 2017 **3** 1700981.

[2] Q. Liu, Y. Cui, D. Gardner, X. Li, S. He, and I. I. Smalyukh, "Self-Alignement of Plasmonic Gold Nanorods in Reconfigurable Anisotropic Fluids for Tunable Bulk Metamaterial Applications," *Nano Letters*, 2010 **10** 1347.

[3] A. J. Hess, Q. Liu, and I. I. Smalyukh, "Cellulose-enabled orientationally ordered flexible gels," *US PATENT APP*. 15/868,714 (2018).

[4] Q.-C. Sun, H. Mundoor, J. C. Ribot, V. Singh, I. I. Smalyukh, and P. Nagpal, "Plasmon-enhanced energy transfer for improved upconversion of infrared radiation in doped-lanthanide nanocrystals," *Nano Letters*, 2014 **14** 101.

[5] S. Fischer, F. Hallermann, T. Eichelkraut, G. Plessen, K. W. Krmer, D. Biner, H. Steinkemper, M. Hermle, and J. C. Goldschmidt, "Plasmon enhanced upconversion luminescence near gold nanoparticlessimulation and analysis of the interactions," *Optics Express*, 2012 **20** 271.

[6] H.K. Dan, D.C. Zhou, R.F. Wang, J. Qiao, Z.W. Yang, Z.G. Song, X. Yu, and J.B. Qiu, "Effects of Gold nanoparticles on the enhancement of upconversion and near-infrared emission in Er3+/Yb3+ co-doped transparent glass-ceramics containing BaF2 nanocrystals," *Ceramics International*, 2015 **41** 2648.

[7] X. Liu and D. Y. Lei, "Simultaneous excitation and emission enhancements in upconversion luminescence using plasmonic double-resonant gold nanorods, *Scientific Reports*, 2015 **5** 15235.

[8] F. Wang, Y. Han, C.S.Lim, Y. Lu, J. Wang, J. Xu, H. Chen, C. Zhang, M. Hong, and X. Liu, "Simultaneous phase and size control of upconversion nanocrystals through lanthanide doping," *Nature*, 2010 **463** 1061.

[9] G. Chen, H. Qiu, P. N. Prasad, and X. Chen, "Upconversion Nanoparticles: Design, Nanochemistry, and Applications in Theranostics," *Chemical Reviews*, 2014 **114** 5161.

[10] H. Mundoor, G. H. Sheetah, S. Park, P. J. Ackerman, I. I. Smalyukh, and J. van de Lagemaat, "Tuning and switching a plasmonic quantum dot "sandwich" in a nematic line defect," *ACS NANO*, 2018 **12** 2580.

[11] N. Khanna, J. Romankiewicz, W. Feng, N. Zhou, and Q. Ye, "Comparative policy study for green buildings in U.S. and China," *Lawrence Berkeley National Laboratory*, 2014.

[12] Q. Liu, Y. Yuan, and I. I. Smalyukh. "Electrically and optically tunable plasmonic guest-host liquid crystals with long-range ordered nanoparticles", *Nano Letters*, 2014 **14** 4071.

[13] J. A. De La Cruz, Q. Liu, B. Senyuk, A. W. Frazier, K. Peddireddy, and I. I. Smalyukh, "Cellulose-based reflective liquid crystal films as optical filters and solar gain regulators," *ACS Photonics*, 2018 **5** 2468.

[14] Q. Liu, A. W. Frazier, X. Zhao, J. A. De La Cruz, A. J. Hess, R. Yang, and I. I. Smalyukh, "Flexible transparent aerogels as window retrofitting films and optical elements with tunable birefringence," *Nano Energy*, 2018 **48** 266.

Bibliography

[1] Q. Liu, Y. Yuan, and I. I. Smalyukh, "Electrically and optically tunable plasmotic guest-host liquid crystals with long-range ordered nanoparticles," *Nano Lett.*, 2014 **14** 4071.

[2] Y. Zhang, Q. Liu, H. Mundoor, Y. Yuan, and I. I. Smalyukh, "Metal nanoparticle dispersion, alignment and assembly in nematic liquid crystals for applications in switchable plasmonic color filters and E-polarizers," *ACS Nano*, 2015 **9** 3097.

[3] H. Mundoor, B. Senyuk, and I. I. Smalyukh, "Triclinic nematic colloidal crystals from competing elastic and electrostatic interactions," *Science*, 2016 **352** 69.

[4] O. Lehmann, "Die Struktur krystallinischer Flssigkeiten," *Zeitschrift für Physikalische Chemie*, 1889 **4** 462.

[5] Q. Liu, Y. Cui, D. Gardner, X. Li, S. He, and I. I. Smalyukh. "Self-alignment of plasmonic gold nanorods in reconfigurable anisotropic fluids for tunable bulk metamaterial applications," *Nano Lett.*, 2010 **10** 1347.

[6] Y. Yuan and I. I. Smalyukh, "Topological nanocolloids with facile electric switching of plasmonic properties," *Opt. Lett.*, 2015 **40** 5630.

[7] G. H. Sheetah, Q. Liu, and I. I. Smalyukh, "Self-assembly of predesigned optical materials in nematic codispersions of plasmonic nanorods," *Optics Letters*, 2016 **41** 4899.

[8] G. H. Sheetah, Q. Liu, B. Senyuk, B. Fleury, and I. I. Smalyukh, "Electric switching of visible and infrared transmission using liquid crystals co-doped with plasmonic gold nanorods and dichroic dyes," *Optics Express*. 2018 **26** 22264.

[9] H. Mundoor, G. H. Sheetah, S. Park, P. J. Ackerman, I. I. Smalyukh, and J. van de Lagemaat, "Tuning and switching a plasmonic quantum dot "sandwich" in a nematic line defect," *ACS NANO*, 2018 **12** 2580.

[10] A. Bhattacharyya, "Fluorescence labelling of biologically important molecules," *Ind. J. Biochem. Biophys.*, 1986 **23** 171.

[11] D. Demus, J. Good, G. W. Gray, H.W. Spiess, and V. Vill, "Handbook of Liquid Crystal Sets," *WILEYVCH Verlag GmbH*, 1998.

[12] K. G. Thomas, S. Barazzouk, B. I. Binil Itty Ipe, S.T.S. Joseph, and P. V. Kamat, "Uniaxial plasmon coupling through longitudinal self-assembly of gold nanorods," *J. Phys. Chem. B*, 2004 **108** 13066.

[13] P. K. Jain, S. Eustis, and M. A. El-Sayed, "Plasmon coupling in nanorod assemblies: optical absorption, discrete dipole approximation simulation, and exciton-coupling model," *J. Phys. Chem. B* 2006 **110** 18243.

[14] F. Wang, Y. Han, C.S. Lim, Y. Lu, J. Wang, J. Xu, H. Chen, C. Zhang, M. Hong, and X. F. Liu, "Simultaneous phase and size control of upconversion nanocrystals through lanthanide doping," *Nature*, 2010 **463** 1061.

[15] X. Ye, C. Zheng, J. Chen, Y. Gao, and C.B. Murray, " Using binary surfactant mixtures to simultaneously improve the dimensional tunability and monodispersity in the seeded growth of gold nanorods," *Nano Lett.*, 2013 **13** 765.

[16] L. Wang, "Controlled synthesis and luminescence of lanthanide doped NaYF4 nanocrystals," *Chem. Mater.*, 2007 **19** 727.

[17] W. C. Wu and J. B. Tracy, "Large-scale silica overcoating of gold nanorods with tunable shell thicknesses," *Chem. Mater*, 2015 **27** 2888.

[18] S. Link, Z. L. Wang, and M. A. El-Sayed, "Alloy formation of goldsilver nanoparticles and the dependence of the plasmon absorption on their composition," *J. Phys. Chem. B*, 1999 **103** 3529.

[19] H. K. Bisoy and S. Kumar, "Liquid-crystal nanoscience: An emerging avenue of soft self-assembly," *Chem. Soc. Rev.*, 2011 **40** 306.

[20] B. Senyuk, D. Glugla, and I. I. Smalyukh, "Rotational and translational diffusion of anisotropic gold nanoparticles in liquid crystals controlled by varying surface anchoring," *Phys. Rev. E*, 2013 **88** 062507.

[21] B. Bahadur, "Handbook of Liquid Crystals," *Wiley-VCH*, Weinheim, 2A, 1998.

[22] P. M. Chaikin, and T. C. Lubensky, "Principles of condensed matter physics," *Cambridge Univ. Press*, 2000.

[23] L. M. Blinov, and V. G. Chigrinov, "Electrooptic effects in liquid crystal materials," *Springer-Verlag, New York*, 1996.

[24] M. Bass, C. DeCusatis, J. M. Enoch, V. Lakshminarayanan, G. Li, C. MacDonald, V. N. Mahajan, and E. Van Stryland, "Handbook of Optics", *McGraw-Hill, New York*, 1995.

[25] F. C. Frank, "On the Theory of Liquid Crystals," *Discussions of the Faraday. Society,* 1958 **25** 19.

[26] J. Li, C. H. Wen, S. Gauza, R. Lu, and S. T. Wu, "Refractive indices of liquid crystals for display applications," *J. D On the Theory of Liquid Crystals isp. Technol.*, 2005 **1** 51.

[27] S. Ishihara, "How far has the molecular alignment of liquid crystals been elucidated?," *IEEE/OSA Journal of Display Technology,*, 2005 **1** 30.

[28] V. S. U. Fazio, L. Komitov, C. Radüge, S. Lagerwal, and H. Motshmann, " Influence of the flow on the anchoring of nematic liquid crystals on Langmuir-Blodgett monolayers studied by optical second-harmonic generation," *Eur. Phys. J. E*, 2001 **5** 309.

[29] A. M. Funston, C. Novo, T. J. Davis, and P. Mulvaney, "Plasmon coupling of gold nanorods at short distances and in different geometries," *Nano Lett.*, 2009 **9** 1651.

[30] L.S. Slaughter, W.-S. Chang, P. Swanglap, A. Tcherniak, B. P. Khanal, E. R. Zubarev, and S. J. Link, "Single-particle spectroscopy of gold nanorods beyond the quasi-static limit: Varying the width at constant aspect ratio," *Phys. Chem. C*, 2010 **114** 4934.

[31] A. S. Stender, G. Wang, W. Sun, and N. Fang, "Influence of gold nanorod geometry on optical response," *ACS Nano*, 2010 **4** 7667.

[32] P.K. Jain and M. A. El-Sayed, "Surface plasmon coupling and its universal size scaling in metal nanostructures of complex geometry: Elongated particle pairs and nanosphere trimers," *J. Phys. Chem. C*, 2008 **112** 4954.

[33] B. T. Draine and P. J. Flatau, "Discrete-dipole approximation for scattering calculations," *J. Opt. Soc. Am. A*, 1994 **11** 1491.

[34] B. Nikoobakht and M. A. El-Sayed, "Preparation and growth mechanism of gold nanorods (NRs) using seed-mediated growth method," *Chem. Mater*, 2003 **15** 1957.

[35] N. R. Jana , L. Gearheart , and C. J. Murphy, "Seed-mediated growth approach for shapecontrolled synthesis of spheroidal and rodlike gold nanoparticles using a surfactant template," *Adv. Mater.*, 2001 **13** 1389.

[36] T. K. Sau and C. J. Murphy, "Seeded high yield synthesis of short Au nanorods in aqueous solution," *Langmuir*, 2004 **20** 6414.

[37] J. O. Park, S.-H. Cho, D.-Y Jeong, Y.-M Kong, and S. Y. Lee, "Effects of chloride and silver ions on gold nanorod formation," *Jpn. J. Appl. Phys.*, 2015 **54** 019202.

[38] J. Cheng, L. Ge, B. Xiong, and Y. He, "Investigation of pH effect on gold nanorod synthesis," *Journal of the Chinese Chemical Society*, 2011 **58** 822.

[39] H. Groenbeck, A. Curioni, and W. Andreoni, "Thiols and disulfides on the Au(111) surface: The headgroup-gold interaction," *J Am Chem Soc*, 2000 **122** 3839.

[40] L. Vigderman, and E.R. Zubarev, "High-yield synthesis of gold nanorods with longitudinal SPR peak greater than 1200 nm using hydroquinone as a reducing agent," *Chem. Mater.*, 2013 **25** 1450.

[41] P. K. Jain, W. Huang, and M.A. El-Sayed, "On the universal scaling behavior of the distance decay of plasmon coupling in metal nanoparticle pairs: A plasmon ruler equation prashant," *Nano Lett.*, 2007 **7** 2080.

[42] H. Zhang, J. Zhang, X. Tong, D. Ma, and Y. Zhao, "Light polarizationcontrolled shapememory polymer/gold nanorod composite," *Macromolecular rapid communications*, 2013 **34** 1575.

[43] A.J. Haes, D.A. Stuart, S. Nie, and R.P. Van Duyne, "Using solution-phase nanoparticles, surface-confined nanoparticle arrays and single nanoparticles as biological sensing platforms", *J. Fluoresc.*, 2004 **14** 355.

[44] J. Perez-Juste, L. M. Liz-Marzan, S. Carnie, D. Y. C. Chan, and P. Mulvaney, "Electric-field-directed growth of gold nanorods in aqueous surfactant solutions," *Adv. Funct. Mater.*, 2004 **14** 571.

[45] X. Ye, L. Jin, H. Caglayan, J. Chen, G. Xing, C. Zheng, V. Doan-Nguyen, Y. Kang, N. Engheta, C. R. Kagan, and C. B. Murray, "Improved size-tunable synthesis of monodisperse gold nanorods through the use of aromatic additives," *ACS Nano*, 2012 **6** 2804.

[46] J. A. Fan, C. Wu, K. Bao, J. Bao, R. Bardhan, N. J. Halas, V. N. Manoharan, P. Nordlander, G. Shvets, and F. Capasso, "Self-assembled plasmonic nanoparticle clusters," *Science*, 2010 **328** 1135.

[47] M. R. Jones, R. J. Macfarlane, B. Lee, J. Zhang, K. L. Young, A. J. Senesi, and C. A. Mirkin, "DNA-nanoparticle superlattices formed from anisotropic building blocks," *Nat. Mater*, 2010 **9** 913.

[48] T. Hu, B. P. Isaacof, J. H. Bahng, C. Hao, Y. Zhou, J. Zhu, X. Li, Z. Wang, S. Liu, C. Xu, J. S. Biteen, and N. A. Kotov, "Self-organization of plasmonic and excitonic nanoparticles into resonant chiral supraparticle assemblies," *Nano Lett.*, 2014 **14** 6799.

[49] G. H. Heilmeier, and L. A. Zanoni, "Guesthost interactions in nematic liquid crystals. A new electrooptic effect," *Appl. Phys. Lett.*, 1968 **13** 91.

[50] T. Uchida, H. Seki, C. Shishido, and M. Wada, "Bright dichroic guest-host LCDs without a polarizer," *Proc. Soc. Inf. Disp.*, 1981 **22** 41.

[51] B. Taheri, T. Kosa, V. Bodnar, L. Sukhomlinova, L. Su, C. Martincic, J. Chonko, and E.-Y. Park, "Guest-host liquid crystal devices for adaptive window application," *Proc. SPIE Emerging Liquid Crystal Technologies V*, 2010 **7618**.

[52] L. Jiang, H. Mundoor, Q. Liu, and I. I. Smalyukh, "Electric switching of fluorescence decay in gold-silica-dye nematic nanocolloids mediated by surface plasmons," *ACS Nano*, 2016 **10** 7064.

[53] D. F. Gardner, J. S. Evans, and I. I. Smalyukh, "Towards reconfigurable optical metamaterials: Colloidal nanoparticle self-assembly and self-alignment in liquid crystals," *Mol. Cryst. Liq. Cryst.*, 2011 **545** 1227.

[54] I. I. Smalyukh, B. I. Senyuk, P. Palffy-Muhoray, O. D. Lavrentovich, H. Huang, E. C. Gartland, Jr., V. H. Bodnar, T. Kosa, and B. Taheri, "Electric-field-induced nematic-cholesteric transition and three-dimensional director structures in homeotropic cells," *Phys. Rev. E*, 2005 **72** 061707.

[55] K. A. Crandall, M. R. Fisch, R. G. Petschek, and C. Rosenblatt, "Vanishing Freedericksz transition threshold voltage in a chiral nematic liquid crystal," *Appl. Phys. Lett.*, 1994 **64** 1741.

[56] R. Baetens, B. P. Jelle, and A. Gustavsen, "Properties, requirements and possibilities of smart windows for dynamic daylight and solar energy control in buildings: A state-of-the-art review," *Sol. Energy Mater. Sol. Cells*, 2010 **94** 87.

[57] E. L. Runnerstrom, A.Llordés, S. D. Lounis, and D. J. Milliron, "Nanostructured electrochromic smart windows: Traditional materials and NIR-selective plasmonic nanocrystals," *Chem. Commun.*, 2014 **50** 10555.

[58] I. Sage, "Thermochromic iquid crystals," *Liq. Cryst.*, 2011 **38** 1551.

[59] J. Heo, J.-W. Huh, and T.-H. Yoon, " Fast-switching initially -transparent liquid crystal light shutter with crossed patterned electrodes," *AIP Adv.*, 2015 **5** 047118.

[60] H. Ren and S.-T. Wu, "Anisotropic liquid crystal gels for switchable polarizers and displays," *Appl. Phys. Lett.*, 2002 **81** 1432.

[61] Y.-C. Hsiao, K.-C. Huang, and W. Lee, "Photo-switchable chiral liquid crystal with optical tristability enabled by a photoresponsive azo-chiral dopant," *Opt. Express*, 2017 **25** 2687.

[62] S. Dey, and J. Zhao, "Plasmonic effect on exciton and multiexciton emission of single quantum dots," *J. Phys. Chem. Lett.*, 2016 **7** 2921.

[63] C. Livache, E. Izquierdo, B. Martinez, M. Dufour, D. Pierucci, S. Keuleyan, H. Cruguel, L. Becerra, J. L. Fave, H. Aubin, A. Ouerghi, E. Lacaze, M. G. Silly, B. Dubertret, S. Ithurria, and E. Lhuillier, "Charge dynamics and optolectronic properties in HgTe colloidal quantum wells," *Nano Lett.* 2017 **17** 4067.

[64] J. C. Johnson, T. H. Reilly, A. C. Kanarr, and J. van de Lagemaat, "The ultrafast photophysics of pentacene coupled to surface plasmon active nanohole films," *J. Phys. Chem. C*, 2009 **113** 6871.

[65] B. Ji, E. Giovanelli, B. Habert, P. Spinicelli, M. Nasilowski, X. Xu, N. Lequeux, J. Hugonin, F. Marquier, J. Greffet, and B. Dubertret, "Non-blinking quantum dot with a plasmonic nanoshell resonator," *Nat. Nanotechnol.*, 2015 **10** 170.

[66] D. E. Gómez, K. C. Vernon, P. Mulvaney, and T. J. Davis, "Surface plasmon mediated strong excitonphoton coupling in semiconductor nanocrystals," *Nano Lett.* 2010 **10** 274.

[67] P.J. Ackerman, H. Mundoor, I. I. Smalyukh, and J. van de Lagemaat, "Plasmon-exciton interactions probed using spatial coentrapment of nanoparticles by topological singularities," *ACS Nano*, 2015 **9** 12392.

[68] S. J. LeBlanc, M. R. McClanahan, M. Jones, and P. J. Moyer, "Enhancement of multiphoton emission from single CdSe quantum dots coupled to gold films," *Nano Lett.* 2013 **13** 1662.

[69] S. Masuo, K. Kanetaka, R. Sato, and T. Teranishi, "Direct observation of multiphoton emission enhancement from a single quantum dot using AFM manipulation of a cubic gold nanoparticle," *ACS Photonics*, 2016 **3** 109.

[70] Y.-S. Park, Y. Ghosh, Y. Chen, A. Piryatinski, P. Xu, N. H. Mack, H.-L. Wang, V. I. Klimov, J. A. Hollingsworth, and H. Htoon, "Super-poissonian statistics of photon emission from single CdSe-CdS core-shell nanocrystals coupled to metal nanostructures," *Phys. Rev. Lett.*, 2013 **110** 117401.

[71] S. Dey, Y. Zhou, X. Tian, J. A. Jenkins, O. Chen, S. Zou, and J. Zhao, "An experimental and theoretical mechanistic study of biexciton quantum yield enhancement in single quantum dots near gold nanoparticles," *Nanoscale*, 2015 **7** 6851.

[72] H. Naiki, S. Masuo, S. Machida, and A. Itaya, "Single-photon emission behavior of isolated CdSe/ZnS quantum dots interacting with the localized surface plasmon resonance of silver nanoparticles," *J. Phys. Chem. C.*, 2011 **115** 23299.

[73] K. Matsuzaki, S. Vassant, H. W. Liu, A. Dutschke, B. Hoffmann, X. Chen, S. Christiansen, M. R. Buck, J. A. Hollingsworth, S. Gtzinger, and V. Sandoghdar, "Strong plasmonic enhancement of biexciton emission: Controlled coupling of a single quantum dot to a gold nanocone antenna," *Sci. Rep.*, 2017 **7** 42307.

[74] P. K. Jain, D. Ghosh, R. Baer, E. Rabani, and P. A. Alivisatos, "Near-field manipulation of spectroscopic selection rules on the nanoscale," *Proc. Natl. Acad. Sci. U.S.A.*, 2012 **109** 8016.

[75] M. L. Andersen, S. Stobbe, A. S. Sorensen, and P. Lodahl, "Strongly modified plasmon-matter interaction with mesoscopic quantum emitters," *Nat. Phys.*, 2011 **7** 215.

[76] P. Zijlstra, P. M. R. Paulo, and M. Orrit, "Optical detection of single non-absorbing molecules using the surface plasmon resonance of a gold nanorod," *Nat. Nanotechnol.*, 2012 **7** 379.

[77] V. G. Kravets, F. Schedin, R. Jalil, L. Britnell, R. V. Gorbachev, D. Ansell, B. Thackray, K. S. Novoselov, A. K. Geim, A. V. Kabashin, and A. N. Grigorenko, "Singular phase nano-optics in plasmonic metamaterials for label-free single-molecule detection," *Nat. Mater.*, 2013 **12** 304.

[78] L. Rogobete, F. Kaminski, M. Agio, and V. Sandoghdar, "Design of plasmonic nanoantennae for enhancing spontaneous emission," *Opt. Lett.*, 2007 **32** 1623.

[79] Qi-C. Sun, H. Mundoor, J. C. Ribot, V. Singh, I. I. Smalyukh, and P. Nagpal, "Plasmon-enhanced energy transfer for improved upconversion of infrared radiation in doped-lanthanide nanocrystals," *Nano Lett.*, 2014 **14** 101.

[80] W. R. Erwin, H. F. Zarick, E. M. Talbert, and R. Bardhan, "Light trapping in mesoporous solar cells with plasmonic nanostructures," *Energy Environ. Sci.*, 2016 **9** 1577.

[81] H. A. Atwater and A. Polman, "Plasmonics for improved photovoltaic devices," *Nat. Mater.*, 2010 **9** 205.

[82] A. J. Morfa, K. L. Rowlen, T. H. Reilly, M. J. Romero, and J. van de Lagemaat, "Plasmon-enhanced solar energy conversion in organic bulk heterojunction photovoltaics," *Appl. Phys. Lett.*, 2008 **92** 013504.

[83] K. Wu, J. Chen, J. R. McBride, and T. Lian, "Charge transfer. Efficient hot-electron transfer by a plasmon-induced interfacial charge-transfer transition," *Science*, 2015 **349** 632.

[84] I. Thomann, B. A. Pinaud, Z. Chen, B. M. Clemens, T. F. Jaramillo, and M. L. Brongersma, "Plasmon enhanced solar-to-fuel energy conversion," *Nano Lett.*, 2011 **11** 3440.

[85] P. J. Ackerman and I. I. Smalyukh, "Diversity of knot solitons in liquid crystals manifested by linking of preimages in torons and hopfions," *Phys Rev X*, 2017 **7** 011006.

[86] P. G. de Gennes, and J. Prost, "The Physics of Liquid Crystals," *2nd ed. Clarendon*, 1993.

[87] X. Wang, D.S. Miller, E. Bukusoglu, J. J. de Pablo, and N. L. Abbott, "Topological Defects in liquid crystals as templates for molecular self-assembly," *Nat. Mater.*, 2016 **15** 106.

[88] M. Ravnik, and S. Zumer, "Landau-De Gennes modelling of nematic liquid crystal colloids," *Liq. Cryst.*, 2009 **36** 1201.

[89] A. Ashkin, J. M. Dziedzic, J. E. Bjorkholm, and S. Chu, "Observation of a single-beam gradient force optical trap for dielectric particles," *Opt. Lett.*, 1986 **11** 288.

[90] O. M. Marag, P. H. Jones, P. G. Gucciardi, G. Volpe, and A. C. Ferrari, "Optical trapping and manipulation of nanostructures," *Nat. Nanotechnol.*, 2013 **8** 807.

[91] A. Kyrsting, P. M.Bendix, D. G. Stamou, and L. B. Oddershede, "Heat profiling of three-dimensionally optically trapped gold nanoparticles using vesicle cargo release," *Nano Lett.*, 2011 **11** 888.

[92] B. Senyuk, J. S. Evans, P. J. Ackerman, T. Lee, P. Manna, L. Vigderman, E. R. Zubarev, J. van de Lagemaat, and I. I. Smalyukh, "Shape-dependent oriented trapping and scaffolding of plasmonic nanoparticles by topological defects for self-assembly of colloidal dimers in liquid crystals," *Nano Lett.*, 2012 **12** 955.

[93] H. Mundoor, T. Lee, D. G. Gann, P. J. Ackerman, B. Senyuk, J. van de Lagemaat, and I. I. Smalyukh, "Optically and elastically assembled plasmonic nanoantennae for spatially resolved characterization of chemical composition in soft matter systems using surface enhanced spontaneous and stimulated raman scattering," *J. Appl. Phys.*, 2014, **116**, 063511.

[94] F. Hajizadeh, and S. N. S. Reihani, "Optimized optical trapping of gold nanoparticles," *Opt. Express*, 2010 **18** 551.

[95] P. M. Hansen, V. K. Bhatia, N. Harrit, and L. Oddershede, "Expanding the optical trapping range of gold nanoparticles," *Nano Lett.*, 2005 **5** 1937.

[96] J. S. Evans, Y. Sun, B. Senyuk, P. Keller, V. M. Pergamenshchik, T. Lee, and I. I. Smalyukh, "Active Shape-morphing elastomeric colloids in short-pitch cholesteric liquid crystals," *Phys. Rev. Lett.*, 2013 **110** 187802.

[97] P. Poulin, H. Stark, T. C. Lubensky, and D. A. Weitz, "Novel colloidal interactions in anisotropic fluids," *Science*, 1997 **275** 1770.

[98] J. Gargiulo, I. L. Violi, S. Cerrota, L. Chvátal, E. Cortés, E. M. Perassi, F. Diaz, P. Zemnek, and F. D. Stefani, "Accuracy and mechanistic details of optical printing of single Au and Ag nanoparticles," *ACS Nano*, 2017 **11** 9678.

[99] P. K. Jain, S. Eustis, and M. A. El-Sayed, "Plasmon coupling in nanorod assemblies: Optical absorption, discrete dipole approximation simulation, and exciton-coupling model," *J. Phys. Chem. B*, 2006 **110** 18243.

[100] B. T. Draine, and P. J. Flatau, "Discrete-dipole approximation for periodic targets: Theory and tests," *J. Opt. Soc. Am. A*, 2008 **25** 2593.

[101] P. J. Flatau, and B. T. Draine, "Fast near field calculations in the discrete dipole approximation for regular rectilinear grids," *Optics Express*, 2012 **20** 1247.

[102] P. K. Jain, N. Sobh, J. Smith, A. R. N. Sobh, S. White, J. Faucheaux, and J. Feser, "nanoDDSCAT," https://nanohub.org/resources/dda. 2015, DOI: 10.4231/D32V2CB3M.

[103] S. C. Kitson, P. Jonsson, J. G. Rarity, and P. R. Tapster, "Intensity fluctuation spectroscopy of small numbers of dye molecules in a microcavity," *Phys. Rev. A*, 1998 **58** 620.

[104] C. W. Hollars, S. M. Lane, and T. Huser, "Controlled non-classical photon emission from single conjugated polymer molecules," *Chem. Phys. Lett.*, 2003 **370** 393.

[105] C. Santori, M. Pelton, G. Solomon, Y. Dale, and Y. Yamamoto, "Triggered single photons from a quantum dot," *Phys. Phys. Rev. Lett.*, 2001 **86** 1502.

[106] B. Omogo, J. F. Aldana, and C. D. Heyes, "Radiative and non-radiative lifetime engineering of quantum dots in multiple solvents by surface atom stoichiometry and ligands," *J. Phys. Chem. C*, 2013 **117** 2317.

[107] A. G. Curto, G. Volpe, T. H. Taminiau, M. P. Kreuzer, R. Quidant1, and N. F. van Hulst, "Unidirectional emission of a quantum dot coupled to a nanoantenna," *Science*, 2010 **329** 930.

[108] S. Arena, F. Cucinotta, O. Di Stefano, A. Cacciola, R. Saija, and S. Savasta, "Plasmonic absorption enhancement of a single quantum dot," *Plasmonics*, 2015 **10** 955.

[109] B. Patton, W. Langbein, and U. Woggon, "Trion, biexciton, and exciton dynamics in single self-assembled CdSe quantum dots," *Phys. Rev. B*, 2003 **68** 125316.

[110] Y. -S. Park, A. V. Malko, J. Vela, Y. Chen, Y. Ghosh, F. Garcia-Santamaria, J. A. Hollingsworth, V. I. Klimov,and H. Htoon, "Near-unity quantum yields of biexciton emission from CdSe/CdS nanocrystals measured using single-particle spectroscopy," *Phys. Rev. Lett.*, 2011 **106** 187401.

[111] S. Jana, P. Davidson, and B. Abécassis, "CdSe nanoplatelets: Living polymers," *Angew. Chem. Int. Ed.*, 2016 **55** 9371.

[112] S. Gai, C. Li, P. Yang, and J. Lin, "Recent Progress in rare earth micro/ nanocrystals: Soft chemical synthesis, luminescent properties, and biomedical applications," *Chem. Rev.*, 2014 **114** 2343.

[113] M. C. M. Varney, Q. Zhang, B. Senyuk, and I. I. Smalyukh, "Self-assembly of colloidal particles in deformation landscapes of electrically driven layer undulations in cholesteric liquid crystals," *Phys. Rev. E*, 2016 **94** 042709.

[114] P. B. Johnson and R. W. Christy, "Optical constants of the noble metals," *Phys. Rev. B*, 1972 **6** 4370.

[115] S. Ninomiya and S. Adachi, "Optical properties of cubic and hexagonal CdSe," *J. Appl. Phys.*, 1995 **78** 4681.

[116] S. Ozaki and S. Adachi, "Optical constants of cubic ZnS," *Jpn. J. Appl. Phys.*, 1993 **32** 5008.

[117] G. Abbate, V. Tkachenko, A. Marino, F. Vita, M. Giocondo, A. Mazzulla, and L. De Stefano, "Optical characterization of liquid crystals by combined ellipsometry and half-leaky-guided-mode spectroscopy in the visible-near infrared range," *J. Appl. Phys.*, 2007 **101** 073105.

[118] L. Vigderman, B. P. Khanal, and E. R. Zubarev, "Functional gold nanorods: Synthesis, self-assembly, and sensing applications," '*Advanced Materials*, 2012 **24** 4811.

[119] F. Li, D. P. Josephson, and A. Stein, "Colloidal assembly: The road from particles to colloidal molecules and crystals," *Angewandte Chemie International Edition*, 2011 **50** 360.

[120] D. A. Walker, B. Kowalczyk, M. O. de la Cruz, and B. A. Grzybowski, "Electrostatics at the nanoscale," *Nanoscale*, 2011, **3**, 1316.

[121] Q. Liu, M. G. Campbell, J. S. Evans, and I. I. Smalyukh, "Orientationally ordered colloidal co-dispersions of gold nanorods and cellulose nanocrystals," *Advanced Materials*, 2014 **26** 7178.

[122] Q. Liu, B. Senyuk, J. Tang, T. Lee, J. Qian, S. He, and I. I. Smalyukh, "Plasmonic complex fluids of nematic-like and helicoidal self-assemblies of gold nanorods with negative order parameter," *Physical Review Letters*, 2012 **109** 088301.

[123] Y. Xie, Y. Liang, D. Chen, X. Wu, L. Dai, and Q. Liu, "Vortical superlattices in a gold nanorods' self-assembled monolayer." *Nanoscale*, 2014 **6** 3064.

[124] D. V. Talapin, E. V. Shevchenko, C. B. Murray, A. Kornowski, S. Förster, and H. Weller, "CdSe and CdSe/CdS nanorod solids," *Journal of the American Chemical Society*, 2004 **126** 12984.

[125] L. S. Li, and A. P. Alivisatos, "Origin and scaling of the permanent dipole moment in CdSe nanorods," *Advanced Materials*, 2003 **15** 408.

[126] M. Ozawa, H. Goto, M. Kusunoki, and E. Osawa, "Continuously growing spiral carbon nanoparticles as the intermediates in the formation of fullerenes and nanoonions," *The Journal of Physical Chemistry B*, 2002 **106** 7135.

[127] F. Kim, S. Kwan, J. Akana, and P. Yang, "Langmuir-Blodgett nanorod assembly," *Journal of the American Chemical Society*, 2001 **123** 4360.

[128] L. Kang, T. Gibaud, Z. Dogic, and T. C. Lubensky, "Entropic forces stabilize diverse emergent structures in colloidal membranes," *Soft Matter*, 2016 **12** 386.

[129] L.-s. Li, J. Walda, L. Manna, and A. P. Alivisatos, "Semiconductor nanorod liquid crystals," *Nano Letters*, 2002 **2** 557.

[130] M.-T. F. Rodrigues, P. M. Ajayan, and G. G. Silva, "Fast vortex-assisted self-assembly of carbon nanoparticles on an air-water Interface," *The Journal of Physical Chemistry B*, 2013 **117** 6524.

[131] J. A. De La Cruz, Q. Liu, B. Senyuk, A. W. Frazier, K. Peddireddy, and I. I. Smalyukh, "Cellulose-based reflective liquid crystal films as optical filters and solar gain regulators," *ACS Photonics*, 2018 **5** 2468.

[132] Q. Liu, A. W. Frazier, X. Zhao, J. A. De La Cruz, A. J. Hess, R. Yang, and I. I. Smalyukh, "Flexible transparent aerogels as window retrofitting films and optical elements with tunable birefringence," *Nano Energy*, 2018 **48** 266.

[FKhanna] . Khanna, J. Romankiewicz, W. Feng, N. Zhou, and Q. Ye, "Comparative policy study for green buildings in U.S. and China," *Lawrence Berkeley National Laboratory*, 2014.

[133] A. J. Hess, Q. Liu, and I. I. Smalyukh, "Cellulose-enabled orientationally ordered flexible gels," *US PATENT APP.* 15/868,714 (2018).

[134] S. Fischer, F. Hallermann, T. Eichelkraut, G. Plessen, K. W. Krmer, D. Biner, H. Steinkemper, M. Hermle, and J. C. Goldschmidt, "Plasmon enhanced upconversion luminescence near gold nanoparticles-simulation and analysis of the interactions," *Optics Express*, 2012 **20** 271.

[135] H. K. Dan, D. C. Zhou, R. F. Wang, J. Qiao, Z. W. Yang, Z. G. Song, X. Yu, and J. B. Qiu, "Effects of Gold nanoparticles on the enhancement of upconversion and near-infrared emission in Er3+/Yb3+ co-doped transparent glass-ceramics containing BaF2 nanocrystals," *Ceramics International*, 2015 **41** 2648.

[136] G. Chen, H. Qiu, P. N. Prasad, and X. Chen, "Upconversion Nanoparticles: Design, nanochemistry, and applications in theranostics," *Chemical Reviews*, 2014 **114** 5161.

Appendix A

Supporting material to Chapter 4

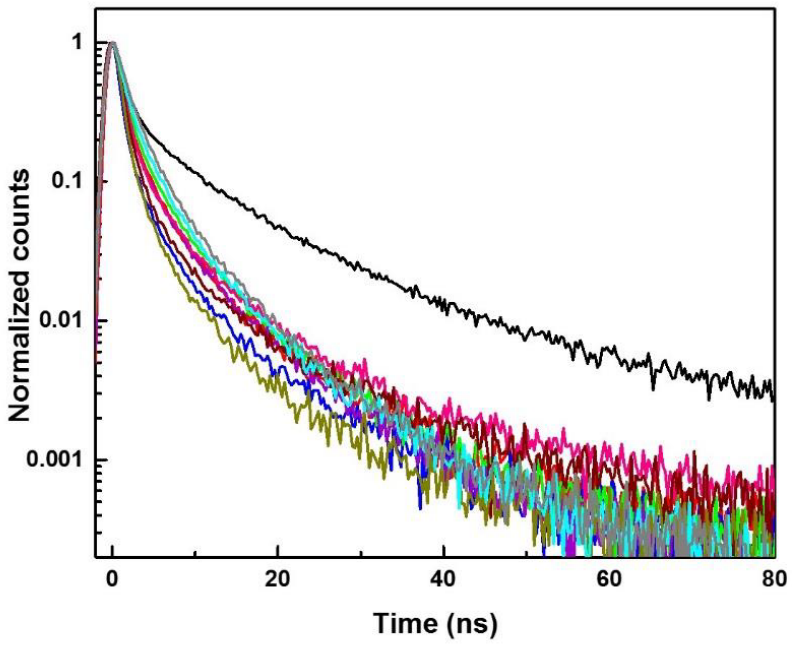

Fig. A.1: Fluorescence decay curves of a QD particle trapped inside the line defect (black) and a QD particle sandwiched between two GNRs forming a dimer structure based on multiple measurements on GNR-QD assemblies (colored). Black curve represents a typical decay curve for a QD particle without GNR.

	τ_1 (ns)	τ_2 (ns)
QD	1.17	19.88
QD-Au	1.09	5.32
	1.06	6.55
	1.1	4.58
	1.2	5.78
	0.97	4.84
	1.2	6.5
	0.98	4.92
	1.2	5.33
	1.08	6.3
	0.95	6.35

Table A.1: The lifetime values extracted by fitting a double exponential equation to the fluorescence decay curves presented in Figure S1 above.

A.1 Estimation of surface temperature of GNR particle during laser tweezer manipulation

Approximate estimate of the increase in temperature at the surface of silica layer of the GNR particles when manipulated with a laser trap can be calculated by the equation:

$$\Delta T_S = \frac{\Phi r^3}{3\lambda h}, \tag{A.1}$$

Where r is the radius of the gold core of GNR particles, h is the radius of the silica coated particle, and λ is the thermal conductivity of silica. $\Phi = \eta\sigma/V$ is the heat absorbed by the particle per unit volume, where η is the incident laser intensity, σ is the absorption cross section of the

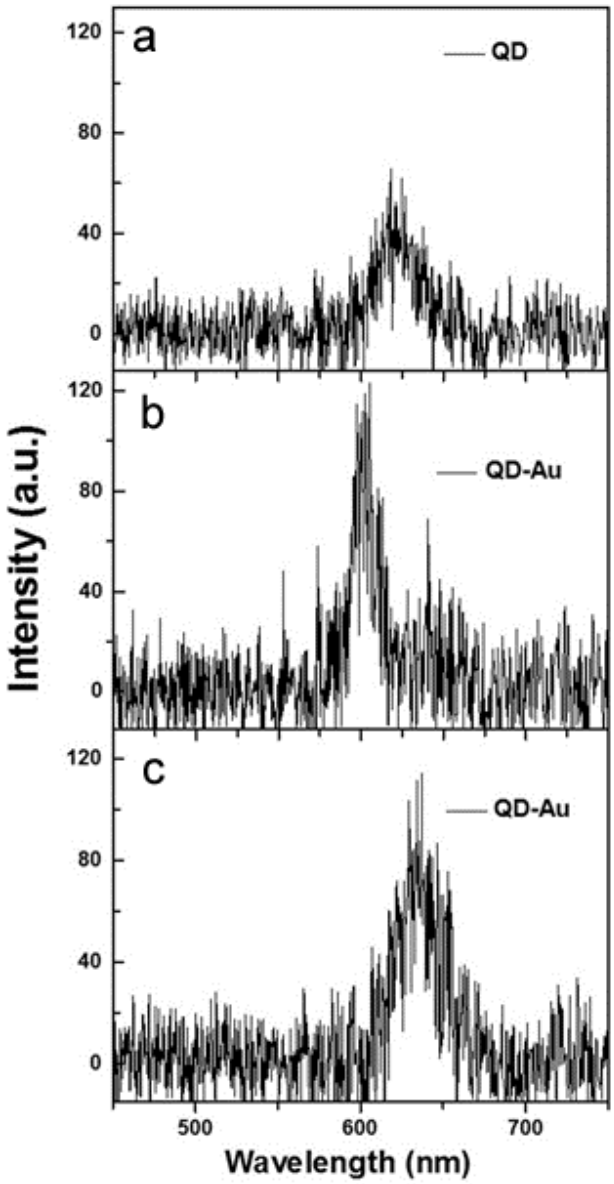

Fig. A.2: Fluorescence spectra of a single QD in line defect without GNR (a) and with GNRs showing a blueshifted (b) and redshifted (c) spectra.

particle at 1064 nm and V is the volume of the particle. For 7 mW laser power, the temperature increase at the surface of the silica layer of the GNR particles is estimated to be $\sim 2\ ^{\circ}\mathrm{C}$.

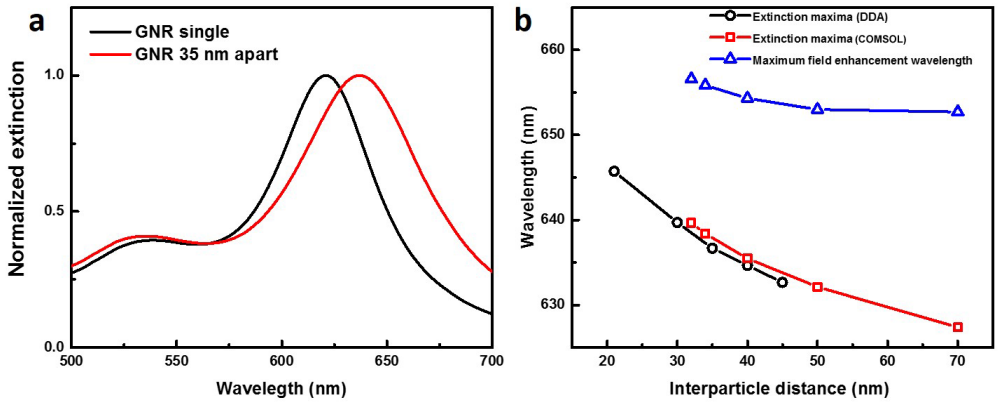

Fig. A.3: Simulated extinction spectra of a single GNR particle (black curve) and two GNR particles forming a sandwich structure (red curve) in the LC line defect. (b) Plot of LSPR peak positions vs. end-to-end separation between the gold cores of two GNRs located in the LC line defect calculated based on DDA (○) and COMSOL Multiphysics (□). Variations of maximum electric field enhancement wavelength (△) end-to-end separation between the gold cores of two GNRs in the sandwich structure, calculated based on the electromagnetic simulations using COMSOL Multiphysics.

A.2 Estimation of van der Waals attraction between the GNRs in LC defect

The total interaction potential between two GNRs in line defect can be represented as sum of pair potential u_{el} due to the repulsive elastic and u_{vdW} due to the attractive van der Waals interaction potential.

$$u(r_{\mathrm{cc}}) = u_{\mathrm{el}}(r_{\mathrm{cc}}) + u_{\mathrm{vdW}}(r_{\mathrm{cc}}). \tag{A.2}$$

The van der Waals potential between the GNRs in the line defect can be estimated using the relation,

$$u_{\mathrm{vdW}}(r_{\mathrm{cc}}) = \frac{A_H}{6}\left(\frac{2I_{\mathrm{nr}}^2}{r_{\mathrm{cc}}^2 - 4I_{\mathrm{nr}}^2} + \frac{2I_{\mathrm{nr}}^2}{r_{\mathrm{cc}}^2} + \ln\frac{r_{\mathrm{cc}}^2 - 4I_{\mathrm{nr}}^2}{r_{\mathrm{cc}}^2}\right), \tag{A.3}$$

Where I_{nr} is the length of the nanorods, $A_H = 10^{-20} - 10^{-19}$ J is the Hamaker constant and r_{cc} is the interparticle distance. The van der Waals potential $u_{\mathrm{vdW}}(r_{\mathrm{cc}})$ between the GNRs at the distances we studied in Fig 4.2(b), ($r_{\mathrm{cc}} = 1$ μm) is many orders of magnitude smaller ($\sim 10^{-6}$ k_B T) than the measured elastic potential (200 k_BT). At smaller distances between the GNRs such as

the one in sandwich structure, the van der Waals potential increases to $\sim 5^{-10}\ k_B$T.

Appendix B

Supporting material to Chapter 5

Fig. B.1 show a TEM image of one of the GNRs used in this work. Different fine-textures (FT) form in the aqueous dextran solution containing the GNRs with a uniform size-distribution. Assemblies of fine-textures 1 (FT1) appear generally with a multilayer configuration, and they are obtained at very high concentrations of GNRs with much longer duration ($\sim$1 hour) and a very slow evaporating rate. Fig. B.2(a), (b) show the Optical Microscopy (OM) and Polarized Optical Microscopy (POM) images of the FT1 structures, while Fig. B.2(c) demonstrates the distribution of the director field using a retardation plate γ inserted at a 45° angle with respect to the polarizer. Fig. B.2(d) shows a schematic diagram of the FT1 structure. Different fine-textures were also observed, FT2, FT3, and FT4. Fig. B.2 illustrates further details of these textures along with the appropriate schematics.

Fig. B.3(a-e) show the merging area of a (π-wall) between two GNRs partially merged assemblies imaged under a POM in a dark-field mode. A parallel arrangement of the rods next to the π-wall is suggested considering that the π-wall is the brightest with the the wall direction is parallel to the analyzer. As two assemblies approach each other, a local 180° twist is prone to form on the edges between the two membrane assemblies, as demonstrated in the SEM images in Fig. B.3(h). However, not all merging assemblies form a π-wall, as shown in Fig. B.3(g).

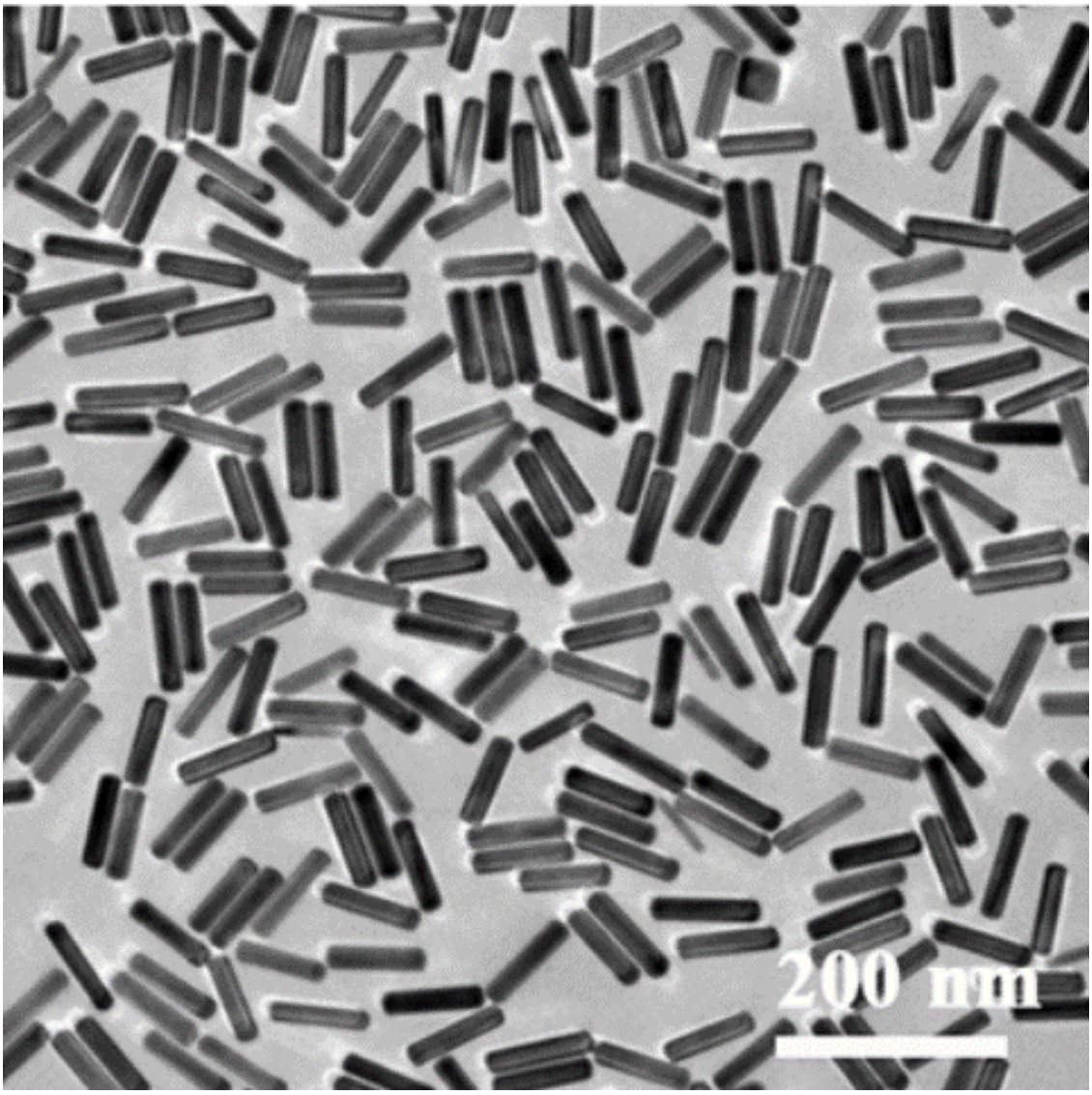

Fig. B.1: TEM image of GNRs.

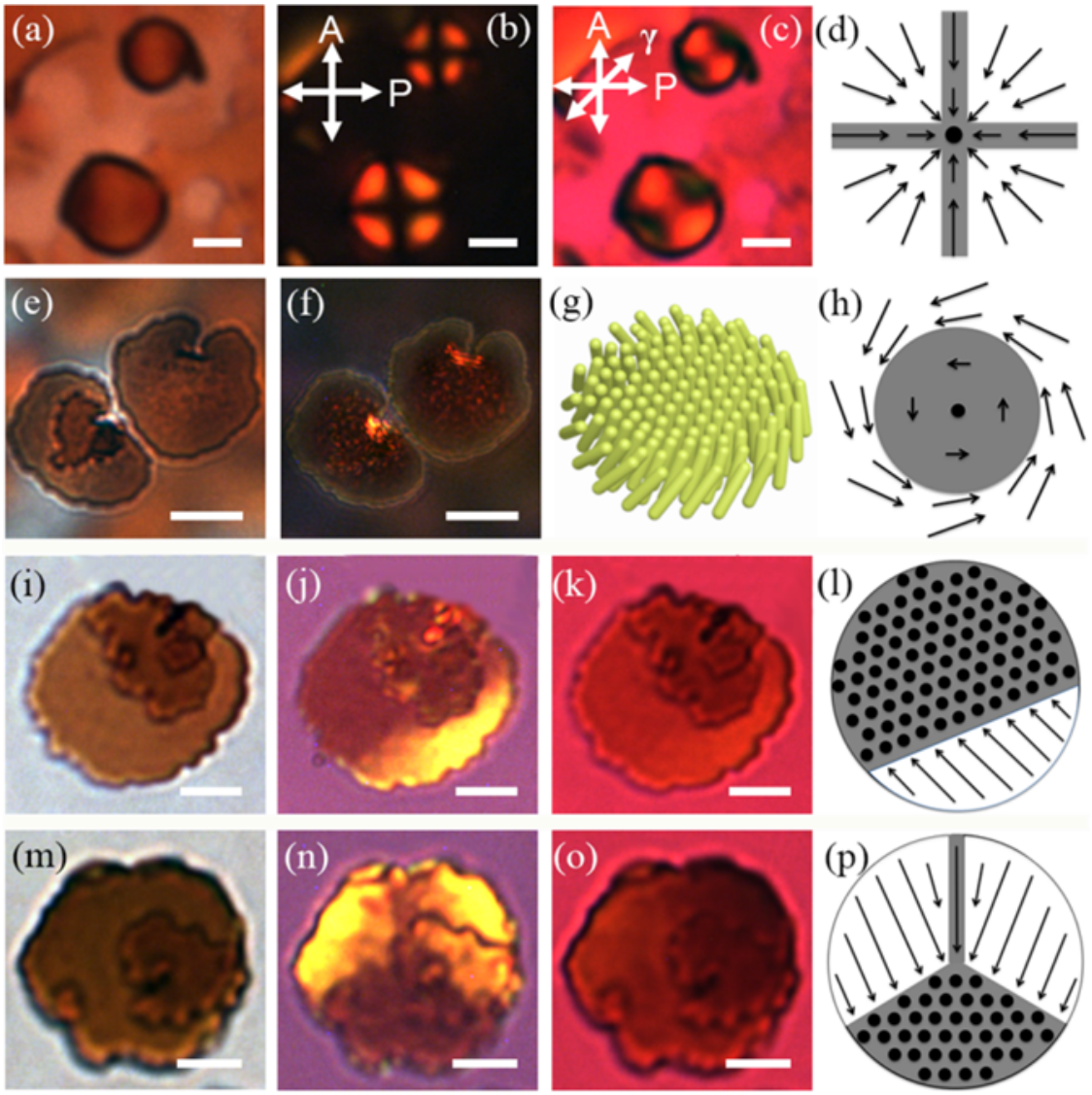

Fig. B.2: (a, e, i, m) Show OM images of different gold nanorods lamellar self-assemblies formed under subtle different formation conditions: FT1, FT2, FT3, and FT4 respectively. (b, f, j, n) POM images showing the different birefringence patterns corresponding to different interior fine-textures. (c, k, o) Demonstrate the corresponding POM images with phase plate γ inserted showing the director field distribution for FT1, FT3, and FT4, respectively. Scale bar is 10 μm. (g) 3D illustration of the twist of FT2 close to the edge. (d, h, l, p) Schematic diagrams showing the physical pictures of the corresponding interior fine-textures of GNRs self-assembly, which clarify the appearance of birefringence in (b, f, j, n), respectively.

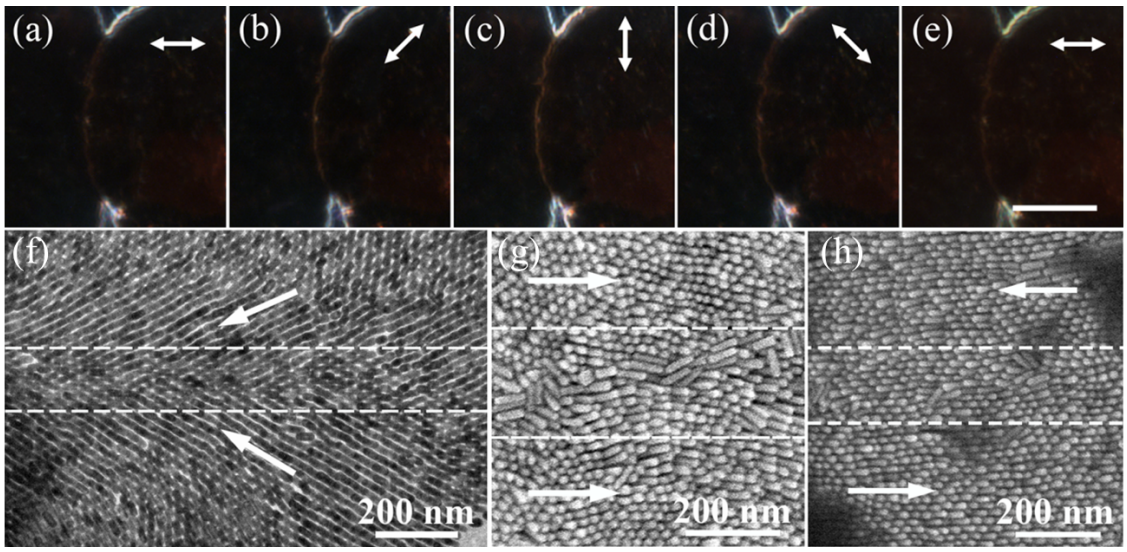

Fig. B.3: (a-e) A twist domain wall (π-wall) formed in two partially merged GNRs self-assemblies taken under polarized dark-field imaging mode. All scale bars are 1 μm. (f-h) Different wall configurations between the dashed lines in each image. (f) A specific angled alignment of rods in a TEM image. (h) An SEM image of GNRs orientation between the two merging self-assemblies, where they form a perfect self-assembled unit without any twisted deformation or defects in between, while a full 180° twist between the two assemblies, also known as a π-wall illustrated in (g).